Faculté des Sciences **Département d'Astrophysique, Géophysique et Océanographie**

Performance study of space-based infrared nulling interferometers

MÉMOIRE DE DEA

Année Académique 2006-2007

présenté pour l'obtention du

Diplôme d'Études Appronfondies en Sciences

par

Denis Defrère

Composition du jury

Président :	Pr. Jean-Pierre SWINGS
Superviseur :	Pr. Jean SURDEJ
Examinateur :	Pr. Claude JAMAR

Institut d'Astrophysique et de Géophysique de Liège

Mis en page avec la classe thloria.

Acknowledgements

The completion of this work would not have been possible without the help, guidance and advice of a number of people. First of all, I would like to acknowledge the support of my advisor, Professor Jean Surdej. Thank you Jean for introducing me to stellar interferometry and for your wise advice during this study.

My utmost gratitude goes also to Dr Olivier Absil for his expert advice and constant guidance since the beginning of this master thesis. This work greatly benefits from Olivier's work and insights into nulling interferometry. I am also very grateful to him for having fostered so many fruitful international collaborations and for his diligence with the corrections of my manuscripts.

I also want to express my deepest gratitude to Professor Jean-Pierre Swings who has given me the opportunity to achieve important experiences in my starting scientific career.

My warmest thank goes also to the Darwin Team at ESA/ESTEC. A special thank to Malcolm Fridlund, Roland den Hartog and Anders Karlsson, for inviting me at the TE-SAT meetings and their expert advice. I take also the opportunity to thank Darwin/Pegase collaborators: Vincent Coudé du Foresto, Alain Léger, Marc Ollivier, Marc Barillot, Jean-Michel Le Duigou, Yvan Stockman and Oliver Lay.

I am also grateful to Professors Jean-Pierre Swings and Claude Jamar for accepting to read and evaluate this work.

Finally, I would like to acknowledge the support of all my colleagues and friends at the Institut d'Astrophysique et de Géophysique de Liège. Special thanks go to Arnaud Magette, Pierre Riaud, Charles Hanot and Dimitri Mawet who have nicely carried this work forward.

This research was supported by a fellowship from the Belgian National Science Foundation ("Boursier FRIA").

Contents

Notations and acronyms

Atmospheric windows

Y band	from 0.95 to 1.1 μm
J band	from 1.15 to 1.4 μm
H band	from 1.5 to 1.8 μm
K band	from 2.0 to 2.4 μm
L band	from 2.8 to 4.2 μm
N band	from 8 to 13 μm

Units

arcmin (or $'$)	minute of arc (2.90888×10^{-4} radian)
arcsec (or $''$)	second of arc (4.848137×10^{-4} radian)
mas	milli-arcsec (10^{-3} arcsec)
μas	micro-arcsec (10^{-6} arcsec)
AU	Astronomical Unit (1.495978×10^{11} m)
pc	parsec (3.085678×10^{17} m)
Myr	Mega-years (one million years)
Gyr	Giga-years (one billion years)
i	The imaginary unit
Jy	Jansky (10^{-26} W m^{-2} Hz^{-1})
zodi	Density unit for dust discs, equivalent to the solar zodiacal disc

Notations

$M_\odot$	Mass of the Sun (1.98892×10^{30} kg)
$R_\odot$	Radius of the Sun (6.96×10^{8} m)
$L_\odot$	Luminosity of the Sun (3.846×10^{26} W)
$M_{\rm Jup}$	Mass of Jupiter (1.8987×10^{27} kg)
$R_{\rm Jup}$	Radius of Jupiter (7.1492×10^{7} m)
$M_\oplus$	Mass of the Earth (5.97370×10^{24} kg)
$R_\oplus$	Radius of the Earth (6.37814×10^{6} m)
$M_\star$, $T_\star$, $L_\star$	Mass, effective temperature and luminosity of a star
$B_\star$	Photospheric brightness of a star
$R_\star$, $\theta_\star$	Linear and angular radius of a star
rms	Root Mean Square (the quadratic mean)
$\eta_\oplus$	Percentage of solar-type stars that have Earth-like planets

Acronyms

AGN	Active Galactic Nuclei
ALADDIN	Antarctic L-band Astrophysics Discovery Demonstrator for Interferometric Nulling
AO	Adaptive Optics
APS	Achromatic Phase Shifter
AT	Auxiliary Telescope
BH	Black Hole
BLINC	BracewelL Infrared Nulling Cryostat
CHARA	Center for High Angular Resolution Astronomy (Georgia State University)
CNES	Centre National d'Etudes Spatiales
CoRoT	Convection Rotation and planetary Transits
Darwin	Not an acronym - infrared space interferometer (ESA)
EGP	Extrasolar Giant Planet
ESA	European Space Agency
ESO	European Southern Observatory
FLUOR	Fiber Linked Unit for Recombination
FSU	Fringe Sensing Unit
GAIA	Global Astrometric Interferometer for Astrophysics
GENIE	Ground-based European Nulling Interferometer Experiment
HZ	Habitable Zone
IAS	Institut d'Astrophysique Spatiale
IRAS	Infra-Red Astronomical Satellite
ISO	Infrared Space Observatory
JPL	Jet Propulsion Laboratory
JWST	James Webb Space Telescope
KI	Keck Interferometer
KIN	Keck Interferometer Nuller
LBTI	Large Binocular Telescope Interferometer
MMT	Multi-Mirror Telescope
MMZ	Modified Mach Zehnder
NASA	National Aeronautics and Space Administration
OB	Observation Block
ODL	Optical Delay Line
OPD	Optical Path Difference
Pegase	Not an acronym - infrared space interferometer (CNES)
PRIMA	Phase-Referenced Imaging and Micro-arcsecond Astrometry
PSD	Power Spectral Density
PSF	Point Spread Function
PTI	Palomar Testbed Interferometer
RV	Radial Velocity
SIM	Space Interferometry Mission
SNR	Signal-to-Noise Ratio
TPF-C	Terrestrial Planet Finder Coronograph
TPF-I	Terrestrial Planet Finder Interferometer
TTN	Three-Telescope Nuller
UT	Unit Telescope
VBA	Visual Basic for Applications
VLTI	Very Large Telescope Interferometer
YSO	Young Stellar Objects

Introduction

One of mankind's most fundamental questions is whether life exists outside our solar system or not. Already in antiquity, the presence of planets like Earth, orbiting other stars and hosting a biological activity, was speculated (Epicurus, 300 B.C.). This question, remained philosophic for at least 2300 years, is today at the dawn to be answered in scientific terms. The key year was 1995 with the discovery of the first extrasolar planet orbiting around a solar-type star (namely *51 Pegasi b*). About 250 extrasolar planets are known today and the recent detection of planets with masses approximately 5 times that of Earth suggests that low mass extrasolar planets exist. Another milestone in the quest for life elsewhere in the Universe has been reached in 2007 with the conclusive detection of water vapor (presumably necessary for the emergence of life) in the atmosphere of hot giant extrasolar planets. While it is unlikely that life exists on such planets, this result supports the idea that significant quantities of water could exist in extrasolar systems.

Detecting planets around distant stars is a challenging task due the high contrast and the small angular separation between the stars and their environment. To date, most known extrasolar planets have been detected indirectly by measuring effects they induce on their parent star. Except in very specific favorable cases, indirect detections generally do not enable the characterisation of planetary atmospheres, indispensable to search for traces of biological activity. In that context, nulling interferometry has been identified as a solution to directly detect photons from extrasolar planets. In addition to providing the required spatial resolution, this technique allows to strongly reduce the stellar emission by combining the light from two telescopes in phase opposition (so that a dark fringe appears on the line of sight).

Whereas nulling interferometry is already used in several ground-based instruments, ambitious projects of space-based nulling interferometers promise outstanding science in a relatively near future. In particular, discovering other worlds like Earth and probing their atmosphere for evidence of life seem more than ever within reach with the ESA's Darwin and NASA's Terrestrial Planet Finder (TPF) missions. Observing in the infrared (6-20 μm), these space-based nulling interferometers could enable the spectroscopic characterisation of the atmosphere of habitable extrasolar planets orbiting nearby main sequence stars. Considerable efforts have been carried out during the past decade to define a mission design that provides excellent scientific performance while minimizing cost and technical risks. These efforts on both sides of the Atlantic have finally resulted in a convergence and consensus on the mission architecture, which has been used as a baseline for the proposal recently submitted to the ESA Cosmic Vision programme.

Flying Darwin/TPF will however be an extraordinary technological challenge and a first step could be taken by a smaller mission. In that respect, several proposals have been made, using the simplest nulling scheme composed of two collectors (i.e. the original Bracewell interferometer). One of these projects, Pegase, has also been proposed in the framework of the Cosmic Vision programme. In addition to paving the technological way of Darwin/TPF, Pegase presents very good prospects for the characterisation of hot extrasolar giant planets (i.e. Jupiter-size planets orbiting close to their parent star). Pegase would also be a valuable scientific precursor for Darwin/TPF, particularly by assessing the level of circumstellar dust around nearby main sequence stars (the ability to study terrestrial extrasolar planets can be hampered by too bright exozodiacal clouds).

This master thesis is devoted to the performance study of space-based infrared nulling interferometers,

particularly for Pegase and Darwin. After reviewing the state of extrasolar planet science in Chapter 1, the principle of nulling interferometry is presented in Chapter 2, together with the existing facilities. In Chapter 3, the performance of Pegase for the exozodiacal disc and planet detection is addressed. Investigations of an upgraded version of Pegase (namely Pegasus) are also reported. Finally, in Chapter 4, the simulated performance of Darwin is given, in terms of the number of planets for which a robust detection of biological activity could be performed. The results reported for Pegase and Darwin, detailed respectively in Chapters 3 and 4, have both contributed to their respective proposal to the ESA's Cosmic Vision programme.

1

Extrasolar planet science

Contents

Abstract. The study of extrasolar planets and the search for other habitable worlds are just beginning. To date, nearly 250 extrasolar planets have been unveiled, mostly by indirect detection techniques, and about 62 ground-based and 16 space-based search programmes are ongoing. Prospects from the ground (radial velocity and transits) or from space (transits and astrometry) promise to identify Earth-size planets orbiting their host star within 1 astronomical unit. Information on protoplanetary and debris discs will complete the understanding of the planetary formation and evolution. After this initial reconnaissance, the next generation of space observatories will directly detect photons from planets in the habitable zone of nearby stars, opening the era of comparative evolutionary biology with the possible discovery of life itself. After a brief overview of the current observational results, for extrasolar planets and for circumstellar discs, this chapter presents the main instruments which promise exceptional advancements in the field of planetary science.

1.1 Extrasolar planets

Extrasolar planets became reality in the 1990s with the first discoveries by Wolszczan and Frail (1992) and Mayor and Queloz (1995). These pioneer astronomers initiated a dramatic explosion in the field of extrasolar planet research, gathering today a worldwide community. Several instruments are now operational or foreseen for the near future and the first dedicated space-based telescope has found its

first planets. So far, about 250 extrasolar planets have been reported[1], suggesting that planetary systems are very common in our galaxy.

1.1.1 Planet population in our galaxy

The first extrasolar planet detected around another solar-type star (namely *51 Peg*) unveiled an unexpected new type of planets: hot Extrasolar Giant Planets (EGPs). Unlike any planet in our solar system, "*51 Peg b*" is a Jupiter-like mass planet (minimum mass of 0.468 M_{Jup}) with a very short orbital period (4.23 days). This corresponds to a semi-major axis of 0.052 astronomical unit (AU) which is much closer than Mercury from the Sun (0.39 AU). Due to this proximity to its parent star, "*51 Peg b*" is heated up to about 1000 K and is often referred to as "hot Jupiter´´. To date, 59 planets have been found with semi-major axes smaller than 0.1 AU (see Figure 1.1, left), i.e. with orbital periods shorter than about 10 days. In total, 248 planets have been discovered so far, with masses ranging from the deuterium-burning limit of 13 M_{Jup} (Chabrier *et al.* 2000) down to 5 Earth masses (1 Earth mass $\simeq$ 0.0031 M_{Jup}). These planets are found in orbits ranging from inside 0.05 AU out to 270 AU with a wide range of orbital eccentricities.

Most of the planets discovered so far, i.e. 236 out of 248 planets, were indirectly detected by the so-called radial velocity (RV) technique in which the stellar wobble of the star moving around the center of mass of the star-planet system is measured with spectral Doppler information. This provides a measurement of $M \sin i$, where M is the planetary mass and i the planetary system's inclination with respect to the plane of the sky. The latter being generally unknown, only a lower limit can be inferred for the planetary mass. To date, the lowest mass planet detected by RV is the newly discovered *Gliese 581c* (Udry *et al.* 2007), which has a minimum mass of 5.1 $M_{\oplus}$. This planet orbits around a star 3 times less massive than the Sun and causes a radial velocity deflection of about 2.5 meters per second (m/s). To detect Earth-like planets, the accuracy on velocity measurements has to be at least a factor 10 better, since Earth causes a reflex motion of order 0.1 m/s in the solar spectrum. Another successful technique for EGP detection relies on the dimming of the apparent stellar flux as the planet transits in front of the stellar photosphere. Even though the probability to detect such a transit is rather low, 23 hot EGPs have either been found or confirmed using this technique. So far, about 5% of the stars monitored in RV surveys have been found to harbor at least one planet. The median planet mass is about 1.5 M_{Jup} (or about 450 $M_{\oplus}$). This relatively large value is almost certainly a result of instrumental detection bias since the RV technique is biased towards high mass/short orbital period planets. Indeed, there are several reasons to expect that many more small planets exist, and will be detected with more sensitive instruments (see section 1.1.2). Despite this inevitable bias, remarkable statistical properties have emerged from the 248 known planets :

- The evidence of planets around solar-type stars has been estimated by Lineweaver and Grether (2003). At least ∼9% of Sun-like stars have planets in the mass and orbital period ranges $M \sin\ i > 0.3\ M_{Jup}$ and $P < 13$ years, and at least ∼22% have planets in the larger range $M \sin\ i > 0.1\ M_{Jup}$ and P<60 years. Even this larger area of the log(mass)-log(period) plane covers less than 20% of the area occupied by our planetary system, suggesting that this estimate constitutes still a lower limit of the true fraction for Sun-like stars with planets.

- About 25 multiple systems have also been detected so far presenting a tendency for the inner planets to be less massive, which can be interpreted either as suppressed accretion from the outer disc or as a mere selection effect (Marcy *et al.* 2005). The detection of multiple systems provides hope that analogs to the solar system exist.

- The median semi-major axis is about 0.8 AU, partly reflecting an instrumental bias towards smaller values, but also showing that these giant planets mostly exist much closer to their parent star than

[1] see Schneider (2007) for an up-to-date list

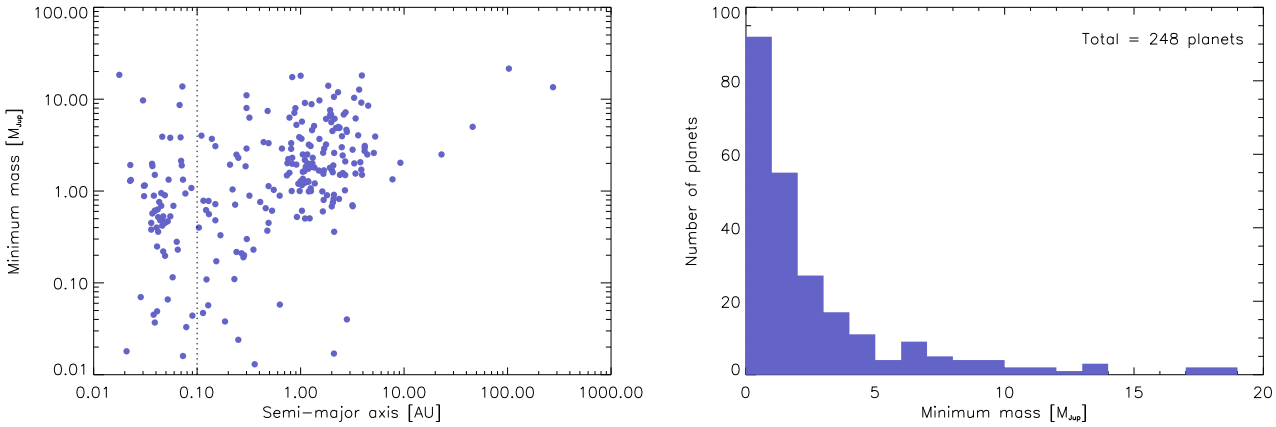

Figure 1.1: Left, extrasolar planet population synthesis, distributed as minimum mass versus semi-major axis. Hot regime planets are concentrated at the left of the dotted line. Right, number of detected extrasolar planets versus minimum mass. The lack of companions with $M \sin i$ larger than 13 $M_{\rm Jup}$ confirms the presence of a "brown-dwarf desert" (data taken from Schneider 2007).

would be expected from our solar system experience. The inference is that they have migrated from greater distances, which in turn raises many questions about what started and stopped the migration, what happened to planets that were in the migration path, and whether the stars without such migrated planets in fact have terrestrial planets instead.

Further statistical investigations have also revealed correlations between stellar metallicity and planet occurrence rate, suggesting that planets form more easily in a metal-rich environment. Another unexpected behaviors are the prevalence of high eccentric orbits. This is in sharp contrast with the planets of our solar system. Figure 1.1 (right) shows the dearth of companions with $M \sin i$ larger than 13 $M_{\rm Jup}$, confirming the presence of a "brown dwarf desert", at least for companions with orbital periods up to about 10 days.

These observational results provide strong reasons to believe that extrasolar planets are formed by a different mechanism than low-mass companion stars and are thereby putting strong constraints on the planetary formation theories, particularly favoring the core accretion model.

1.1.2 Principles of planet formation

The presence of planets orbiting around other stars is a natural consequence of the process of stellar formation (see e.g., Bodenheimer 1997; Mannings *et al.* 2000; Boss 2003). Stars are formed out of interstellar clouds of gas and dust where turbulent processes lead sufficiently dense regions to collapse, leading to an embedded pre-stellar core and a circumstellar disc, which retains most of the angular momentum of the cloud. The planets are believed to form from the material in the circumstellar disc, which is in this stage also referred to as the "protoplanetary" disc.

At this point, two representative models have been proposed to explain the planetary formation process; the core-accretion scenario (Pollack 1984) and the disc instability scenario (Cameron 1978). According to the core-accretion scenario, a heavy element core is first assembled by the accretion of planetesimals in the outer part of protoplanetary discs, beyond the snow line[2] (Sasselov and Lecar 2000). As these cores grow, they eventually become sufficiently massive to gravitationally bind nebular gas. While this gas accretion proceeds slowly in the early phases, it eventually runs away when a

[2]The snow line refers to the distance from the star at which the mid-plane temperature of the protoplanetary disc drops to the sublimation temperature of ice.

critical mass is reached (the so-called cross-over mass, typically at around 10 Earth masses), allowing the formation of a gas giant within 10 Myr (Pollack *et al.* 1996). Because this timescale is uncomfortably close to the typical lifetime of protoplanetary discs, believed to be of the order of 1-10 Myr (Haisch *et al.* 2001), a long-discarded mechanism, based on local gravitational collapse of the protoplanetary disc, has been reevaluated by Boss (1998) to allow for a more rapid formation of giant planets. In this disc instability scenario, the discs fragment into a dense core if it is sufficiently massive. Such clumps can contract to form giant gaseous planets in several hundred years. Gas giants are quickly formed before the gas in the disc depletes. Unfortunately, this model is unable to account for the period-eccentricity relations of the observed systems.

In any case, formation scenarios require giant planets to be formed in the outer part of protoplanetary discs. These theories are obviously incompatible with the observation of giant planets orbiting close to their parent star, where a sufficient amount of gas is not available to form such large bodies and the temperature far too high to allow the condensation of solid particles. This apparent contradiction is now understood in the framework of migration processes: in the protoplanetary disc, the planets are assumed to excite density waves that propagate on both sides of their orbit (Goldreich and Tremaine 1979; Lin *et al.* 1996). Migration involves the tidal interaction between the protoplanet and the gas in the surrounding protoplanetary disc by means of angular momentum exchange. Three types of migration mechanisms can be distinguished:

- *type I migration*, for which planetary embryos embedded in a protoplanetary disc suffer a decay in semi-major axis due to the asymmetric torques produced by the interior and exterior wakes raised by the body. The increased amount of mass outside the planetary orbit causes the planet to lose angular momentum as the material outside its orbit is moving more slowly. The planet then migrates inwards on timescales short relative to the million-year lifetime of the disc;
- *type II migration*, for which the planet is sufficiently massive (more than about 10 Earth masses) to open a gap in the protoplanetary disc. As material enters the gap over the timescale of the larger accretion disc, the planet and the gap move inward over the accretion timescale of the disc. This is presumably how hot EGPs form;
- *type III migration*, which is a new form of potentially fast migration applicable to massive discs that could be driven by orbital torques (Ward 2004).

Comparison with observations shows that 90% of the detected planets are consistent with the core-accretion model regardless of the spectral type (Matsuo *et al.* 2007). The remaining 10% are not in the region explained by the core-accretion model, but are instead explained by the disc instability model. Extended core-accretion models, including in particular migration, disc evolution and gap formation, lead to a much more rapid formation of giant planets, making it compatible with the typical disc lifetimes inferred from observations of young circumstellar discs (Alibert *et al.* 2005). This speed up is due to the fact that migration prevents the severe depletion of the feeding zone as observed in classical core accretion simulations. Hence, the growing planet is never isolated and it can reach the cross-over mass over a much shorter timescale. Based on this extended model, synthetic planet populations can be computed, allowing a statistical comparison with observations (see Figure 1.2). While these models are not specific to terrestrial planets (they are initialized with a mass of 0.6 $M_{\oplus}$), they demonstrate that if planetary embryos can form, only a small fraction of them will grow sufficiently fast and big to eventually become giant planets. Given that EGPs orbit around about 7% of the stars surveyed, there must be plenty of terrestrial planets out there.

Earth-like planets form in the wake of giants. Terrestrial embryos, being closer to the star, have less material available and hence they empty their feeding zone before growing massive. They must then rely on distant gravitational perturbations to induce further collisions. As a result, the growth of terrestrial planets occurs over longer timescales than for the giants. Simulations have revealed that Earth-like planets can be formed with some help from a wandering giant. In particular, a recent study

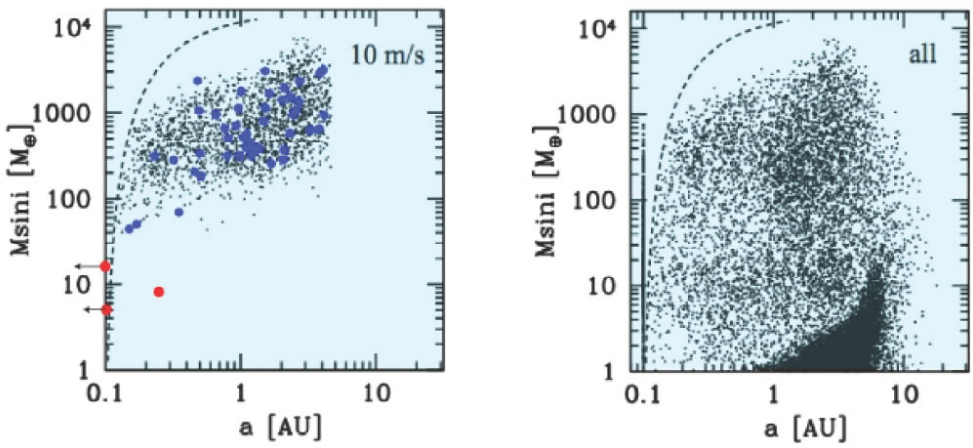

Figure 1.2: Left, extrasolar planet population predicted by the extended core accretion scenario and that are potentially detectable by radial velocity (with a 10 m/s accuracy). The blue dots represent planets actually detected orbiting solar type stars, while the red dots are 3 planets recently detected orbiting the M dwarf *Gl 581*. Right, underlying population of planets. Note that most embryos do not grow to become gas giants, leaving many potentially detectable lower-mass planets.

has shown that planet formation can occur after a giant planet has migrated through the "habitable zone" (Raymond *et al.* 2006), suggesting that migration does not suppress the formation of Earth-like planets by either capturing protoplanetary material or causing the material to be ejected from the habitable zone. Migration could even support the creation of Earth-like planets by concentrating water and heavier materials into the habitable zone. Since about 40% of known planetary systems may have undergone a migration, more than one third of all known planetary systems would include Earth-like planets.

Terrestrial planets have not yet been detected but low-mass companions are discovered at an accelerating pace, with the detection of so-called "hot Neptunes" or "super-Earths". These planets have masses 5-20 times larger than the Earth and are mainly found on close-in orbits with periods of 2-15 days. To date, the lowest mass planet could be *GI 581 c* which presents a $M \sin i$ of about 5.2 $M_{\oplus}$ and is very close to the HZ (see section 1.1.4 for more details) of its parent M star (Udry *et al.* 2007). It is also to be noted that a remarkable system of three Neptune-mass planets with orbital periods of 8.67, 31.6 and 197 days, has been detected orbiting the nearby star HD 69830 (Lovis *et al.* 2006). Theoretical computations favor a mainly rocky composition for both inner planets, while the outer planet probably has a significant gaseous envelope surrounding its rocky/ice core; the outer planet orbits within the HZ of its star.

These detected intermediate-mass planets raise the question of their possible internal composition. In this respect, the diversity of the discovered systems so far was fully unexpected and new kinds of planets have been imagined such as "ocean planets" (Léger *et al.* 2004) and "carbon planets" (Kuchner and Seager 2005). It is interesting to note that ocean planets would be rather easily detectable by transit space missions (CoRot, Kepler, Selsis *et al.* 2007).

1.1.3 First physical characterisations

Characterizing the composition of extrasolar planets requires the possibility to distinguish of the planetary and the stellar spectra. Whereas the radial velocity technique is not appropriate for such a task, transiting extrasolar planets could, when the contrast is not too large, represent a valuable tool to determine key physical and atmospheric parameters of the EGPs (Seager and Sasselov 2000). The basic principle of the method is that the planet atmosphere absorption features are superimposed to the stellar

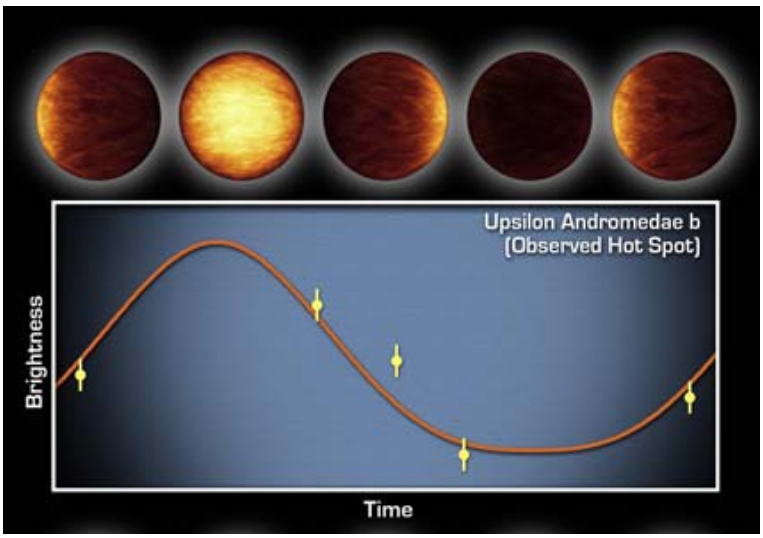

Figure 1.3: The Spitzer telescope has detected the thermal emission of the EGP companion Upsilon Andromedae, throughout the entire 4-day period. The solid curve shows a model of a tidally locked planet with a sub-solar point that is considerably hotter than the backside due to the relatively poor global circulation of winds.

flux as it passes through the planet atmosphere. With this method, some atmospheric properties can be determined (see e.g., Vidal-Madjar *et al.* 2003; Burrows *et al.* 2004; Charbonneau *et al.* 2006). The detection of the secondary eclipse[3] can even provide some limited information on the thermal emission of these planets (Charbonneau *et al.* 2005; Deming *et al.* 2005). By subtracting spectra obtained during secondary eclipse from spectra obtained outside eclipse (star and planet), the emission spectrum of the planet can be deduced. This technique has allowed the physical characterisation of a few transiting planets with the detection at infrared wavelengths by the Spitzer Space Telescope of secondary transits of 4 hot Jupiters (namely *HD 189733 b*, *TrES-1*, *HD 209458 b* and *GJ 436 b*, see Burrows *et al.* 2006 and Deming *et al.* 2007). Phase variations have also been observed by Spitzer at 24 μm, revealing a temperature difference between day and night faces of the EGP companion of υ Andromedae (see Figure 1.3, Harrington *et al.* 2006). These results constrain the temperature, radius, and albedo of the planets and enable the study of the weather on distant planets.

Note that conclusive detection of water vapor on the transiting EGP *HD 189733 b* has been reported for the first time very recently (Tinetti *et al.* 2007). This major scientific result has been followed by the identification of water absorption features in the atmosphere of *HD 209458 b*, suggesting a cloud-free model (Barman 2007). While it is unlikely that life exists on *HD 189733 b* and *HD 209458 b* or any similar extrasolar planet, the research supports the idea that significant quantities of water could exist in extrasolar systems.

1.1.4 Habitable zone and the search for life

The HZ is defined as the region around a star within which an Earth-like planet can sustain liquid water on its surface, a condition necessary for photosynthesis. Within the HZ, starlight is sufficiently intense for a greenhouse atmosphere to maintain a surface temperature above 273 K, and low enough not to initiate runaway greenhouse conditions that can vaporize the whole water reservoir, allowing photo-dissociation of water vapor and the loss of hydrogen to space (Kasting *et al.* 1993). If the region remains habitable for a duration longer than 1 Gyr, the HZ is then referred to as "Continuous". For the Sun, the continuous habitable zone extends roughly from 0.76 to 1.6 AU. The limits of the continuous HZ as a function of the stellar mass is represented in Figure 1.4.

[3]The secondary eclipse is the phase during which the planet is occulted by its host star.

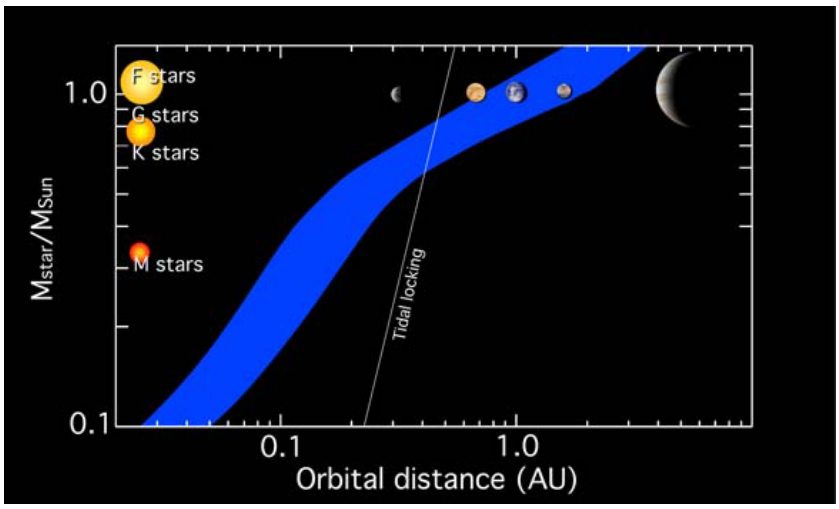

Figure 1.4: Continuous Habitable Zone (blue region) around M, K, G, and F stars. The region around the Sun that remains habitable during at least 5 Gyr extends from approximately 0.76 to 1.63 AU.

Planets located inside the HZ are not necessary habitable. For instance, too small planets, like Mars, cannot maintain active geology since most of their atmosphere escape in space. They can not either be too massive, like *HD 69830 d*, which accreted a thick H_2-He envelope below which water cannot be liquid (Lovis *et al.* 2006). Anyhow, planet formation models predict abundant Earth-like planets with the right range of masses (0.5-8 $M_\oplus$) and water abundances (0.01-10% by mass, Raymond *et al.* 2006).

In order to determine if a planet in the HZ is actually "inhabited", its planetary atmospheres has to be probed to search for the spectral features that are specific to biological activity, the biosignatures. According to Lovelock (1975), the simultaneous presence of large amounts of reducing and oxidizing gases in an atmosphere out of thermodynamic equilibrium can be a criterion for the presence of biological activity. All planetary atmospheres are out of thermodynamic equilibrium because their photochemistry is driven by UV photons from their parent star. For instance, Owen (1980) argued that a large-scale biological activity on a telluric planet necessarily produces a large quantity of oxygen (O_2). By analogy with Earth, the following elements are considered as potential biosignatures :

- **Water vapor** (H_2O). A baseline sign, indicating the presence of liquid water, a requirement of known life;
- **Carbon dioxide** (CO_2). Although it can be created by biological and non-biological processes, it is necessary for photosynthesis and it would indicate the possible presence of green plants;
- **Methane** (CH_4). It is considered as suggestive of life, it can also be made both by biological and non-biological processes;
- **Oxygen (O_2) and its tracers Ozone** (O_3). The best indicator of biological modification of a planetary atmosphere.

Unless molecular oxygen in Earth atmosphere is constantly replenished by photosynthesis, it is quickly consumed in chemical reactions, in the atmosphere, on land and in seawater. So the presence of a large amount of oxygen in an extrasolar planet's atmosphere would be a sign that it might host an ecosystem like present-day Earth's. Concerning the methane, detecting it on a distant world would not automatically indicate the presence of life, although it is often biogenic. For instance, Jupiter and Saturn have traces of it. However, a sufficiently high methane level (around 1000 ppm) may have been produced as a waste byproduct by primitive microorganisms. Even if methane is largely considered as a suggestive but not convincing biosignature, finding oxygen along with methane might constitute the most convincing biosignature.

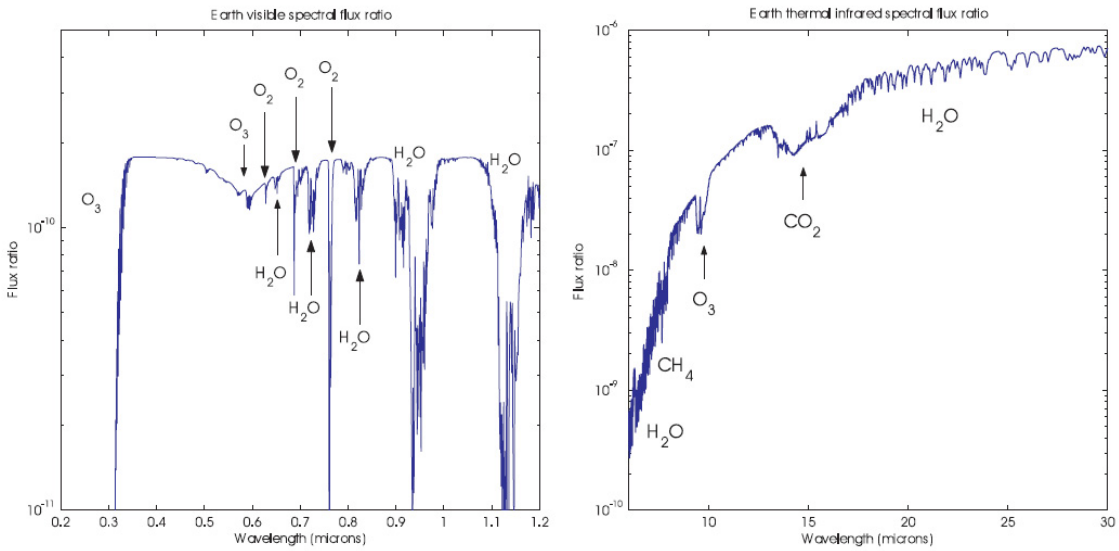

Figure 1.5: Left, Earth spectral contrast in the visible. Spectral feature of biosignatures like O_2, O_3 and H_2O clearly appears. Note that the CO_2 feature is absent in the visible. Right, Earth spectral contrast in the thermal infrared where the CO_2 feature appears (figure from Mawet 2006).

In addition, the reliability of O_2 and O_3 as signature of biological activity has been thoroughly addressed by Léger *et al.* (1999) and Selsis *et al.* (2002). Considering various abiotic production processes, such as photo-dissociation of CO_2 and H_2O, and the possible escape of hydrogen from the atmosphere, they conclude that a simultaneous detection of a significant amount of H_2O and O_3 in the atmosphere of a planet in the habitable zone presently stands as a criterion for large-scale photosynthetic activity on the planet. Such an activity on a planet illuminated by a Sun-like star, is likely to be a significant indication that there is local biological activity. Detecting O_3 in addition to H_2O seems to be a robust biosignature because no counter example has been identified. This is not true for O_2 for which false positive could be detected (Selsis *et al.* 2002).

To reveal the effects of these biosignatures, low-resolution mid-IR (6-20 μm) observations is particularly suited. As shown in Figure 1.5, the wavelength range displays the 9.6 μm O_3 band, the 15 μm CO_2 band, the 6.3 μm H_2O band and the H_2O rotational band that extends longward of 12 μm. The visible wavelength range presents also the main biosignatures features but the planet-star contrast is much less favorable than in the mid-IR (see Figure 1.5, left). Note also that a low-resolution spectrum spanning the 6-20 μm region has the advantage to allow the measure of the effective temperature of the planet, and thus its radius and albedo. For all these reasons, the mid-IR range is currently considered as an optimal observation window for the future life-finding missions such as Darwin and Terrestrial Planet Finder (TPF).

The atmosphere spectrum also depends on the distance between the planet and its host star. Within the HZ, the partial pressure of CO_2 and H_2O at the surface of an Earth-like planet is a function of the distance from the star. Water vapour is a major constituent of the atmosphere for planets between 0.84 AU (inner edge of the HZ) and 0.95 AU. Figure 1.6 shows the estimated evolution of the H_2O, O_3 and CO_2 features in the spectra of an Earth-like planet as a function of its location in the HZ. Carbon dioxide is a tracer for the inner region of the HZ and becomes an abundant gas further out.

Considering the solar system, the right part of Figure 1.6 shows the spectra for Venus, Earth and Mars. For instance, Venus, closer to the Sun than the HZ, has lost its water reservoir and accumulated a thick CO_2 atmosphere. Planets like Venus can be identified as uninhabitable by the absence of water and by the high-pressure CO_2 absorption bands between 9 and 11 μm. The Earth's spectrum is also clearly distinct from that of Mars which presents no H_2O and O_3 feature. According to Segura *et al.* (2003), the ozone absorption band is observable for O_2 concentrations higher than 0.1% of the present terrestrial

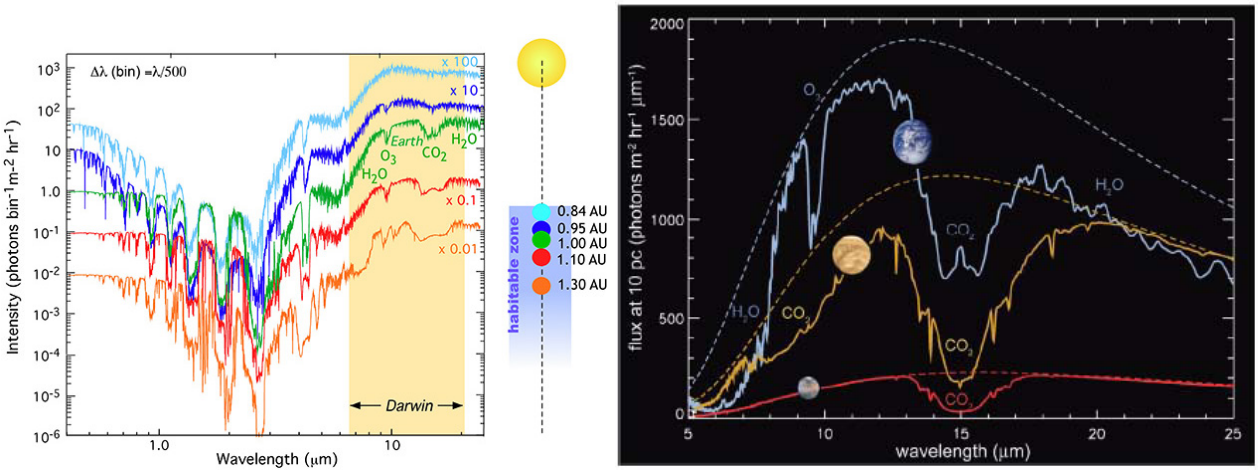

Figure 1.6: Left, synthetic spectra of an Earth-like planet computed at different orbital distance across the solar habitable zone (courtesy J. Paillet). Right, mid-IR spectra of Venus, the Earth and Mars as seen from 10 pc.

atmospheric level. Concerning the Earth spectrum, it has displayed this feature for the past 2.5 Gyr (Kaltenegger *et al.* 2007b). Other spectral features of potential biological interest include methane (CH_4 at 7.4 μm), and species released as a consequence of biological fixation of nitrogen, such as ammonia (NH_3 at 6 and 9-11 μm), nitrous oxide (N_2O at 7.8, 8.5 and 17 μm) and nitrogen dioxide (NO_2 at 6.2 μm). The presence of these compounds would be difficult to explain in the absence of biological processes.

1.2 Circumstellar discs

The presence of dust around a mature main-sequence star is a reminder that the star was born by accretion in a dense protostellar disc of gas and dust and that any planet orbiting around the host star was born out of that same material. The effect of gas may be an important factor, as suggested by Takeuchi and Artymowicz (2001): relatively modest amount of gas could strongly affect the dynamics of small dust grains, leading to the formation of azimuthally symmetric structures like cleared zones or dust rings. This general conclusion is supported by more recent modelling (Klahr and Bodenheimer 2006), which also showed that such gas-formed structures can persist after the gas is completely gone. In theory, dust grains are removed by radiative forces in a few thousands to a few millions of years, such as the dust observed around a mature star is not itself primordial. However, the largest bodies of the observed small dust grains (for instance asteroids or comets) are the remnants of this primordial material, and the debris associated with them provide hints to the origin of planetary systems. In addition, this solid material is important in the evolution of life, since the cold outer region of a planetary system is believed to be rich in water and volatiles needed for the creation of habitable environments in the inner parts of the system.

1.2.1 Debris discs

First discovered by the InfraRed Astronomical Satellite (IRAS), the "Vega phenomenon" characterises main-sequence stars presenting a significant deviation from their expected Rayleigh-Jeans emission (Aumann *et al.* 1984). These photometric excesses are now commonly understood as the signature of dust surrounding the stars, analogous to the zodiacal cloud and/or the Kuiper belt in our own solar system (Backman and Paresce 1993). This dust originates mainly from collisions between small bodies or from outgassing comets (Beust *et al.* 1996), and has a limited lifetime due to physical effects such as radiation

pressure, collisions and drag. Extrasolar systems with IR excess presumably have their own supply of large, solid planetesimals and, perhaps, large planets like those in our system. The gravitational influence of such planets is suspected to be at the origin of the structures (like rings, warps and gaps) observed in the handful of visible and sub-millimetric images of debris discs that have been obtained during the last decade (Augereau and Papaloizou 2004).

Characterisation of warm circumstellar dust (≥ 300 K) in the inner part of debris discs is particularly important to understand the physical and dynamical properties of the discs, including planetary formation and evolution mechanisms in the regions where terrestrial planets are supposed to be located. In fact, the scarce resolved images of debris discs obtained so far in the visible (e.g. Heap *et al.* 2000; Kalas *et al.* 2004, 2006) and sub-mm (e.g. Holland *et al.* 1998, 2003; Greaves *et al.* 2004) regimes have revealed the presence of extended structures associated with a void of matter in the central region (< 50 AU). Warps, gaps and clumpy structures have been repeatedly detected and attributed to the gravitational influence of planets, which may also be the cause for the apparent void of matter in the inner region (e.g. Wyatt and Dent 2002). Several studies have already searched for warm dust in these cavities using mid-IR photometry, but with poor results. For instance, Fajardo-Acosta *et al.* (1998) have only found 5 systems with weak 10 μm excess, suggesting the presence of dust between 1 and 10 AU with median grain temperatures ranging between 200 and 350 K. Such an excess is most of the time not detectable by classical aperture photometry because both the photometric accuracy and the precision on the mid-IR photospheric fluxes are of the order of or larger than the excess to be measured.

One of the main questions is whether inner dust reservoirs can survive the suspected planetary migration, and continue to replenish the inner disc at advanced ages. It is in fact expected that planetesimals trapped in mean motion resonances with the migrating planet could be pushed towards the innermost regions as the planet migrates inwards during the early system evolution, and thereby constitute a significant reservoir of solid bodies.

1.2.2 Summary of current observational results

Spitzer view

The surveys performed by IRAS, ISO and more recently by the Spitzer Space Telescope have shown that about 15% of mature solar-type stars (F0 - K0) harbour cold debris discs (Beichman *et al.* 2006c). These observational results have greatly improved our understanding of the incidence of exozodiacal clouds as a function of age, spectral type and metallicity. For instance, older stars use to present less infrared excess than younger. Specific programs focused on main sequence stars with planetary companions have shown that this proportion increases to $24 \pm 10\%$ for old ($\sim$ 5 Gyr) planet-bearing stars, while the overall frequency of excesses at similar ages is about 10% (Beichman *et al.* 2005b). On the contrary, the established correlation between stellar metallicity and the presence of extrasolar planets is not observed in the case of debris discs (Greaves *et al.* 2006). All these elements raise the question of how planets, planetesimals and dust grains interact and evolve in extrasolar systems.

At 70 μm, Spitzer is sensitive to levels of exozodiacal emission in the range of 35 - 75 K dust with $L_{\rm disc}/L_\star \sim 10^{-6}$ to 10^{-5}, or roughly 5 - 10 times the expected level of emission of our own Kuiper Belt. A wide variety of Spitzer programmes has found the following characteristics of exozodiacal emission:

- Approximately $14 \pm 3\%$ of mature, solar type stars (spectral type in the F5-G5 range) have detectable 70 μm zodiacal emission at a level of $L_{\rm disc}/L_\star = 10^{-5}$ to 10^{-6} (Bryden *et al.* 2006). This rate is somewhat higher among A and early F stars ($\pm$ 25%) and smaller for stars later than K ($< 4\%$) (Beichman *et al.* 2006b).
- Emission at 10 μm, corresponding to dust in the HZ and thus most relevant to DARWIN, is very rare at the Spitzer sensitivity level for mature stars. However, the unfavorable contrast ratio at this wavelength means that Spitzer can detect emission only at a level $\pm$ 1000 times brighter than our

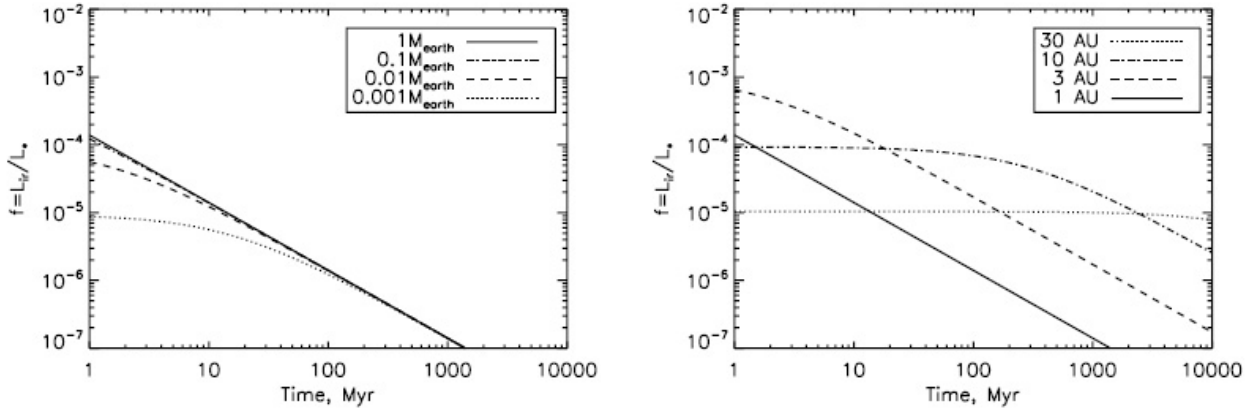

Figure 1.7: Models of the evolution of the total exozodiacal emission as a function of time for different total disc masses (left) and disc locations (right). After a few Gyr, solar-type stars with discs interior to 10 AU reach zodiacal levels comparable to our own, f = $L_{disc}/L_\star = 10^{-7}$ (figure from Wyatt *et al.* 2007).

own zodiacal cloud. Initial estimates based on Infrared Astronomical Satellite (IRAS, Mannings and Barlow 1998; Fajardo-Acosta *et al.* 2000) and Infrared Space Observatory (ISO, Laureijs *et al.* 2002) observations were that $< 2\%$ of systems have detectable discs at 10 μm, while the largest Spitzer sample studied to date of 150 stars suggests a rate of less than 1% (Beichman *et al.* 2006b). While a few individual objects, including A stars like β Pic and β Leo and the 2-4 Gyr old K0 star HD 69830 (Beichman *et al.* 2005a), show bright emission from small grains in the HZ, such stars are very rare.

- Zodiacal emission is both more intense and more frequent (up to 30% at 24 μm) at ages less than $\sim$ 150 Myr (Rieke *et al.* 2005; Siegler *et al.* 2007), but at stellar ages greater than about 1 Gyr, the incidence of exozodiacal emission shows little dependence with age.

These observational results can begin to guide the expectations for the amount of zodiacal emission around the majority of mature main sequence stars. Models based on collisions between planetesimals can be developed to reconstruct the evolution of debris discs and confronted with the properties of the emerging population of Sun-like stars that have hot dust. Considering a solar type star, the curves in Figure 1.7 show the evolution of $f = L_{disc}/L_\star$ as a function of time depending on the mass and location of the parent disc (Wyatt *et al.* 2007).

The predicted level of zodiacal emission drops well below 10 times that of our system by the time the star reaches a few Gyr. The right-hand curves show the variation of the expected emission for different disc sizes (1, 3, 10, 30 AU). The 3-AU case corresponds to the location of our asteroid belt and reproduces almost exactly the level of emission in our own Solar System, $L_{disc}/L_\star$, a few 10^{-7}. The 10-AU and 30-AU cases predict a higher level of zodiacal emission than is presently seen in the solar system. Nevertheless, this model ignores the clearing action of the Jupiter and Saturn which would either have incorporated much of the planetesimal material into a solid core, or ejected the material. While the theoretical understanding is far from complete, these results validated by present and future observations of discs, should give confidence that the expected level of emission will be at or below the desired $\sim$ 10 - 20 exozodiacal level needed for the detection of terrestrial planets around many nearby stars (see Chapter 4).

Interferometric view

In general, due to the limited spatial resolution of Spitzer, the localisation of the grains cannot be accurately inferred in the region where physical and dynamical processes need to be studied. Resolving

the star-disc system is therefore the most reliable way to assess the presence of small quantities of warm dust around solar-type stars and only infrared interferometry can investigate the inner disc in a thorough manner.

The first attempt to detect a debris disc was performed at the Palomar Testbed Interferometer (PTI) by Ciardi *et al.* (2001) on the prototypical debris disc star Vega. A simple debris disc model, accounting for 3 to 6% of Vega's near-infrared flux and emanating from a region within 4 AU, was proposed. However, the determination of the circumstellar disc emission was rather imprecise due to the limited and inappropriate spatial frequency range. A second, more thorough study, was then performed by Di Folco *et al.* (2004) with the VINCI instrument at Very Large Telescope Interferometer (VLTI) on five Vega-like stars. Due to the limited precision of the VLTI observations at that time, and to the unavailability of short baselines, this study did not allow an unambiguous detection of warm dust around these stars. Finally, a study on debris discs has been performed by nulling interferometry using the BracewelL Infrared Nulling Cryostat (BLINC) instrument at the Multi-Mirror Telescope (MMT, see the description in section 2.4.1, Liu *et al.* 2004). The nulling ratio measured on Vega in the N band was found to be consistent with the point-source calibrators within an uncertainty of 0.7%. This allowed for an upper limit of 2.1% to be placed on the circumstellar emission of Vega relative to its photosphere at 10.6 μm, valid for separations greater than 0.8 AU (equivalent to the resolution of BLINC at MMT).

Recently, interferometric observations of Vega with the FLUOR (Fiber Linked Unit for Recombination) instrument at the CHARA array have revealed for the first time the expected near-IR signature of a faint debris disc, accounting for 1.3 % of the stellar flux in the K band (Absil *et al.* 2006b). The resolved excess seems to emanate mostly from hot sub-micron carbonaceous grains located within 1 AU from the photosphere, close to their sublimation limit. Because such grains have a very short lifetime (a few tens of years at most), this result can be interpreted as a possible evidence for massive evaporation of cometary bodies. A dozen of comets similar to Hale-Bopp should be currently orbiting in the star's vicinity in order to permanently replenish the disc. Migration of giant planets in the young (350 Myr) Vega system could trigger such a cometary shower, in a mechanism similar to the Late Heavy Bombardment in the solar system (Gomes et al. 2005). Recent observations with the CHARA/FLUOR interferometer have brought new detections of circumstellar emission excess as high as 1-2% of the stellar flux at 2 μm around the 10 Gyr old sun-like star τ Cet (G8V) and around the young Vega-like ζ Aql (A0V), β Leo (A3V) and ζ Lep (A2V, di Folco *et al.* 2007; Absil *et al.* 2007; Akeson *et al. in prep*). At the same time, no excess was detected around several other Vega-like stars, including the sun-like K2V ϵ Eri, with a similar precision of about 0.25 %.

1.2.3 Prospects for future observations

In order to detect Kuiper belt analogs, observations with facilities other than Spitzer are necessary. For instance, the Herschel telescope will measure cold Kuiper belt discs to solar system levels while ground-based interferometers, such as the Keck Interferometer (KI, see section 2.4.2) and the Large Binocular Telescope Interferometers (LBTI, see section 2.4.3), should be able to measure the 10-μm exozodiacal emission that arises in the HZ. European projects like ALADDIN (see section 2.5.2) and Pegase (see section 3.2) are also very promising to measure the 3.5-μm emission of circumstellar disc inner regions to an unprecedented level (see a performance study of these instruments in chapter 3). With Spitzer and Herschel measuring excesses from 20 to 200 μm down to near solar system levels, KI and LBTI pushing to near solar system levels at 10 μm and hopefully ALADDIN and Pegase to probe the inner disc regions, the statistical properties of Darwin/TPF targets should be understood sufficiently well to know whether or not a population of stars with low levels of zodiacal emission exists, as the theory suggests.

1.3 Detection and characterisation techniques

1.3.1 Overview

To detect and characterise extrasolar planets, several techniques exist, some achieving the detection indirectly by effects on the host star (such as radial velocity) and others by directly detecting the photons from the planet (such as coronography and interferometry). A global view of these detection methods is presented in Figure 1.8, displaying the four main families of detection methods. These techniques are classified according to the way they can lead to the detection of a planet:

- by observing dynamical effects on the host star (radial velocity, astrometry or timing in the case of the pulsar planets);
- by microlensing effects (astrometric or photometric);
- by monitoring the photometric signals (transits and direct imaging in the visible or infrared);
- miscellaneous effects (such as magnetic super-flares or radio emission).

Each method has its own advantages and drawbacks. Figure 1.8 summarizes the results of each method in terms of planets detected. Dashed lines indicates techniques which are not yet available to detect extrasolar planets. They should provide complementary discoveries in the next years. In the next section, some ongoing and foreseen observational instruments are presented.

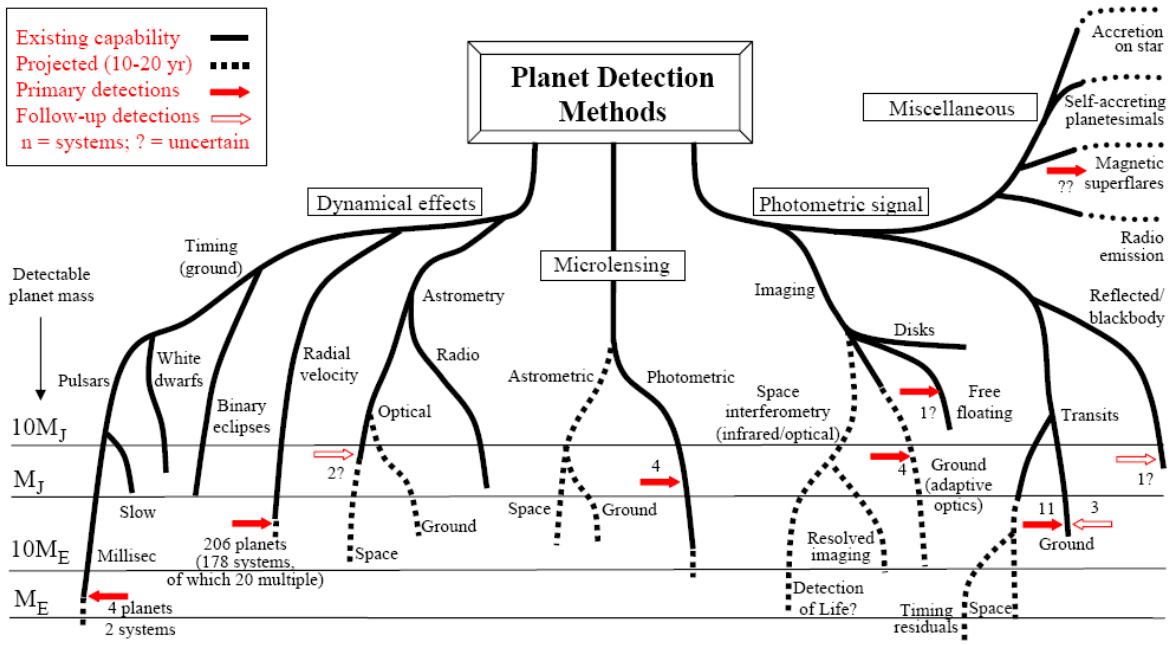

Figure 1.8: Diagram of detection and characterisation methods for extrasolar planets (updated April 2007). The lower extent of the solid lines indicates, roughly, the detectable masses that are in principle within reach with the available instruments. The expected level of detection of future instruments is shown by the dashed lines (see the mass scale on the left). The miscellaneous signatures to the upper right are less well quantified in mass terms. Solid arrows indicate (original) detections according to approximate mass, while open arrows indicate further measurements of previously detected systems. A question mark indicates uncertain or unconfirmed detections (figure from Perryman 2000).

1.3.2 Indirect detection methods

Almost all planets discovered so far have been evidenced by indirect methods, which rely on effects induced by the planet on its parent star. The most successful technique relies on precise measurements of the host star's radial velocity through spectroscopic observations, showing small shifts in the stellar spectral lines (typically a tens of meters per second) as the star moves back and forth due to the gravitational pull of its planet. Another successful technique relies on the dimming of the apparent stellar flux as the planet transits in front of the stellar disk. Even though the probability to detect such a transit is rather low (about 10% for a hot Jupiter), 24 planets have been either found or confirmed using this technique. Astrometric data are also used to detect planets. The method consists in measuring the periodic displacement in the apparent position on the sky of a star, due to the planetary gravitational influence. Ongoing or future space missions using one of these indirect techniques such as CoRoT, Kepler, GAIA and Space Interferometry Mission (SIM) promise to detect many more planets, as briefly exposed hereafter:

- **CoRoT** (Convection Rotation and planetary Transits) is a space mission led by the French Space Agency (CNES) in conjunction with the European Space Agency (ESA) and other international partners (Baglin *et al.* 2007). The mission has two objectives: searching for extrasolar planets and performing asteroseismology by measuring solar-like oscillations in stars. CoRoT consists in a 27-cm aperture telescope with a 3.5 deg^2 field of view (cf. Figure 1.9, left). For the planetary programme, five fields containing approximately 12000 dwarf stars will be continuously monitored for 150 days. CoRoT is expected to detect over 10000 planets in the 1 to 5 $R_\oplus$ range within 0.3 AU, assuming all stars have at least one such a planet (Bordé *et al.* 2003). More realistic simulations show that CoRoT will detect about 100 transiting planets down to a size of 2 $R_\oplus$ around G0V stars and 1.1 $R_\oplus$ around M0V stars.

  CoRot was launched on December 2006 and detected its first extrasolar planet (*Corot exo 1b*) in May 2007, a "hot Jupiter" orbiting a sun-like star located at about 450 pc. This planet has a radius of approximately 1.78 times that of Jupiter, a mass of approximately 1.3 times that of Jupiter, and orbits its parent star once every 1.5 days.

- **Kepler** is a discovery mission of NASA (National Aeronautic and Space Administration) designed to determine the frequency of Earth-size and smaller planets in and near the HZ of about 100000 main sequence stars (Borucki *et al.* 2007). The instrument consists of a 0.95-m aperture telescope (cf. Figure 1.9, right) able to perform high precision photometry in order to evidence the sign of a transiting planet. After 4 years, this mission (planned to start in early 2009) should have discovered several hundred terrestrial planets (i.e. planets up to twice the diameter of Earth) with periods between one day and 400 days if such planets are common. In particular, about 100 Earth-size planets in the HZ could be discovered. This number increases to 650 planets if most terrestrial planets have a size of 2 $R_\oplus$. A null result would imply that terrestrial planets are rare.

  Aside from detecting Earth-sized planets in the HZ, Kepler will advance the hot Neptune and hot Earth studies started by CoRoT, detecting up to hundreds of them down to a size as small as that of Mercury. Both Kepler and CoRoT will reveal exciting extrasolar giant planet science with tens of transiting giant planets with semi-major axes in the 0.02-1 AU range and even giant planets in orbits beyond 1 AU can be detected.

- **GAIA** is an ESA mission which intends at measuring stellar positions with a μas precision in order to make the largest and most precise three-dimensional map of the Milky Way (Crifo and The French Gaia Team 2006). For stars within a distance of approximately 50 pc from the Sun, GAIA is expected to find every Jupiter-sized planet with an orbital period of 1.5 - 9 years. Estimates suggest that GAIA will detect between 10000 and 50000 extrasolar planets (Sozzetti *et al.* 2003).

  GAIA is the acronym of Global Astrometric Interferometer for Astrophysics, a name that reflected the optical technique of interferometry, originally planned for use on this telescope. Even if the

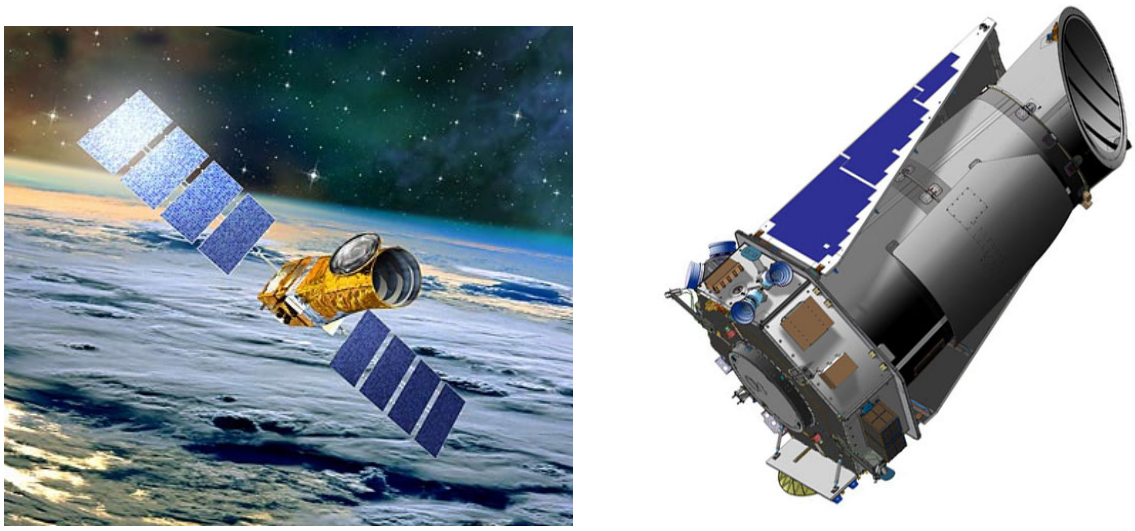

Figure 1.9: Left, CoRot, a 27-cm aperture telescope aimed at detecting short orbital period transiting planets down to the size of Earth. Right, Kepler, a 0.95-m aperture telescope aimed at detecting Earth-size planets in the habitable zone.

working method has now changed, the name of GAIA has remained.

- **SIM** (Space Interferometry Mission) is an astrometric mission that will be able to search for terrestrial planets in the HZ of nearby stars with 1 μas relative astrometric accuracy (Shao 2006). The instrument combines the light from two 30-cm aperture telescopes structurally-connected and separated by 9 m. It will use precise measurements of fringe position to determine orbits of planets with masses 0.5-5.0 times that of Earth around 220 of the closest stars. If every star had an Earth-twin orbiting in the star's HZ, then SIM could detect 6 of these Earth-twins; if the planet's mass were twice the Earth's mass, SIM could detect 30 of them. Around at least 15 stars, the detectable planets would be considered Earth twins. It will also perform a broader survey of over 2000 stars to look for planets the size of Neptune and larger.

Note that the PRIMA (Phase-Referenced Imaging and Micro-arcsecond Astrometry) instrument will also use astrometry to detect extrasolar planets. PRIMA will be an ESO's facility at the VLT Interferometer (Cerro Paranal, Chile), expected to be fully operational within a couple of years (Reffert *et al.* 2006). With PRIMA/VLTI, it will then be possible to perform relative astrometry with an accuracy of the order of 10 μas over angles of about 10$''$. The main science driver for this astrometric capability is the detection and characterization of extrasolar planets, including the observation of known radial velocity planets and planetary systems to fully constrain their orbital geometry and accurately determine the mass of the planet, a search for extrasolar planets around stars which are less suitable for the radial velocity method (for example young and active stars as well as early type stars), and a systematic search around the most nearby stars to detect low mass planets (Uranus or Neptune masses).

Figure 1.10 summarizes the sensitivity of the different ongoing or planned observational instruments, described in the previous paragraphs. In particular, it shows the improved sensitivity of Kepler with respect to CoRoT and the complementarity between radial velocity surveys and astrometric measurements. The planets of the Solar system are indicated by the first letter of their name written on a blue filled circle. Extrasolar planets already detected are also represented. Space-based instruments become critical to search for terrestrial planets in the habitable zone.

Although these future instruments for transit searches (CoRoT, Kepler) or astronomic surveys (GAIA, SIM) are expected to push the detection limit down to a few Earth masses (see Figure 1.10 for a global view of the detection capabilities), they will still be restricted to the measurements of orbital parameters and will therefore provide limited information on the physics of these supposedly rocky

Figure 1.10: Global view of the limiting sensitivity of a wide variety of space and ground-based instruments as a function of planet sizes and orbital locations. The filled circles indicate the planets found at the date of October 2006 by radial velocity surveys (blue), transit surveys (red) and microlensing surveys (yellow). Also indicated by the filled circles are pulsar planets (violet) and the companion to a young brown dwarf (dark red). Planets in our solar system are also indicated. Space-based techniques become critical to search for terrestrial planets in the habitable zone (Figure from Lawson and Traub 2006).

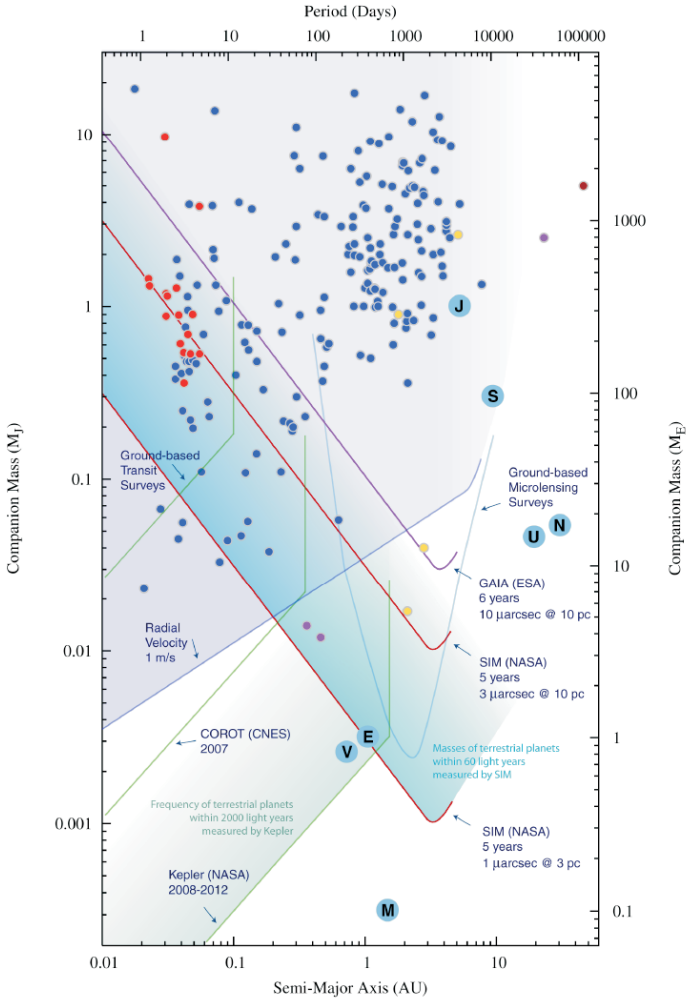

bodies. Indirect methods still have many bright years ahead, but will gradually be complemented and replaced by direct techniques, which aim at extrasolar planet imaging and could eventually lead to the detection of biosignatures.

1.3.3 Direct detection methods

Direct detection consists in acquiring directly the planetary photons. Although it is obviously the most promising way to characterise extrasolar planets, direct imaging is a very challenging task since it requires generally the suppression of the parent starlight to many orders of magnitude. To date, direct imaging of extrasolar planets has been reported in only 4 (favorable) cases where the star-planet contrast was not too high (a few hundredths) and the angular separation not too small. These discoveries have been made possible only very recently with the advent of adaptive optics (AO) systems on large ground-based telescopes. In order to improve the sensitivity to fainter and fainter planets, several techniques have been proposed, particularly coronagraphy and nulling interferometry which are very promising to accomplish this task. A coronagraph is an instrument designed specifically to block the starlight, either by an occulting disc or by an appropriate phase mask, so that nearby objects can be resolved without burning out the telescope's optics. Phase mask coronagraphs are transparent but induce spatially-distributed phase shifts with the goal of destructively rejecting the starlight (see Mawet 2006 for a detailed description of phase-mask coronagraphs). Nulling interferometry is a technique in which the beams coming from two telescopes are combined in phase opposition so that a dark fringe appears on the line of sight, which strongly reduces the starlight emission. This technique is thoroughly addressed in Chapter 2. In the following paragraphs, main space-based missions using one of these techniques are presented.

- **JWST** (James Webb Space Telescope) will be by 2013 the largest telescope operating in space, providing a wide and continuous spectral coverage from the visible (0.6 μm) to the mid-IR (28 μm, Clampin 2007). With a diameter of 6.57 m, the main objectives of JWST are the understanding of the Universe, the birth and formation of stars and their planetary systems. Using phase-mask coronagraphy, JWST is expected to enable the direct imaging of giant extrasolar planets with a temperature higher than 400 K and orbiting at 10 AU around nearby stars (Baudoz *et al.* 2006).

- **SEE-COAST** (Super-Earth Explorer - Coronagraphic Off-Axis Space Telescope) is a 1.5-m space telescope (see Figure 1.11, left), using a phase-mask coronagraph and intended at detecting and characterising extrasolar planets in the visible (Schneider *et al.* 2006). In particular, SEE-COAST should be able to image dozens of Jupiter-like planets in the 1-5 AU range around nearby stars (within 15 pc). Low-resolution spectroscopic capabilities will permit a first characterisation of their atmosphere in the visible, searching for H_2O, CH_4 and NH_3 (see Figure 1.5). It has been proposed by an European consortium, led by the University of Liège (IAGL and CSL) and the Paris-Meudon Observatory, in response to an ESA call for proposals for a small-medium mission in the framework of the ESA Cosmic Vision programme.

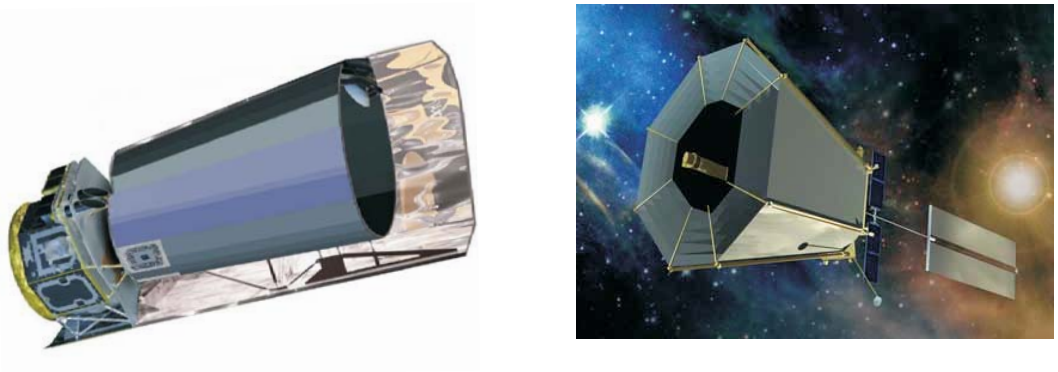

Figure 1.11: Left, artistic view of the SEE-COAST satellite concept, showing the sun-shielded off-axis 1.5 meter telescope. Right, representation of the TPF-C instrument, showing its 3.5 × 8-m elliptical single-aperture telescope .

- **TPF-C** (Terrestrial Planet Finder Coronagraph) is a NASA mission presenting a 3.5 × 8-m elliptical single-aperture telescope (see Figure 1.11, right) and using a coronagraph to suppress the stellar emission (Traub *et al.* 2006). It will observe nearby Sun-like stars in the visible to search for Earth-like planets able to support life. It will be deployed beyond the Moon's orbit for a mission lifetime of 5 years, possibly extended to 10 years. TPF-C is now in Pre-Phase A of its development.

- **Darwin** is an ESA nulling interferometer, aimed at the detection and characterisation of Earth-like extrasolar planets. During a mission lifetime of 5 years, over 200 Earth-size planets could be detected with a spectroscopic characterisation (CO_2, O_3 and H_20) for about 20 of them. Darwin achieves this sensitivity by using four 2-m telescopes operating in the infrared. The Darwin mission and its expected performance are described in details in Chapter 4.

- **TPF-I** (Terrestrial Planet Finder Interferometer) is the interferometric version of NASA Terrestrial Planet Finder missions. TPF-I is today conceived as an international collaboration with ESA's Darwin project. As Darwin, TPF-I consists in 4 telescopes working as a nulling interferometer. It has the potential to detect and characterise Earth-like planets in the infrared (Beichman *et al.* 2006a).

2

Overview of nulling interferometry

Contents

Abstract. After reviewing why interferometry is essential in modern astronomy, this chapter presents the basic principle of a specific promising method: nulling interferometry. In addition to provide the required spatial resolution, this technique offers an elegant solution to explore faint regions around a bright object (e.g. a planet around a star), relaxing the high dynamic range constraints. After a theoretical introduction, the first ground-based experiments currently under development in the United States are presented with their preliminary scientific results. Finally, two major European ground-based projects are described: the Antarctic L-band Astrophysics Discovery Demonstrator for Interferometric Nulling (ALADDIN) and the Ground-based European Nulling Interferometer Experiment (GENIE).

2.1 The need for interferometry

Interferometry appears as a natural solution to the limited resolution of classical instruments. Indeed, the angular resolution of monolithic optical instruments is limited due to the wave nature of light which is embodied in the Rayleigh's criterion, stating that the angular resolution of a telescope is ultimately diffraction limited according to $\theta = 1.22\lambda/D$, where λ is the wavelength and D the aperture diameter. For instance, the angular separation between an Earth-like planet orbiting at 1 AU from its host star located at 20 pc is 50 mas which requires at least a 30-m diameter telescope to resolve the system in the N band (8-13 μm). Similar conclusions can be drawn for the observations of the inner part of circumstellar discs. The need for higher angular resolution has led to the development of instruments with larger

and larger mirrors, finally reaching 10 m with the most recent telescopes (see the Keck description in section 2.4.2). Adaptive optic systems have been designed to achieve the full potential of these giant telescopes in terms of angular resolution, overcoming the harmful perturbations of atmospheric turbulence. However, in the mid-infrared regime, the desired angular resolution to resolve extrasolar systems can hardly be accomplished with current monolithic telescopes, where the angular resolution is limited to about 250 mas. Large telescopes, up to 100-m aperture diameter, are currently being studied but, as such large apertures are not expected to be feasible in space, they will still be limited by the presence of the Earth's atmosphere which degrades the images and restricts the observations to the infrared transparency windows (e.g. the N band).

Another way to achieve high angular resolutions without building gigantesque telescopes is to combine light beams from several telescopes in order to synthetise a larger aperture. The resolution of the instrument is then equivalent to the resolution of a single-dish telescope with a diameter equals to the distance between individual telescopes. The principle of interferometry is known since Fizeau and Foucault (1847) and the first astronomical interferometer was built on the Mount Wilson Observatory's in order to measure the diameters of stars (Michelson and Pease 1921). This method was extended to separated telescopes by Labeyrie (1975) who measured the angular size of stars with a 12-m baseline length (in the visible). Today, interferometry has become a widespread technique used in several instruments and projects (see Absil 2006 for more details).

2.2 Principle of nulling interferometry

In addition to the high angular resolution necessary to study extrasolar systems, another major difficulty is the luminosity contrast between the science object (e.g. planet, disc) and the host star. For instance, the luminosity contrast between Earth and the Sun is about 10^{-10} in the visible and 10^{-7} in the mid-infrared. Unfortunately, the dynamic range of state-of-the-art stellar interferometers, a few 0.1% (Absil 2006), is not sufficient and only bright debris discs can be investigated.

In that context, Bracewell (1978) proposed nulling interferometry as a solution to detect directly extrasolar planets. The basic principle of nulling interferometry is to combine the beams coming from two telescopes in phase opposition so that a dark fringe appears on the line of sight, which strongly reduces the starlight emission (see Figure 2.1). The response of this simple interferometer on the plane of the sky is a series of sinusoidal fringes, with angular spacing of λ/b which lets through the light from an off-axis source by adjusting the baseline length (see Figure 2.1, right). As the baseline is rotated in the plane perpendicular to the star direction, the star remains nulled, and the planet moves through peaks and nulls of the response, giving an output photon rate that is modulated in time. Appropriate demodulation of this output gives the flux of the planet and the position relative to the star. The rationale of the Bracewell's proposal was already based on the limited performances of indirect techniques (astrometry, radial velocity) and on the inability of "direct photography" to detect small and faint extrasolar planets around bright stars. The purpose of the initial proposal was the detection of Jupiter-like planets in the far-infrared (40 μm) with a moderate interferometer baseline (7.7 m), but the key features of future missions for Earth-like planet detection were already included.

The idea proposed by Bracewell has led to the definition of the so-called "Bracewell" interferometer, meaning two-telescope nulling interferometer. The primary disadvantage of the single Bracewell configuration is that the response on the sky is symmetric on either side of the star. As a result, the planet position angle has a 180° ambiguity, it is difficult to separate the planet signal from other sources of emission and it is not possible to implement phase chopping (see section 2.3). A number of interferometer configurations with more than two collectors have been proposed to overcome these limitations (Angel and Woolf 1997; Mennesson and Mariotti 1997; Absil 2001). In the following section, the generic response of these configurations are presented.

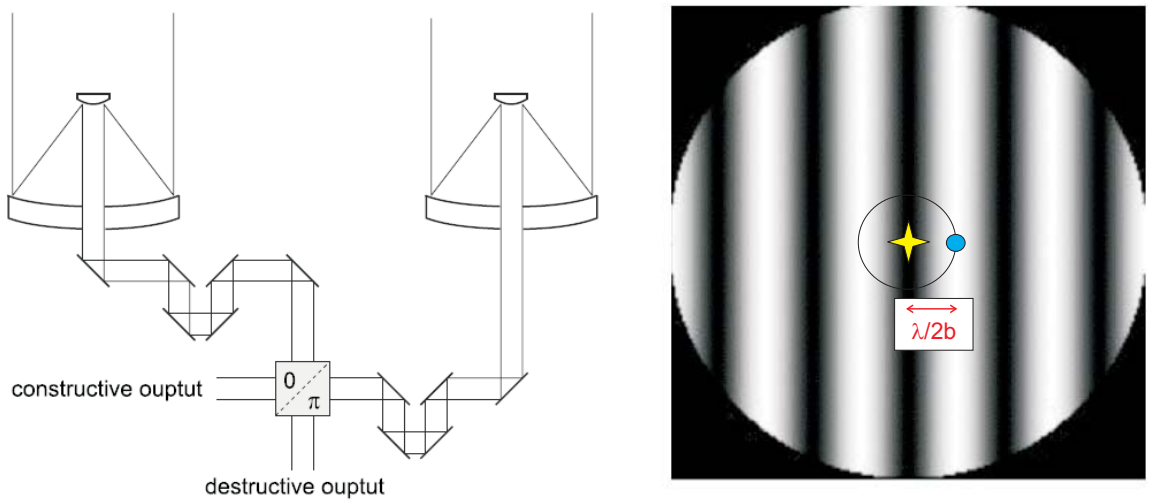

Figure 2.1: Schematic configuration of a Bracewell interferometer (left figure, from Absil 2006) with the corresponding response on the sky (right figure). The beam-combining system produces a destructive interference by applying an achromatic π phase shift to one of the two input beams and by superposing them in a co-axial way. At an angular distance $\lambda/2b$ (λ is the wavelength and b the baseline length) from the line-of-sight, the interference is constructive and a planet located at this position is fully transmitted.

2.2.1 Instrument response

The method described in this section to derive the instrument response relies on the full analytical study of Lay (2004). This method has the advantage to be easily applicable to any interferometer configuration, represented in a generic way in Figure 2.2. The final detection of output photons of a nulling interferometer can be done either in a pupil plane or in an image plane. In the first case, a single-pixel detector is sufficient to record the total flux in the output pupil, emanating from all the sources in the diffraction limited field-of-view. In the latter, an image similar to that of a single telescope is formed, except that the relative contribution of each source is affected by the interferometer's intensity response at its location. In any case, no fringe is formed nor recorded, and the final output generally consists of a single value: the total intensity in the diffraction-limited field-of-view. On output of the interferometer, the total detected photon rate (excluding stray light[4]) can be written as:

$$N = \int_{\theta}\int_{\alpha} B_{\rm sky}(\mathbf{s})R(\mathbf{s})P(\mathbf{s})\,\theta d\theta d\alpha\,, \tag{2.1}$$

where $B_{\rm sky}$ is the brightness distribution on the sky for a spectral channel centered on wavelength λ and a bandwidth $\Delta\lambda \ll 1$ (units in photons/s/m^2), $\mathbf{s}$ is a unit vector whose direction represents position on the sky, $\mathrm{P}(\mathbf{s})$ is a field-of-view taper function resulting from the size of a collecting aperture and the input response of the single-mode spatial filter (equals to 1 on axis) and $R(\mathbf{s})$ is the intensity response of the interferometer on the sky (excluding the taper), the so-called transmission map.

To deduce the transmission map, the first step is to compute the expression of the electric field produced by a point source of unit flux at position $\mathbf{s}$. Due to the linearity of the Maxwell's equations, the result is simply given by the sum over the contributions from each collector:

$$r(\mathrm{s}) = \sum_j A_j \exp\left[i\left(\phi'_j + \frac{2\pi}{\lambda}\mathbf{x_j}\cdot\mathbf{s}\right)\right]\,, \tag{2.2}$$

[4]Stray light is made of the photons originating from outside the interferometer and which do not follow the nominal route to the detector. It includes scattered light from the target and thermal photons from the instrument.

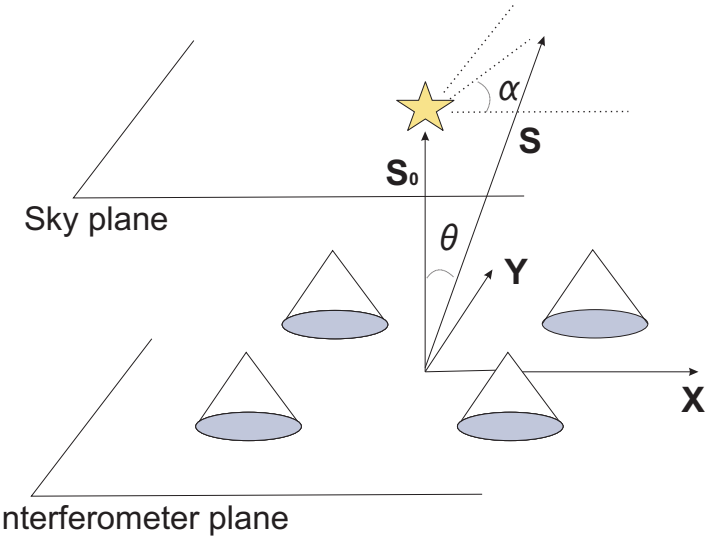

Figure 2.2: Schematic of a generic nulling interferometer and target system. The two angular coordinates (θ, α) denote the position in the sky plane.

where j is the index identifying the collector, i is the imaginary unit, A_j is the electric field amplitude response for collector j, scaled such that A_j^2 represents the detected photon rate from a source with a flux of 1 photon/m^2 (including the beam combiners), ϕ'_j is the relative phase shift for collector j and x_j the vector position for the center of collector j. The transmission map is then given by:

$$\begin{aligned} R(\mathbf{s}) &= rr^* = \left\{ \sum_j A_j \exp\left[i \left(\phi'_j + \frac{2\pi}{\lambda} \mathbf{x_j} \cdot \mathbf{s} \right) \right] \right\} \times \left\{ \sum_k A_k \exp\left[-i \left(\phi'_k + \frac{2\pi}{\lambda} \mathbf{x_k} \cdot \mathbf{s} \right) \right] \right\} \\ &= \sum_j \sum_k A_j A_k \cos\left(\phi'_j - \phi'_k + \frac{2\pi}{\lambda} (\mathbf{x_j} - \mathbf{x_k}) \cdot \mathbf{s} \right) . \end{aligned} \tag{2.3}$$

This expression represents the interference pattern and defines which parts of the field-of-view is transmitted by constructive interference, and which are blocked by destructive interference. To be specific, the transmission of a single Bracewell interferometer (2 telescopes, ϕ'_1=0, $\phi'_2 = \pi$, A_1=A_2=A) writes:

$$R(\theta, \alpha) = 4A^2 \sin^2\left(\pi \frac{b\theta}{\lambda} \cos\alpha \right) , \tag{2.4}$$

taking into account that $(\mathbf{x_2} - \mathbf{x_1}) \cdot \mathrm{s} = b\theta \cos\alpha$ with b the baseline length and (θ, α) denoting the position in the sky plane. The resulting transmission map is represented in Figure 2.3 (left) for a Bracewell interferometer with 2-m telescopes. The baseline length which would locate a planet (at an angular distance θ_p from its host star) is then given by $b = \lambda/(2\theta_\mathrm{p})$.

The right part of Figure 2.3 shows the transmission map of a 4-telescope nulling interferometer with 2-m mirrors. This configuration is referred to as X-array and is the current baseline configuration for the Darwin mission (see chapter 4 for more details). For both transmission maps, the ratio λ/b has been fixed at 5×10^{-7} representing for example a nulling interferometer working at 10 μm with a nulling baseline length of 20 m. In theory, there is no real limitation to the field-of-view of a nulling interferometer, although the crests and troughs of the transmission map wash out for angular distances larger than $\lambda^2/(b\Delta\lambda)$ due to the effect of the finite bandwidth.

Substituting the expression of the transmission map (see Equation 2.3) in Equation 2.1, the expression of the output intensity writes:

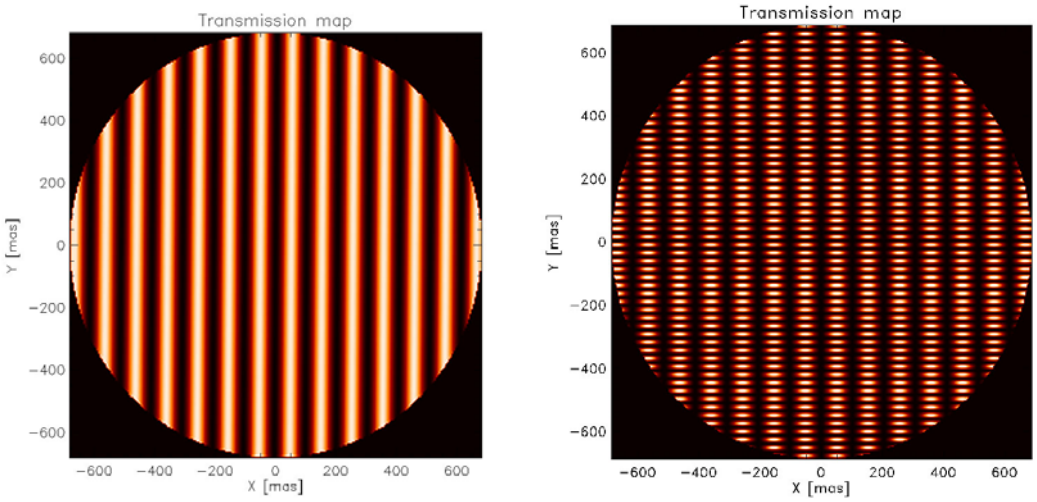

Figure 2.3: Left, monochromatic transmission map for a Bracewell interferometer formed by two 2-m telescopes for a factor λ/b fixed at 5×10^{-7} (corresponding for example to λ=10 μm and a baseline length of 20 m). The transmitted parts of the field are indicated by bright stripes while those that are blocked by dark stripes, including the central dark fringe. Right, monochromatic transmission map for a 4-telescope nulling interferometer with 2-m mirrors with an aspect ratio of 4 (the long baseline length is 4 times larger than the short). This configuration is referred to as X-array and is the current configuration for the Darwin mission (see chapter 4 for more details).

$$N = \sum_j \sum_k A_j A_k \Bigg\{ \cos(\phi_j - \phi_k) \iint B_{\mathrm{sky,sym}}(\theta,\alpha) P(\theta) \cos\left(\frac{2\pi}{\lambda}[b_{jk}\cos\alpha]\right) \theta d\theta d\alpha$$
$$- \sin(\phi_j - \phi_k) \iint B_{\mathrm{sky,asym}}(\theta,\alpha) P(\theta) \times \sin\left(\frac{2\pi}{\lambda}[b_{jk}\cos\alpha]\right) \theta d\theta d\alpha \Bigg\}, \tag{2.5}$$

where $b_{jk} = (x_{jk}^2 + y_{jk}^2)^{0.5}$ is the length of the projected baseline between collectors j and k and $B_{\mathrm{sky,sym}}$ (resp. $B_{\mathrm{sky,asym}}$) is the symmetric (resp. asymmetric) part of the sky brightness distribution. The double integrals are two-dimensional Fourier transforms of the sky brightness distribution, including the field-of-view taper, which are denoted by a horizontal bar:

$$N = \sum_j \sum_k A_j A_k \left[\cos(\phi_j - \phi_k)\overline{B}_{\mathrm{sky,jk,sym}} - \sin(\phi_j - \phi_k)\overline{B}_{\mathrm{sky,jk,asym}}\right] . \tag{2.6}$$

The total photon rate is therefore a sum over all possible pairs of collectors. If a baseline has a phase difference of 0, $\pm\,\pi$ or $\pm\,2\pi$, then its contribution to the photon rate comes entirely from the symmetric brightness distribution while a baseline with a phase difference that is an integer multiple of $\pi/2$ couples entirely to the asymmetric brightness distribution (like a planet). This total photon rate on output contains the contributions from the planet (N_{planet}), star (N_*), exo-zodiacal cloud (N_{EZ}), local zodiacal cloud (N_{LZ}), stray light and any solar photons that are scattered into the instrument (N_{stray}), and instrumental thermal emission (N_{thermal}). Therefore, it can also be written as:

$$\begin{aligned} N &= N_{\mathrm{planet}} + N_* + N_{\mathrm{EZ}} + N_{\mathrm{LZ}} + N_{\mathrm{stray}} + N_{\mathrm{thermal}} \\ &= N_o + \delta N\,, \end{aligned} \tag{2.7}$$

where the second equality indicates that the photon rate at the detector can be written as the sum of the photon rate for an ideal instrument without perturbations (N_o) and the additional photon rate that is due to perturbations (δN, the "perturbation leakage"). These two terms are addressed separately in the following sections.

2.2.2 Geometric leakage

Even for an ideal instrument, photons from the different sources leak through the interferometer (as illustrated in Figure 2.4, left). The main sources have characteristic contributions described hereafter:

- The planet can be represented by a point-like δ function in Equation 2.5 and has both symmetric and asymmetric components:

$$N_p = F_p \sum_j \sum_k A_j A_k \Bigg\{ \cos(\phi_j - \phi_k) \cos\left(\frac{2\pi}{\lambda}[b_{jk}\theta_p \cos\alpha_p]\right) - \sin(\phi_j - \phi_k) \sin\left(\frac{2\pi}{\lambda}[b_{jk}\theta_p \cos\alpha_p]\right)\Bigg\}, \tag{2.8}$$

  where F_p is the flux from the planet and (θ_p, α_p) its position on the sky.

- If the star is assumed center symmetric, the stellar contribution to the detected photon rate is given by:

$$N_\star \approx \sum_j \sum_k A_j A_k \cos(\phi_j - \phi_k) \overline{B}_{\star jk}\,. \tag{2.9}$$

  Assuming also that the stellar brightness is distributed over a uniform circular disc, the Fourier transform is then given by:

$$\overline{B}_{\star jk} = 2F_\star J_1\left(\frac{2\pi b_{jk}\theta_*}{\lambda}\right) \Bigg/ \frac{2\pi b_{jk}\theta_*}{\lambda}\,, \tag{2.10}$$

  where $F_\star$ is the stellar flux at wavelength λ over the bandwidth $\Delta\lambda$, J_1 is the first kind Bessel function and $\theta_\star$ is the stellar angular diameter.

- The exozodiacal dust emission is orders of magnitude fainter than the star, but cannot be nulled efficiently since it extends into the HZ. The detected photon rate can be calculated with Equation 2.6:

$$N_{\rm EZ} \approx \sum_j \sum_k A_j A_k \cos(\phi_j - \phi_k) \overline{B}_{{\rm EZ}jk}\,. \tag{2.11}$$

  assuming here again that the brightness distribution is center symmetric.

- The local zodiacal dust is a uniform and incoherent foreground source of photons. It can be calculated with the symmetric part of Equation 2.5, leading to:

$$N_{LZ} = B_{LZ} \sum_j A_j^2 \Delta\Omega_j\,, \tag{2.12}$$

  with $\Delta\Omega_j$ being the effective solid angle of the collector beam pattern. For the local zodiacal dust, the photon rate depends only on the amplitudes (no phase or baseline dependence).

Finally, the geometrical leakage (N_g) is defined as the part of the sky brightness distribution that "leaks" through the ideal instrument (except the planetary signal, N_p) and can be derived using Equations 2.9, 2.11 and 2.12:

$$\begin{aligned} N_g &= N_o - N_p \\ &= \sum_j \sum_k A_j A_k \cos(\phi_j - \phi_k)(\overline{B}_{*jk} + \overline{B}_{EZjk}) + B_{LZ} \sum_j A_j^2 \Delta\Omega_j\,. \end{aligned} \tag{2.13}$$

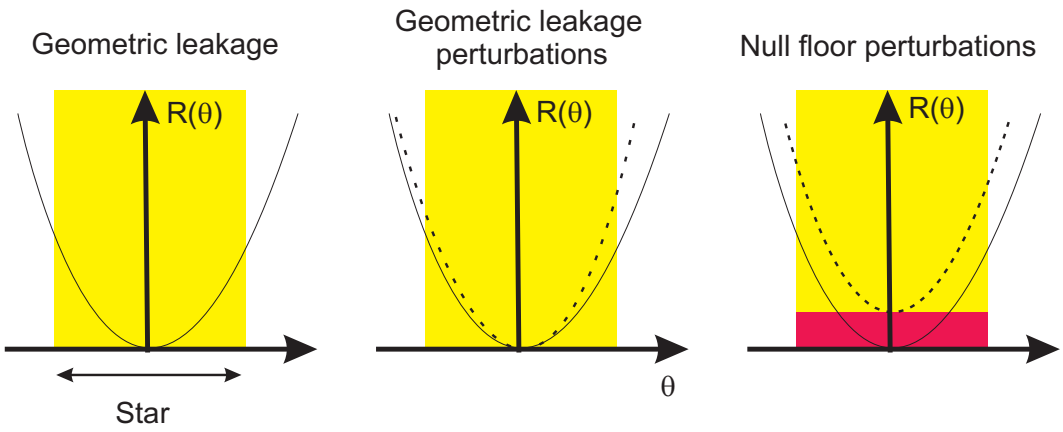

Figure 2.4: Schematic representation of different contributions to the detected photon rate on the output of a nulling interferometer (figure adapted from Lay 2004, see main text for further information).

Considering a Bracewell interferometer and assuming that the emissions of the exozodiacal and local zodiacal clouds are negligible with respect to the star, the geometrical leakage is given by:

$$N_g = 4F_\star A^2 \left(\frac{2\pi b\theta_\star}{4\lambda}\right)^2 , \tag{2.14}$$

taking into account that $J_1(x)/x \simeq 1-(x/4)^2$ for $x \ll 1$. Useful quantities to characterise a nulling interferometer is the geometric nulling ratio G, defined as the ratio between the transmitted flux and the initial flux at the input of the beam-combiner (flux coming from both telescopes), and its corresponding rejection factor ρ_g, defined as the inverse of the nulling ratio:

$$G = \frac{N_g}{2F_\star A^2} = \frac{\pi^2}{4}\left(\frac{b\theta_\star}{\lambda}\right)^2 ; \quad \rho_g = \frac{4}{\pi^2}\left(\frac{\lambda/b}{\theta_\star}\right)^2 . \tag{2.15}$$

These quantities depend on two parameters: the wavelength-baseline ratio, which sets the angular resolution of the interferometer, and the angular radius of the star ($\theta_\star$). The rejection factor decreases for longer baselines (or shorter wavelengths) as the stars gets more and more resolved.

2.2.3 Sensitivity to perturbations

If the instrument is ideal, the total photon rate on output of a nulling interferometer would be given by the sum of expression 2.13, the geometrical leakage, and expression 2.8. In practice, the photon rate is affected by instrumental perturbations, such as intensity, Optical Path Difference (OPD) and/or pointing errors. For the stellar emission, the contributions of each perturbation can be assessed by deriving Equation 2.9 to the second order:

$$\begin{aligned}
\delta N_\star \;\approx\; & \sum_j \left[\frac{\partial N_\star}{\partial A_j}\delta A_j + \frac{\partial N_\star}{\partial \phi_j}\delta\phi_j + \frac{\partial N_\star}{\partial x_j}\delta x_j + \frac{\partial N_\star}{\partial y_j}\delta y_j\right] + \sum_j\sum_k \left[\frac{1}{2}\frac{\partial^2 N_\star}{\partial A_j \partial A_k}\delta A_j\delta A_k \right. \\
& \left. + \frac{\partial^2 N_\star}{\partial A_j \partial \phi_k}\delta A_j\delta\phi_k + \frac{1}{2}\frac{\partial^2 N_\star}{\partial \phi_j \partial \phi_k}\delta\phi_j\delta\phi_k\right] \\
\approx\; & \sum_j \left(C^\star_{Aj}\delta a_j + C^\star_{\phi j}\delta\phi_j + C^\star_{xj}\delta x_j + C^\star_{yj}\delta y_j\right) + \sum_j\sum_k [C^\star_{AAjk}\delta a_j\delta a_k + C^\star_{A\phi jk}\delta a_j\delta\phi_k \\
& + C^\star_{\phi\phi jk}\delta\phi_j\delta\phi_k] ,
\end{aligned} \tag{2.16}$$

defining $\delta a_j = \delta A_j/A_j$ and $C^\star$, the sensitivity coefficients for the star which can be written as:

$$C^{\star}_{Aj} = A_j \frac{\delta N_\star}{\delta A_j} \approx 2A_j \sum_k A_k \cos(\phi_j - \phi_k)\overline{B}_{*jk}\,, \tag{2.17}$$

$$C^{\star}_{\phi j} = \frac{\delta N_\star}{\delta \phi_j} \approx -2A_j \sum_{k\neq j} A_k \sin(\phi_j - \phi_k)\overline{B}_{*jk}\,, \tag{2.18}$$

$$C^{\star}_{xj} = \frac{\delta N_\star}{\delta x_j} \approx 2\sum_k A_j A_k \cos(\phi_j - \phi_k)\frac{\partial \overline{B}_{*jk}}{\partial x_j}\,, \tag{2.19}$$

$$C^{\star}_{yj} = \frac{\delta N_\star}{\delta x_j} \approx 2\sum_k A_j A_k \cos(\phi_j - \phi_k)\frac{\partial \overline{B}_{*jk}}{\partial y_j}\,, \tag{2.20}$$

$$C^{\star}_{AAjk} = \frac{1}{2} A_j A_k \frac{\delta^2 N_\star}{\delta A_j \delta A_k} \approx A_j A_k \cos(\phi_j - \phi_k)\overline{B}_{*jk}\,, \tag{2.21}$$

$$C^{\star}_{A\phi jk} = A_j \frac{\delta^2 N_\star}{\delta A_j \delta \phi_k} \approx \begin{cases} 2A_j A_k \sin(\phi_j - \phi_k)\overline{B}_{*jk} & j \neq k \\ -2A_j \sum_l A_l \sin(\phi_j - \phi_l)\overline{B}_{*kl} & j = k \end{cases} \tag{2.22}$$

$$C^{\star}_{\phi\phi jk} = \frac{1}{2}\frac{\delta^2 N_\star}{\delta \phi_j \delta \phi_k} \approx \begin{cases} A_j A_k \cos(\phi_j - \phi_k)\overline{B}_{*jk} & j \neq k \\ -A_j \sum_l A_l \cos(\phi_j - \phi_l)\overline{B}_{*kl} & j = k \end{cases} \tag{2.23}$$

The second order is necessary since the amplitudes and phases are chosen to null the stellar photon contribution, leading to first order derivatives close to 0. Considering the other contributors to the photon rate, the "perturbation leakage" δN is given by

$$\delta N \approx \sum_j (C_{Aj}\delta a_j + C_{\phi j}\delta\phi_j + C_{xj}\delta x_j + C_{yj}\delta y_j) + \sum_j \sum_k [C_{AAjk}\delta a_j \delta a_k + C_{A\phi jk}\delta a_j \delta\phi_k + C_{\phi\phi jk}\delta\phi_j\delta\phi_k]\,, \tag{2.24}$$

where C is the global sensitivity factor, which can be computed similarly for other sources with Equations 2.17 to 2.23. As illustrated in Figure 2.4, the perturbations lead to two classes of leakage : "geometric leakage perturbations" and "null-floor leakage". Geometric leakage perturbations arise from the linear terms in Equation 2.24 while the null-floor perturbations arise from the nonlinear terms.

Phase chopping techniques (described in the following section) allow for the subtraction of the null-floor leakage, which is the same in the two chopped states provided that there is no systematic difference between them. The null floor will therefore contribute only as an additional source of shot noise. On the other hand, most of the instrumental noise is not suppressed by phase chopping, as proven by Lay (2004). This contribution, referred to as instability noise (previously "systematic error" or "variability noise"), is dominated by nonlinear, second order terms related to the perturbations in the amplitudes, phases and polarisation angles of the electric fields from each telescope. Three independent studies have been dedicated to instability noise (Lay 2004; d'Arcio 2005; Chazelas *et al.* 2006), which is also briefly discussed in the context of Darwin in section 4.2.

2.3 The need for chopping

Even if the stellar emission is sufficiently reduced, it is generally not possible to detect Earth-like planets with a static array configuration, particularly due to the dominant exozodiacal emission. This is the reason why Bracewell proposed to rotate the interferometer such that the planet signal would then be

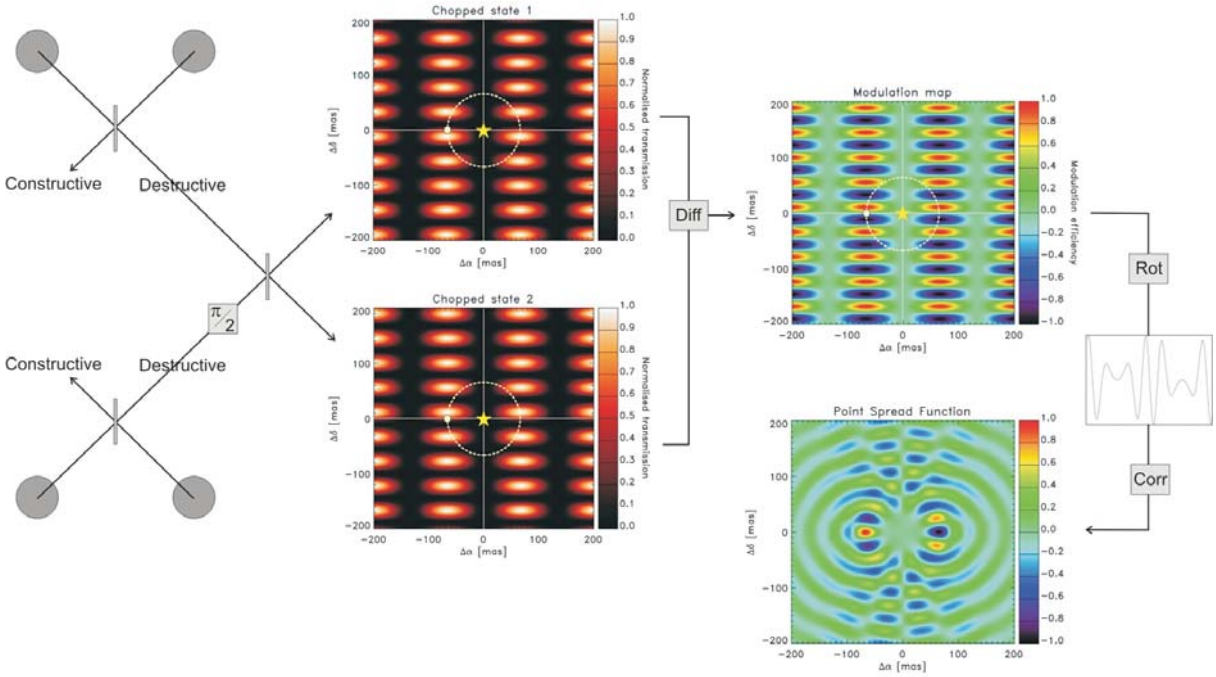

Figure 2.5: Overview of phase chopping for the X-array configuration, the current baseline for the Darwin mission (see Chapter 4). Combining the beams with different phases produces two conjugated transmission maps (or chopping states), which are used to produce the modulation map. Array rotation then locates the planet by cross-correlation of the modulated chopped signal with a template (Courtesy O. Absil).

temporally modulated by alternatively crossing high and low transmission regions, while the stellar signal and the background emission remain constant (except for the exozodiacal emission). The planetary signal could then be retrieved by synchronous demodulation. The first array configurations designed to separate the planetary signal from the exozodiacal emission have been proposed by Angel and Woolf (1997) and by Mennesson and Mariotti (1997). The former relied on the strong modulation of the exozodiacal emission at twice the interferometer rotation frequency (due to its symmetry), while the latter suggested to break the central symmetry of the interferometer, for example by using five telescopes regularly located on a circle or on an ellipse. However, since the rotation of the array can not be implemented sufficiently fast, this observing scenario is highly vulnerable to low frequency drifts in the stray light, thermal emission, and detector gain. To perform faster modulation and overcome this problem, the technique of phase chopping has been proposed in 1997 by J.-M. Mariotti (Mennesson *et al.* 2005). The principle of phase chopping is to synthetise two different transmission maps with the same telescope array, by applying different phase shifts in the beam combination process (see Figure 2.5). By quickly switching between the two different transmission maps, it is possible to modulate the planet signal without modulating the stellar, local zodiacal cloud, exozodiacal cloud, stray light, thermal, or detector gain contributions to the noise. Phase chopping can be implemented in various ways (e.g. inherent and internal modulation, see Absil 2006), and are now an essential part of the future space-based planet finding missions.

Figure 2.5 illustrates the principle of phase chopping. The outputs of two Bracewell interferometers are combined with opposite phase shifts ($\pm\,\pi/2$) to produce two transmission maps (or "chopped states"). Taking the difference of the photon rates obtained in the two chopped states gives the chopped response of the array (R_c), given by:

$$R_c(\theta,\alpha) = \frac{1}{2}[R_L(\theta,\alpha) - R_R(\theta,\alpha)]\,, \tag{2.25}$$

where R_L and R_R are the two chopped states. The factor $1/2$ accounts for the fact that the instrument

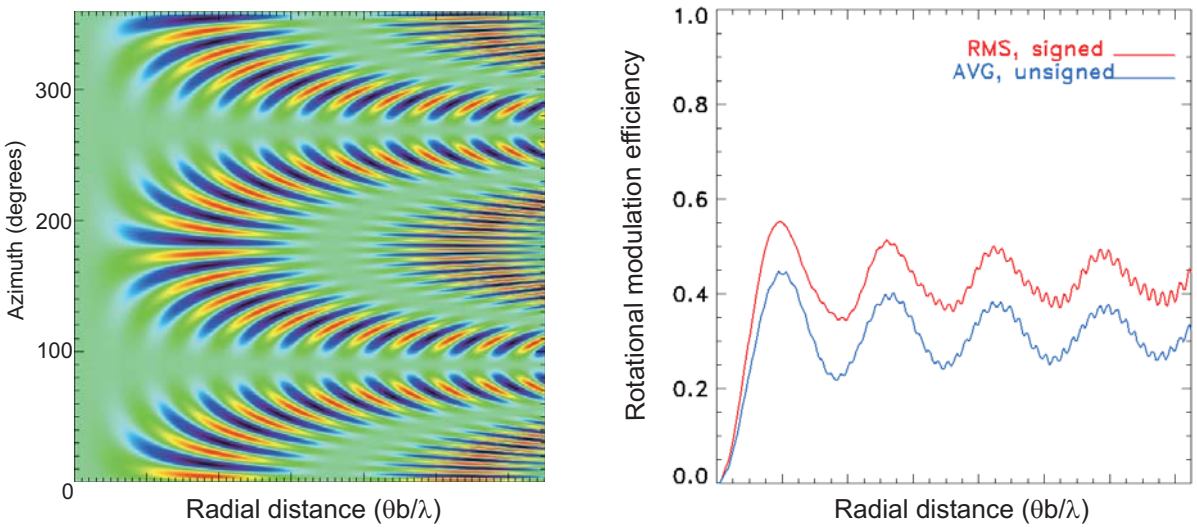

Figure 2.6: Left, modulation map of the X-array configuration in polar coordinates. Right, corresponding rotational modulation efficiency (red curve, labelled "rms signed"). The blue curve (labelled "avg unsigned") indicates the mean value of the modulation map absolute value (see main text for further information).

spends only half the time in each chop state. The chopped response (R_c) is the so-called modulation map, which can be negative by construction. Since the value of the modulation map varies across the field-of-view, the position of the planet cannot be unambiguously inferred and an additional level of modulation is mandatory. This is provided by the rotation of the interferometer (typically with a period of 1 day). The two levels of modulation (chopping and rotation) allow to define the concept of "rotational modulation efficiency", which indicates the part of the incoming signal which is actually modulated and thus retrievable by synchronous demodulation. The rotational modulation efficiency for the X-array configuration is about 50%, depending on the radial distance as shown in Figure 2.6 (right). The left part of Figure 2.6 show the modulation map in polar coordinates, so that at each abscissa corresponds to a complete rotation of the interferometer. Note that the rotational modulation efficiency for several array configurations has been investigated by Lay (2005).

The variation of the chopped planet photon rate with the rotation angle of the array appears at the right of Figure 2.5. Finally, the most common approach applied to retrieved the planet is correlation mapping, a technique closely related to the Fourier transform used for standard image synthesis (Lay 2004). The result is a correlation map, displayed for a single point source in the low right part of Figure 2.5. This represents the Point Spread Function (PSF) of the array. This process, illustrated here for a single wavelength, is repeated across the waveband, and the maps are co-added to obtain the net correlation map. The broad range of wavelengths planned for Darwin greatly extends the spatial frequency coverage of the array, suppressing the side lobes of the PSF.

2.4 First ground-based nulling instruments

2.4.1 BLINC at the MMT

The BracewelL Infrared Nulling Cryostat (BLINC) is a nulling interferometer installed on the Multi-Mirror Telescope (MMT, Mont Hopkins, Arizona). It was first installed on the segmented version of the MMT, using the beams from two of its 1.8-m segments (Hinz *et al.* 1998b), and produced first scientific results on late-type giant stars around which dust outflows were detected (Hinz *et al.* 1998a). After the refurbishment of the MMT in 1999, BLINC was re-installed on the new 6.5-m monolithic telescope (Hinz et al. 2000). It uses the two parts of the MMT's 6.5-m primary mirror to create an interferometer with

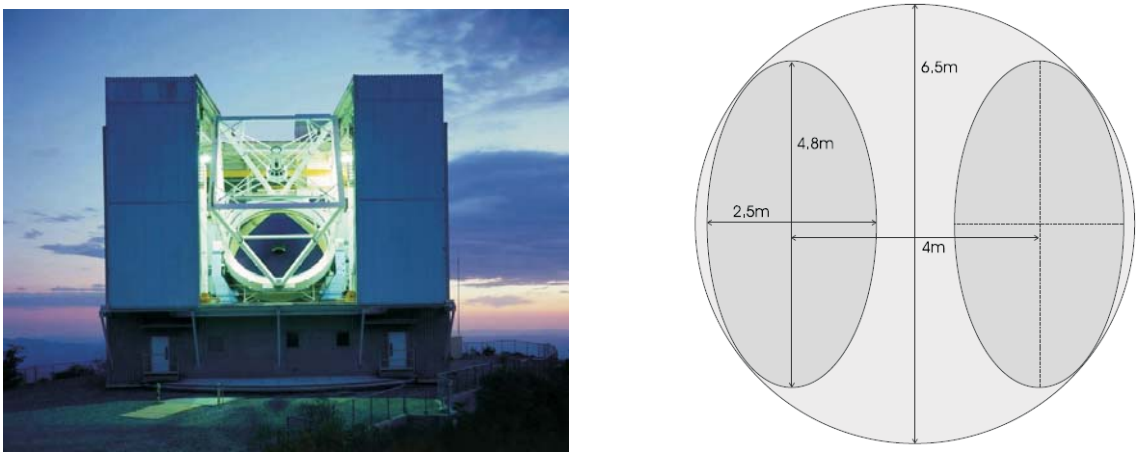

Figure 2.7: Left, picture of the Multi-Mirror Telescope (MMT, Mont Hopkins, Arizona). Right, division of the MMT pupil by the BLINC instrument to artificially produce a baseline of 4 m between two oval sub-pupils and perform destructive beam combination (figure from Absil 2006).

two elliptical 4.8 × 2.5-m sub-apertures and a baseline length of 4 m (see Figure 2.7). These two sub-apertures are overlapped in the pupil plane in order to destructively interfere the central point source in the image plane. Nulling interferometry is implemented in combination with the MMT's adaptive optics (AO) secondary mirror. The addition of AO has benefits for nulling, providing correction of atmospheric wavefront aberrations in the incoming light which allows destructive interference to be precisely tuned for the deepest possible suppression of starlight. However, despite adaptive optics, the performance of BLINC is limited to about 3% in null depth because of mechanical vibrations. Theoretically, a null depth of a few tenths of a percent would be achievable. This level of performance should be reached when the internal servo loop for active correction of phase difference in K band will become operational.

A null depth of about 10^{-3} in the N band should enable the detection of exozodiacal discs about 50 to 100 times as dense as the solar zodiacal disk. For instance, the BLINC instrument has obtained nice results on Young Stellar Objects (YSO) and Vega-type stars (Liu *et al.* 2003, 2004, 2005, 2007). Using the refined nulling observations, the BLINC team is planning a survey of nearby main-sequence A-type stars to search for evidence of exozodiacal dust. Note that the BLINC instrument has also been used in the southern hemisphere, at the Magellan I (Baade) telescope.

2.4.2 Keck Interferometer Nuller (KIN)

The Keck Interferometer (KI, Colavita *et al.* 2006) is a NASA-funded ground-based interferometer located at the summit of Mauna Kea, Hawaii (see Figure 2.8, left). Its primary goal is the characterization of the exozodiacal dust distribution close to nearby stars (0.1 - 1 AU) and the detection of hot Jupiter-like planets. KI combines light from the two 10-m aperture telescopes of Keck (the world's largest optical telescopes). The mirrors are composed of 36 hexagonal segments that work in concert as a single piece of reflective glass. It presents a 85-m baseline length, corresponding to a spatial resolution of 5 mas at 2.2 μm, and 24 mas at 10 μm. The sub-systems of the interferometer include adaptive optics, laser metrology to control optical delay lines, and fringe tracking to measure the interference in the combined light from the two telescopes. In its most sensitive configuration, the interferometer would reach magnitudes of K=21 and N=10 in about 1000 seconds of integration. KI achieved its first fringes in 2001 and an interferometric null of 1% in 2005, a milestone in the development of planet-finding technology. Several scientific observations using the nulling mode have been reported recently (Serabyn *et al.* 2006). The objective is to achieve exozodiacal disc detection at the 30-zodi level around G2V stars located at 10 pc. This level of performance requires a deep and stable instrumental null depth of at least 0.1% at 10 μm. The current activities are focused on improving performance both in null depth and sensitivity,

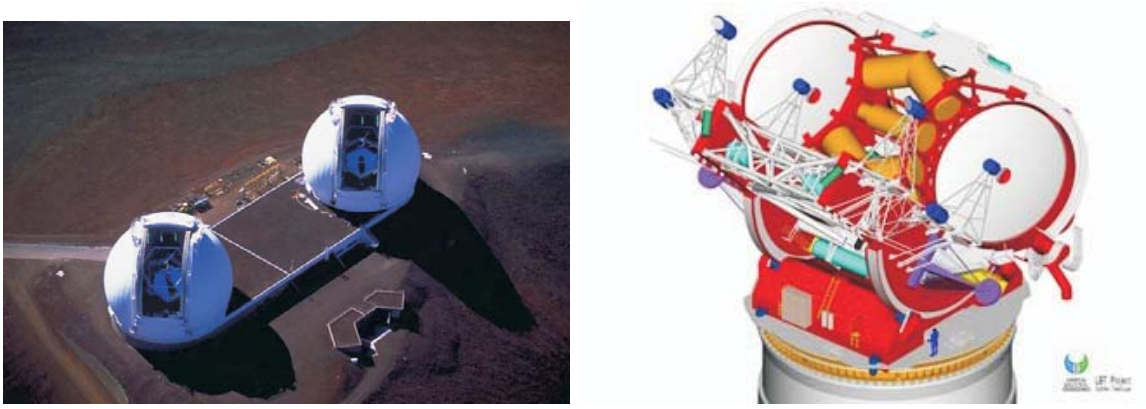

Figure 2.8: Left, picture of the Keck interferometer (Mauna Kea, Hawai). Right, artist concept of the fully assembled Large Binocular Telescope Interferometer (LBTI, Mont Graham, Arizona).

increasing functionality and operability in preparation for formal commissioning in 2007.

2.4.3 Large Binocular Telescope Interferometer (LBTI)

The Large Binocular Telescope Interferometer (LBTI) is a ground-based interferometer currently under development by the University of Arizona and located at Mont Graham, Arizona. LBTI combines the light from two 8.4-m telescopes placed side by side (14.4 m apart) on a single rigid alt-azimuth mount (see Figure 2.8, right) in the infrared. The resulting instrument will have a maximum baseline of 22.8 meters. Because of its unique geometry and relatively direct optical path, the LBTI will offer science capabilities that are different from other interferometers. Its major science objectives are similar to those of KI. Nulling techniques will enable the LBTI to examine and describe the dust and planets around nearby planetary systems, as well as detect Jupiter-like planets in orbit within these systems. With its short baseline, it provides an angular resolution of 70 mas in the midinfrared, which corresponds to the typical angular size of HZs around nearby G-type stars. As a consequence, LBTI is complementary to KI because it will enable to explore regions that are more remote from a star (1.0-10 AU). LBTI and KI will thus work together to fully describe the environment and the hottest planets in nearby systems.

2.5 The European effort

2.5.1 GENIE

GENIE (Ground-based European Nulling Interferometer Experiment, Gondoin *et al.* 2004) is a nulling interferometer conceived as a focal instrument for the VLTI (Cerro Paranal, Chile) which has been studied by ESA at the phase A level. GENIE was intended as a next step toward Darwin but has been unfortunately put on hold by ESA and ESO. The objectives of the GENIE project were twofold. From a technological and operational point of views, the goal was to advance and mature the experience on designing, manufacturing and operating a nulling interferometer, employing Darwin representative concepts and technologies. From a scientific point of view, the objective was to perform a systematic survey of candidate targets for Darwin in order to detect bright exozodiacal dust discs around nearby solar type stars. GENIE would have benefitted from the existing VLTI infrastructure including 8-m Unit Telescopes (UT) and 1.8-m Auxiliary Telescopes (AT) with chopping, adaptive optics, delay lines, fringe sensors and a beam combiner laboratory. The overall capabilities of the instrument heavily depend on the performance of all VLTI sub-systems and in particular on the adaptive optics and co-phasing sub-systems. The GENIE optical bench within the VLTI laboratory would have provide the functions

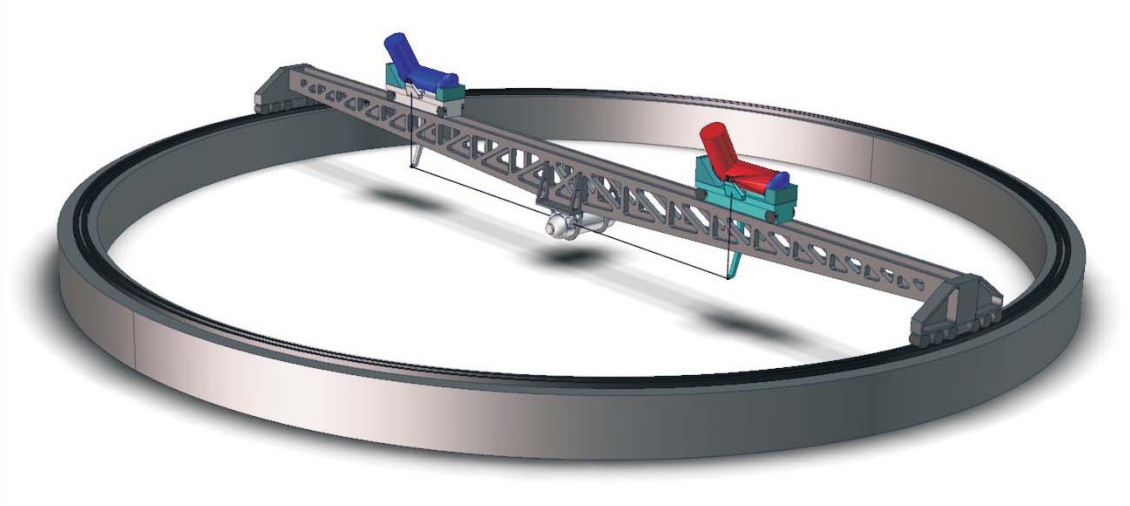

Figure 2.9: Overview of the ALADDIN infrastructure. A 40-m rotating truss bearing the siderostats is mounted on a 30-m high structure (not represented). The light beams collected by the two siderostats are fed into off-axis telescopes and routed towards the nulling instrument cryostat by fixed relay optics (only five reflections outside the cryostat).

specific to the nulling interferometry technique, namely photometry and amplitude control, polarization matching, phase shifting, beam combination and internal modulation, spatial filtering, spectrometry, detection, electronics and cryogenics.

Considering the Darwin/TPF targets, GENIE/UT could detect exozodiacal discs about 50 times as dense as the solar zodiacal cloud (Absil *et al.* 2006a). Due to shorter available baselines, GENIE/AT would also be valuable to observe the closest stars for which GENIE/UT is strongly limited by the geometric leakage (see Equation 2.15). Further information on the capabilities of GENIE is given in Chapter 3, reporting the comparison of performance with other nulling instruments such as ALADDIN described hereafter.

2.5.2 ALADDIN

ALADDIN (Antarctic L-band Astrophysics Discovery Demonstrator for Interferometric Nulling, Coudé du Foresto *et al.* 2006) is a Bracewell interferometer with two 1-m collectors, foreseen to be installed at Dome C (Antarctica). The two moveable siderostats are located on a 40-m long rotating truss installed on top of a 30 m tower and are able to move on a circular path to maintain the source at the meridian of the baseline (see Figure 2.9). In that manner, the baseline is always perpendicular to the line of sight so that neither long delay lines nor dispersion correctors are needed. This design has also the advantage to benefit for the exceptionally low turbulence of the free air above the boundary layer. The whole nulling instrument is assumed to be enclosed in a cryostat, in order to improve its overall stability and to mitigate the influence of temperature variations between seasons at the ground level (the mean temperature during the austral summer is about 40° C higher than during winter, while the instrument should be usable during the whole year). The lower temperature of the optics inside the cryostat (77 K) also further decreases the background emission produced by the instrument. The available baseline lengths range from 4 to 30 m and provide a maximum angular resolution of 10 mas in the L band (ranging from 2.8 to 4.2 μm).

The L band has been chosen in relationship with the main scientific goal of ALADDIN which is to investigate the inner region of exozodiacal discs. The 10-mas maximum angular resolution provided by this wavelength range is largely sufficient to study the HZs around Darwin/TPF-I candidate targets, since they are typically separated by a few 10 mas from their parent star (Kaltenegger *et al.* 2007a). ALADDIN

presents an improved sensitivity with respect to GENIE and should be able to detect exozodiacal discs at the level of 20 zodis. The capabilities of ALADDIN has been recently studied in details and compared to those of GENIE (Absil *et al.* 2007) and Pegase (Defrère *et al.* 2007a, see Chapter 3 for more details).

3

Pegase: a space-based precursor to Darwin

Contents

Abstract. Pegase is a single Bracewell interferometer proposed in the framework of the 2004 call for scientific proposals from Centre National d'Etudes Spatiales (CNES) for its formation flying demonstrator mission. The main scientific goal of Pegase would be to enable the high-angular resolution study of EGPs in the near-infrared (from 1.5 to 6 μm). In addition, Pegase might serve as a technology demonstrator for future major space missions based on formation flying. Proposed in 2004 by a consortium of European laboratories lead by Institut d'Astrophysique Spatiale (IAS), Pegase was selected along with three other concepts for a phase-0 study performed at CNES during 2005. The results of this study showed that the mission could be feasible following an 8-9 year development period, using existing or slightly improved space components. However, the mission was not selected for budgetary reasons and has been consequently submitted to the ESA Cosmic Vision programme in 2007. This chapter presents the simulated performance of Pegase for planet and circumstellar disc detection which has directly contributed to the Cosmic Vision proposal. The capabilities of an upgraded version of Pegase (namely Pegasus) have also been thoroughly investigated.

3.1 Scientific objectives of Pegase

With its high dynamic range, Pegase is a particularly well suited instrument to observe a faint target in the proximity of a bright source. In particular, Pegase promises significant scientific breakthroughs in the extrasolar planetary field by probing EGP's atmospheres and circumstellar discs. The survey of brown dwarfs and active galactic nuclei (AGN) is also expected to be very fruitful. These objectives are reviewed briefly hereafter.

3.1.1 Circumstellar disc science

Protoplanetary discs

As discussed in chapter 1, planets form in a protoplanetary disc well before the parent star reaches the main sequence. The probable migrations of the extrasolar planets from their birth places, probably external to the snow line to the inner regions, produce wide gaps in the circumstellar discs. Hence, looking for gaps created by transiting planets inside the disc is very important to understand the formation of planetary systems and early dynamics of planets, including migration and orbital interactions. The gaps create a non-uniformity in the disc which can be detected by high accuracy visibility measurements. Among all types of stars and discs, gaps can particularly be observed in the case of FU Ori discs[5] (see Figure 3.1). The gap is detected by an accurate measurement of the visibility function. Preliminary simulations have shown that a 0.05 AU gap would lead to variations of the visibility of a few percents (Herwats, in prep.). In particular, around Herbig AE/BE stars[6], the transition between the photospheric emission of the star and the disc emission can be observed. This observation of the internal part disc where the dust grains sublimate (0.1 to 0.4 AU) is relevant to constrain models. Around T Tauri stars[7], it is possible to constrain the size of the magnetosphere of the star and to observe the inner part of the disc, allowing the study of matter transfer from internal disk to stellar surface.

Debris discs

The next step in understanding planetary formation is the study of debris discs. Infrared interferometry is a very appropriate tool as it can provide sub-AU spatial resolution and spatially separate the contribution of the warm dust from that of the stellar photosphere. Indeed, near IR (K-band) thermal emission at the $\sim$ 1% photospheric level has already been isolated in the vicinity of Vega and tau Ceti with the CHARA/FLUOR ground-based interferometer (Absil *et al.* 2006a; di Folco *et al.* 2007). PEGASE, providing detectability for higher contrast environments (up to 10000:1) and at longer wavelengths, will be able to probe a much wider range of inner debris discs. Beyond the mere photometry of warm dust, an interferometer can provide very useful information about its spatial distribution. Most of the near-IR flux is expected to be emitted by a thin ring region whose radius corresponds to the sublimation limit of the dust. Measuring the sublimation radius strongly constrains the mineralogy of the grains. This, however, requires the capability to address arbitrarily any point in the (u,v) plane, a feature that distinguishes Pegase from ground-based interferometers. In addition, the presence of planets in a circumstellar disc creates structures (not only gaps but also large scale structures) that can be detected with a high angular resolution, high dynamics instrument. Such observations of debris discs should provide useful information on the existence and major parameters of planets (e.g. mass, orbit, current location) as well as the location of planetesimals belts, comparable to the Kuiper belt.

[5] In stellar evolution, FU Ori objects are pre-main sequence stars which display an extreme change in magnitude and spectral type.

[6] Herbig Ae/Be stars are pre-main sequence stars (younger than 10 Myr) stars of spectral types A and B, still embedded in gas-dust envelopes and surrounded by a circumstellar disc.

[7] T Tauri stars are a class of variable stars named after their prototype, T Tauri. They are found near molecular clouds and identified by their optical variability and strong chromospheric lines.

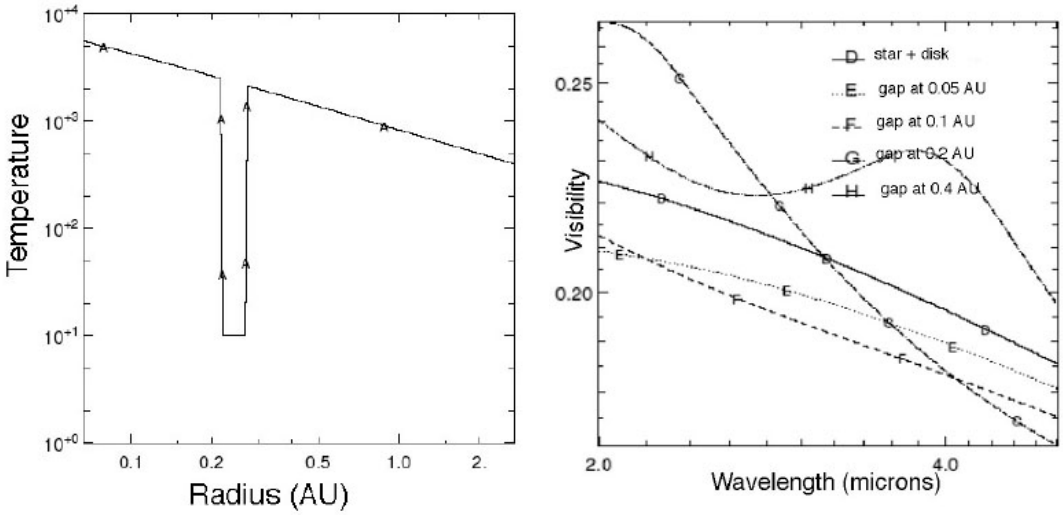

Figure 3.1: Variation of the measured fringe visibility as a function of the gap in a FU Ori disk. The gap is modelled by a break in the temperature distribution. The baseline is equal to 500 m (Herwats, in prep.).

Exozodiacal light characterization in the context of DARWIN

The study of the amount and distribution of exozodiacal light around main sequence stars has a particular relevance in the context of the DARWIN/TPF projects. The emission of dust particles within the HZ around the target stars is a key parameter for the performance of a nulling interferometer, as it is likely to be the brightest component (after the star itself) of an extrasolar system. For example in the solar system, the zodiacal light is two orders of magnitude brighter than the Earth at mid-infrared wavelengths. Warm exozodiacal cloud could thus become a dominant source of noise and hamper the detection of faint planets. Irregularities in the dust cloud (such as clumps) may also be confused with a planet. PEGASE will have the capability of providing a statistically significant survey of the amount of exozodiacal dust in the HZ around the DARWIN targets, and its prevalence as a function of other stellar characteristics (e.g. age, spectral type, metallicity, cold debris disc). It will be used to streamline the input source catalogue for the Darwin survey (reducing the risk of observing sources for which exozodiacal light prevents Earth-like planet detection) and optimize its mission profile before the launch. The capabilities of Pegase in that respect are investigated in section 3.3.

3.1.2 Sub-stellar objects

Extrasolar planets

The most compelling scientific goal of Pegase, which is also the main design driver, is to perform the spectroscopic characterisation of extrasolar planets. The target list is mainly composed of EGPs orbiting close to their parent star (0.017 to 0.1 AU, i.e. orbital periods shorter than 10 days). About 50 hot EGPs have been detected so far in our neighborhood ($<$ 150 pc), generally by means of radial velocity surveys. Present observation techniques help characterizing the mass of the objects, and elements of the atmospheric composition by spectral photometry and model fitting, but up to now, no spectrum with a resolution of several tens has been obtained (see section 1.1.3 for more details). Such a spectrum would help determining the atmospheric and internal structure of the object. The understanding of the internal structure is fundamental to explain the object diversity that is observed. Indeed, two objects with the same diameter can have a mass varying by a factor 2.

There is a particular interest in studying the physics of hot EGPs because they have no equivalent

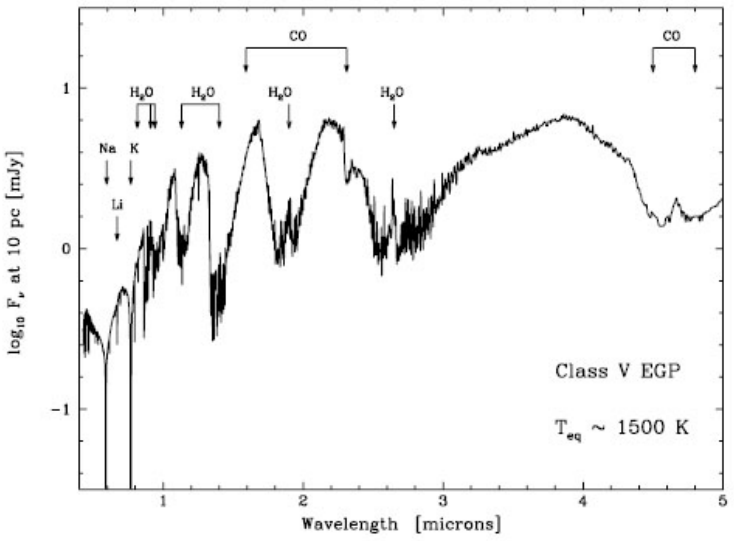

Figure 3.2: Example of synthetic spectrum for a hot jupiters located at 0.1 AU from its parent star and heated up to 1000 K (applicable to *51 Peg*, Sudarsky *et al.* 2003). For a sake of comparison, a Sun located at the distance of *51 Peg* would have a flux of about 8 Jy at 3 μm.

in the solar system and because no theory had predicted their existence before their discovery. These hot and highly irradiated objects ($T_{eff} < 1000$ to 1500 K) are nowadays thought to have formed far from their central star, and to have migrated inward, where they now have their rotation synchronously locked with their revolution period. This means that a same face of the planet is permanently irradiated leading to a complex circulation within the atmosphere. Even if all the models describe hot jupiters as giant gaseous objects, the role of aerosols and potential clouds of dust, the level of thermalization between irradiated and dark hemispheres of the planet and the potential existence of winds between the hemispheres are strongly discussed.

The infrared spectroscopy in the near infrared (from 1.5 to 6 μm) has several advantages to study hot EGPs. The contrast with the central star is moderate (10^5 to 10^3, depending on the wavelength). This spectral range contains molecular species such as CH_4, CO (which depth is a tracer of cloud thickness) and especially H_2O at 2.6 μm, difficult to detect from ground. Figures 3.2 and 3.3 show 3 alternative models with and without clouds leading to a strong difference in the spectral features depth. Collision-induced absorption by H_2 can also potentially be detected between 2.5 and 3.0 μm. Moreover, this wavelength regime gives access to an almost unperturbed part of the continuum in the thermal emission, between roughly 3.5 and 4.3 μm, which allows for a good estimation of the planet equilibrium temperature. A spectral analysis of the objects with a spectral resolution of several tens in the near infrared would strongly constrain the atmospheric models.

Brown dwarfs

With moderate baseline lengths, Pegase could also be used to characterise the atmospheres of bounded brown dwarf stars by using the nulling mode. Spectroscopic studies of brown dwarfs provide constraints on their surface temperature, radius and the composition of their atmosphere (especially for CH_4 and for the clouds). In addition, observing bounded brown dwarfs has the advantage of giving an accurate estimation of the mass of the companion (thanks to the observation of the companion trajectory and their likely adherence to Kepler's laws) and its age (thanks to the spectroscopic study of the parent star), compared to free floating objects where these parameters have to be estimated using theoretical models. Pegase would provide the required angular resolution and dynamic range to study bounded brown dwarfs (the contrast between a Sun-like star and a brown dwarf typically ranges between 10^3

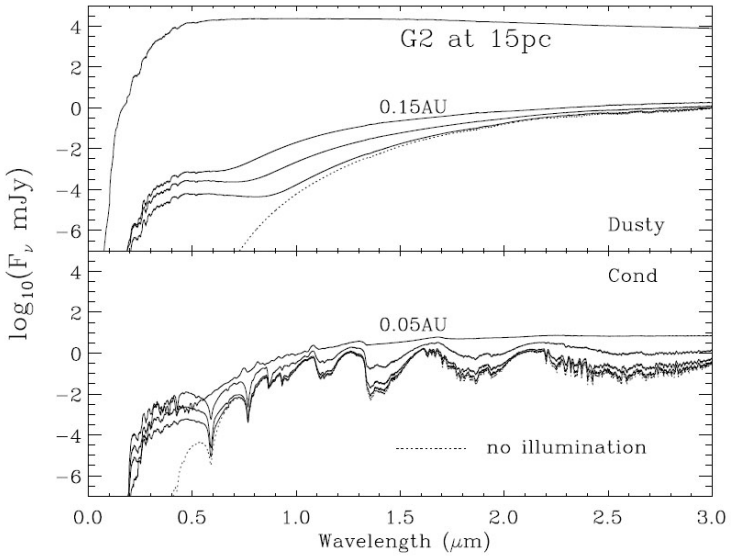

Figure 3.3: Example of synthetic spectra for hot EGPs for different atmospheric models (Barman *et al.* 2001). In the top figure, the dust is supposed to have entirely settled, leaving "clear skies". In the bottom figure, settling is ignored so that the dust contributes to oppacity. The planets have been placed respectively at 0.15, 0.25 and 0.5 AU from the star in the top figure and at 0.05, 0.1 and 0.25 AU in the bottom figure.

and 10^5 for a 1 Gyr-old system). Furthermore, the study of brown dwarfs of various ages will help to constrain evolutionary models of these objects.

3.1.3 Additional programmes

The scientific programmes using the visibility mode have to take into account the instrumental characteristics of PEGASE and the main operational constraints. The targets of PEGASE are compact sources for which emission peaks in the 1.5-6 μm spectral range, corresponding to a temperature range from 500 to 3000 K (maximum of the black body emission). In that spectral range, PEGASE will get the sensitivity of ISO but with an angular resolution 80 to 1000 times higher (about 0.5 mas), thanks to baseline from 40 to 500 m. As a two telescopes interferometer, PEGASE will not be able to spend a lot of time on imaging spatially complex sources. The astrophysical targets have to be easily characterized by simple models, symmetrical (uniform or Gaussian) or not (binaries). The great advantage of PEGASE with respect to other interferometers will be its ability to observe continuously with a stable configuration during a time exceeding the classical 24 hour cycle. The other advantage is the length of the baselines that can exceed a few hundreds meter. The following programs take advantages of this situation to propose unique science that can be done with PEGASE in the future:

- Active galactic nuclei (AGN);
- Resolving images of quasars splitted by gravitational lens effects;
- Temporal characterization of different classes of rapid radial pulsators;
- Disc formation and evolution of active hot stars.

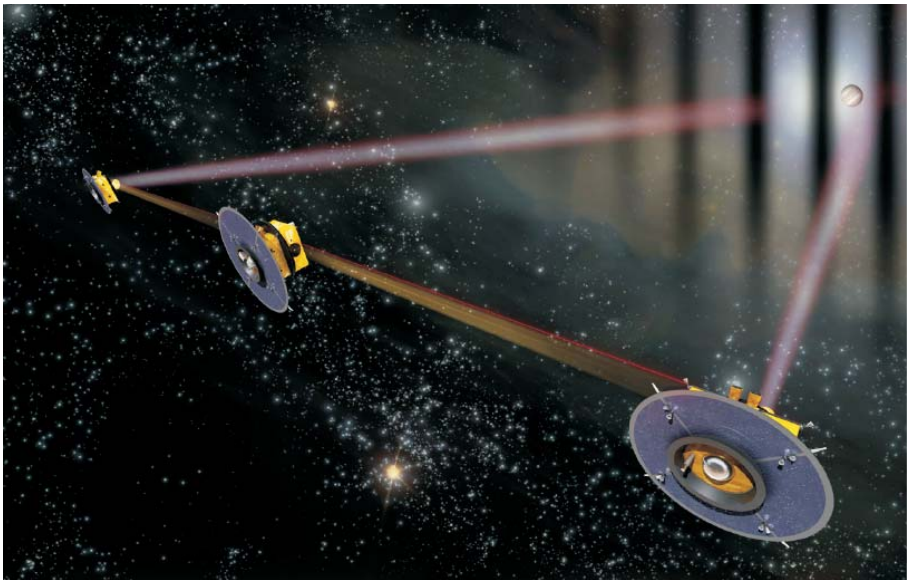

Figure 3.4: Overview of the Pegase space-based interferometer. The two siderostats are flying in linear configuration with the beam combiner spacecraft located in the middle of the formation.

3.2 Instrumental concept

Following the phase 0 study, the optimum instrumental parameters of Pegase has been determined. The baseline concept for the mission consists in a two-telescope interferometer formed of three free flying spacecraft orbiting around the second Lagrangian point, L2, and pointing in the anti-solar direction within $\pm$ 30° cone. Thanks to this location, the spacecraft and the focal plane assembly can be passively cooled down to respectively 90 $\pm$ 0.1 K and 55 $\pm$ 0.1 K. In its nominal configuration, Pegase consists in two 40-cm siderostats and a beam combiner flying in linear formation (see Figure 3.4). Visibility measurements and recombination in nulling mode (Bracewell interferometer) are both possible with a spectral resolution of about 60. The formation flying constraints allow baseline lengths from 40 to 500 m giving an angular resolution in the range of 0.5-30 mas. The fine-tuning of the optical path difference (OPD) is performed by a dedicated control loop based on a fringe sensor measuring the observed central target in the 0.8-1.5 μm range and an optical delay line. The intensity control is performed by a fine pointing loop using a field relative angle sensor operating in the 0.6-0.8 μm range and fast steering mirrors based on piezoelectric devices. This implementation allows to control the OPD down to a level of 2.5 nm rms and the tip/tilt errors to a value of 30 mas rms, corresponding to a nulling ratio of 10^{-4} stable at the level of 10^{-5}. The instrumental parameters of Pegase are summarized in Table 3.1.

Instrumental parameters	
Baselines	40-500 m
Telescope diameter	0.40 m
Warm throughput	0.46
Cold throughput	0.80
Optics temperature	90 $\pm$ 0.1 K
Detector temperature	55 $\pm$ 0.1 K
IR total transmission	7 %
Science waveband	1.5-6 μm
Fringe sensing waveband	0.8-1.5 μm
Tip-tilt sensing waveband	0.6-0.8 μm

Table 3.1: Instrumental parameters of Pegase resulting from the phase 0 study.

The optical arrangement is represented in Figure 3.5 with the following elements on the optical path:

- Two afocal telescopes, composed of two mirrors (see M_2 and M_3), with an optical magnification which will be a trade-off between dynamics of the tip-tilt errors, the available stroke of the fast steering mirrors, the actuation noise, the mechanical constraints and the polarization limitations. A magnification of the order of 20 is today considered as a good starting value.
- Two fast steering mirrors to correct the tip-tilt errors. They are placed the closest to the afocal telescopes in order to minimize the optical space where the tip-tilt errors are not corrected, and hence reduce differential polarization effects (possible location are M_3 or M_4).
- Two achromatic π-phase shifters using field reversal by reflections (Serabyn 1999, see for instance M_4 and M_1).
- Two optical delay lines placed after the active mirrors to operate in a tip/tilt corrected optical space.
- Dichroic beam splitters which separate the signal between the science wave band and the tip-til/OPD sensing wave bands.
- A Modified Mach Zehnder (MMZ) to achieve the combination. Another MMZ might be necessary to cover the full wavelength range, depending on the the coating feasibility.
- Small off axis parabolas focus the four outputs of the MMZ into single mode fibres. A fluoride glass fibre can cover the spectral range 1.5-3 μm. A chalcogenide fibre is required for the spectral range 3-6 μm.

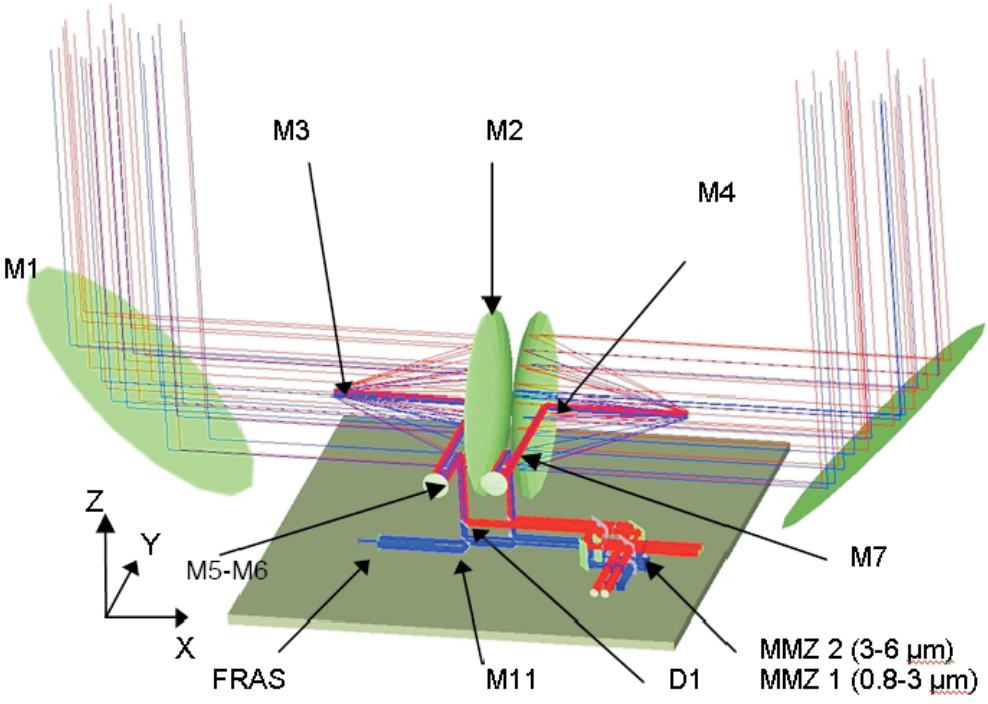

Figure 3.5: Optical layout of the Pegase nulling interferometer (adapted from Le Duigou *et al.* 2006).

3.3 Performance for exozodiacal disc detection

In order to assess the performance of Pegase for exozodiacal disc detection, the GENIEsim software[8] (Absil *et al.* 2006b) has been adapted to enable the simulation of a space-based nulling interferometer. In particular, the expected vibrations of the telescopes along the optical path in the ambient space environment have been implemented and all atmospheric effects disabled. The space environment is now fully integrated in GENIEsim and space-based nulling interferometers can be simulated by switching the appropriate keywords. After briefly describing the GENIEsim software, the modifications necessary to simulate space-based instruments are discussed in the section 3.3.2.

3.3.1 The GENIEsim software

GENIEsim is an IDL-written code which has originally been designed to simulate the GENIE instrument at the VLTI interferometer. It has the advantage to benefit from extensive validation efforts by cross-checking with performance estimates carried out by industrial partners during the GENIE phase A study. GENIEsim performs end-to-end simulations of ground-based nulling interferometers which include the simulation of astronomical sources (star, circumstellar disc, planets and background emission), atmospheric turbulence (piston, longitudinal dispersion, wavefront errors and scintillation), as well as a realistic implementation of closed-loop compensation of atmospheric effects by means of fringe tracking and wavefront correction systems.

On input of GENIEsim, two text files are required to define the instrument and the science target. These two files contain 170 global parameters which can be classified as:

- The operational parameters, detailing the configuration, the control loops, the atmosphere and the VLTI environment;
- The observational parameters, specifying the target system and relevant observational parameters.

In addition to these two input files, GENIEsim is controlled by a set of keyword switches, by which GENIEsim is told what are the names of the output files, what atmospheric effects and control loops to take into account in the computation. In the last release of GENIEsim, the simulation of a nulling instrument at Cerro Paranal (Chile), Dome C (Antarctica) or located in space can be performed. ALADDIN and PEGASE keywords are available for a direct simulation of these instruments.

Based on these inputs, GENIEsim produces an instantaneous transmission map of the nulling interferometer (see Equation 2.3), taking into account all perturbations related to the instrument and its environment. This map is projected on the plane of the sky in order to compute the transmitted flux from all astrophysical sources located within the field-of-view of the instrument. Each individual source is affected by the transmission map differently:

- The residual stellar emission at the destructive output of the instrument is computed in a semi-analytical way by 2D numerical integration. This process gives a very accurate stellar leakage estimate.
- The contribution of the exozodiacal disc is computed by multiplying a disc image, sampled over the field-of-view by a $n \times n$ pixel grid, by a digitised transmission map of the same size. The disc image can be computed with three different packages, depending on the target (optically thin disc, optically thick or the solar zodiacal disc seen from outside the solar system). The size of the image is generally 128 $\times$ 128 pixels but special attention has to payed for configurations for which the

[8] GENIEsim is available on request from Roland den Hartog (rdhartog@rssd.esa.int) or Olivier Absil (olivier.absil@obs.ujf-grenoble.fr).

"telescope diameter/baseline length" ratio is low. In this case, the field-of-view is relatively large and it can be necessary to increase the number of pixels in order to avoid undersampling problems, especially when the baseline length is long.

- Potential planets are considered as point-like sources, and are thus only affected by the value of the transmission map at the position of their centre.
- The background emission is assumed to be perfectly incoherent so that the resulting signal can be computed by a simple integration over the field-of-view.

Taking into account all the sources in the field-of-view, GENIEsim simulates an observational run by a number of Observation Blocks (OB), which have a duration of typically 10 to 100 seconds. For each OB, the simulator generates time sequences for the random variables, based on their input power spectral densities and on the transfer functions of the control loops. The initialisation of control loops is one of the first actions performed in the time loop on OBs. The coupling efficiency is also computed in real-time as it is affected by random perturbations as well. Finally, the output of the simulator basically consists in time series of photo-electrons recorded by the detector at the two outputs of the nulling combiner (constructive and destructive outputs) as a function of time and wavelength. The overall architecture of the GENIEsim software is represented in Figure 3.6.

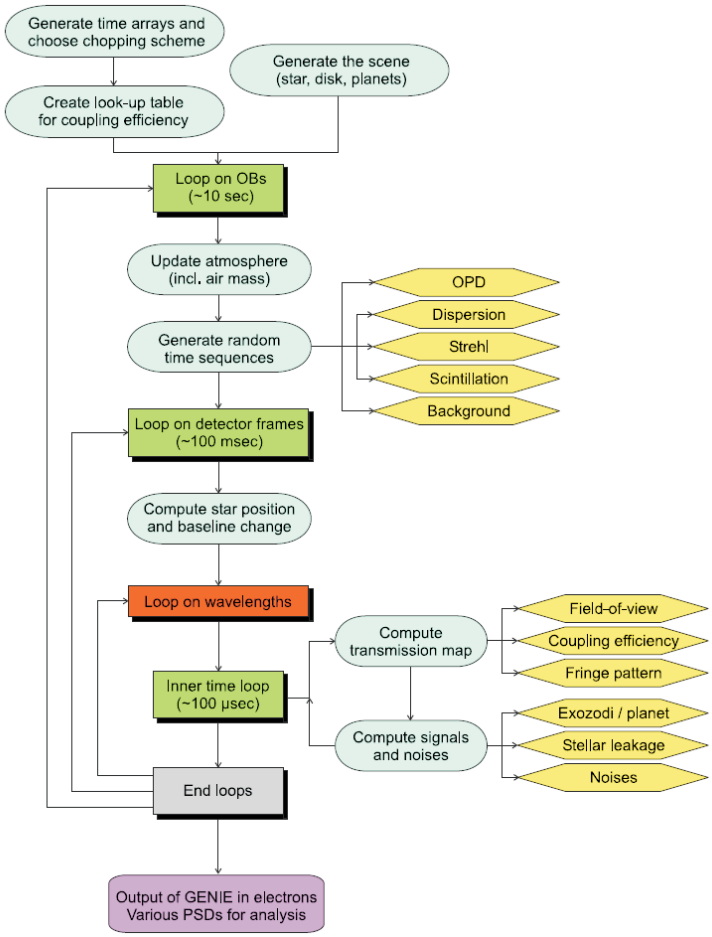

Figure 3.6: Block diagram showing the top-level architecture of the GENIEsim software (Figure from Absil 2006).

3.3.2 Vibrations in the ambient space environment

To enable the simulation of a space-based nulling interferometer, few modifications were necessary due to the versatility of GENIEsim. Disabling all atmospheric effects and the VLTI environment is easily achieved by setting the appropriate keywords. The main modification was to introduce the random sequences of OPD and tip/tilt generated by the vibrations of the telescopes in the ambient space environment.

The vibrations of the spacecraft are a critical issue for nulling interferometry because they induce mismatches in the optical paths and pointing errors which give rise to instability noise (Lay 2004). These vibrations are caused by disturbance forces which can be either internal (due to on-board systems) or external (caused by the ambient space environment). For Pegase, the internal disturbance forces arise mainly from the thrusters, the Optical Delay Line (ODL), the steering mirrors, and the reaction wheels. The requirements on these on-board systems have been assessed recently by two R&D studies (Villien *et al.* 2007). The external disturbance forces are mainly caused by particulate impacts, solar radiation pressure and charging effects but these effects are not expected to be dominant at the L2 point. A recent comparative study concludes that the ambient space environment causes no larger OPD than the disturbances induced by on-board equipments for Darwin and its precursor missions (Sterken 2005). The total disturbance force can be related to the induced vibrations by the basic equation of the rigid body motion:

$$S_{\text{vib}} = \frac{1}{16\pi^4 m^2 f^4} S_{\text{in}} \,, \tag{3.1}$$

where m is the mass of the spacecraft, f the frequency, S_{in} the Power Spectral Density (PSD) of the total disturbance force in N^2/Hz and S_{vib} the PSD of the spacecraft displacement in m^2/Hz. Assessing the shape and magnitude of the input disturbance PSD requires a specific R&D study and is beyond the scope of this master thesis. Following the results about the Darwin mission (Sterken *et al.* 2005), we will assume that the global disturbance force is distributed as white noise, so that the PSD of the spacecraft displacement (S_{out}) decays linearly with a slope of -40 dB/dec. The relative displacement induced by internal disturbances (rms_{vib}) should not exceed 1 μm rms as indicated by the phase 0 study performed by CNES in 2005. Based on this value, the PSD of the spacecraft tip-tilt before correction (rms_{tt}) can be computed as:

$$\text{rms}_{\text{tt}} = \frac{M}{R} \text{rms}_{\text{vib}} \,, \tag{3.2}$$

where M is the magnification factor (20 according to the phase 0 study) and R the telescope radius. This gives a rms tip-tilt error of about $35''$ ($\sim$ 2000 mas) rms. This value does not take into account an additional noise of 10 mas/$\sqrt{(Hz)}$ per tip-tilt mirror which has been considered separately in GENIEsim as an actuator noise. Finally, note that the frequencies at which resonances are present should cause additional peaks in the input vibrations (for instance, due to the sun-shields) but these frequencies have not been considered since they are not yet well defined. Their impact on the residual OPD could however be minimised by the use of an appropriate Butterworth filter.

3.3.3 Real-time correction of spacecraft vibrations

As indicated in the previous section, the level of OPD would be of the order of 1 μm rms without an appropriate control loop. This is very constraining for exozodiacal disc detection and fringe tracker is

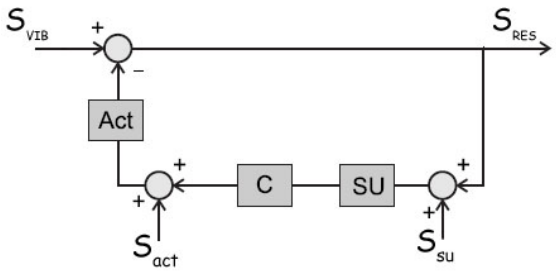

Figure 3.7: Simplified block-diagram of a fringe tracking system (adapted from Absil 2006).

by consequent mandatory to stabilize the OPD to a sufficiently low value. In GENIEsim, the simulation of the control loop is achieved by a simultaneous optimisation of the repetition frequency and of the controller parameters (a simple PID[9]). The procedure is based on a description of spacecraft vibrations in terms of its temporal PSD, while the action of control loops is expressed by means of transfer functions in the frequency domain. The general architecture of real-time control loops is illustrated in Figure 3.7. The three main components of the loop are the sensing unit (SU), which provides an estimation of the perturbations to be corrected for (e.g. OPD difference for a fringe tracking loop), the controller (C), which computes the correction applied to cancel the perturbation, and the actuator (Act), which performs the correction (e.g. an optical delay line). Both sensor and actuator produce additional noise in the control process, modelled by their PSDs (S_{su} and S_{act}), which is applied at the input of the associated block. Sensor noise (S_{su}) depends on the number of available photons in each elementary measurement (shot noise and detector noise), while actuator noise (S_{act}) depends on the particular design of the actuator. The input and residual vibrations are described by their PSDs (S_{vib} and S_{res}).

3.3.4 Article: *Performance study of space-based infrared Bracewell interferometers: comparison with ground-based sites for exozodiacal dust disc detection*

The following article (Defrère *et al.* 2007a) presents a thorough comparison of performance between Pegase and ground-based demonstrators for exozodiacal disc detection. Particularly, the nulling performance of Pegase is addressed and discussed. The end-to-end simulation of Pegase finally provides realistic estimates of its sensitivity in terms of detectable exozodiacal level, taking into account calibration (when necessary) and data postprocessing techniques.

[9]PID stands for “Proportional, Integral and Differential" which is a basic controller device for closed-loop control

Astronomy & Astrophysics manuscript no. Disc˙Pegase
September 6, 2007

Performance study of space-based infrared Bracewell interferometers

Comparison with ground-based sites for exozodiacal disc detection

D. Defrère[1], O. Absil[2], and V. Coudé du Foresto[3]

[1] Institut d'Astrophysique et de Géophysique de Liège, Université de Liège, 17 Allée du 6 Août, B-4000 Liège, Belgium
e-mail: defrere@astro.ulg.ac.be
[2] LAOG, Université Joseph Fourier, CNRS, 414 rue de la Piscine, F-38400 Grenoble, France
[3] LESIA, Observatoire de Paris-Meudon, CNRS, 5 place Jules Janssen, F-92195 Meudon, France

Received; accepted

ABSTRACT

Context. Characterising the circumstellar dust around nearby main sequence stars is a necessary step to understand the planetary formation process and of crucial relevance for the future life-finding space missions such as ESA's Darwin or NASA's Terrestrial Planet Finder (TPF). In addition to paving the technological way for Darwin/TPF, the space-based infrared interferometer Pegase will be a valuable scientific precursor in that respect.
Aims. Investigating the performance of Pegase for the exozodiacal disc detection and compare the results with ground-based demonstrators.
Methods. The GENIEsim software (Absil et al. 2006) used for the GENIE (VLTI nuller, using two 8-m telescopes) and ALADDIN (Antarctic nuller, using two dedicated 1-m telescopes) studies, has been adapted to simulate the performance of a space-based nulling interferometer. In particular, all atmospheric effects have been disabled and the vibrational level due to the ambient space environment implemented.
Results. Despite relatively small telescopes (40 cm diameter), Pegase shows very good capabilities for the exozodiacal dust detection. Comparing to the results of GENIEsim applied on ground-based nulling interferometers, Pegase exceeds the sensitivity of GENIE in all cases and shows similar performance to ALADDIN for the most distant targets. The sensitivity could be boosted by considering a triangular flight configuration to outperform any ground-based nuller for the most distant stars of the Darwin/TPF catalogue.
Conclusions. In addition to its main objective (characterising hot giant extrasolar planets), the space-based nulling interferometer Pegase will also be a very efficient instrument to assess the level of circumstellar dust around nearby main sequence stars.

Key words. Space-based interferometer – Instrumentation: high angular resolution – Technique: nulling interferometry – Circumstellar discs

1. Introduction

Nulling interferometry is the core technique of future life-finding space missions such as ESA's Darwin (Fridlund et al. 2006) and NASA's Terrestrial Planet Finder (TPF, Beichman et al. 2006). Observing in the infrared (6-20 μm), these missions would enable the spectroscopic characterisation of the atmosphere of habitable extrasolar planets orbiting nearby main sequence stars. This ability to study distant planets strongly depends on the density of exozodiacal clouds around the stars which can hamper the planet detection if the warm exozodiacal dust is more than 20 times as dense as our solar zodiacal disc (Absil 2001). Assessing the level of circumstellar dust around nearby main sequence stars is by consequent a necessary pre-requisite to prepare the observing programme of Darwin/TPF by reducing the risk of observing sources for which exozodiacal light prevents Earth-like planet detection. The objective is to provide a statistically significant survey of the amount of exozodiacal light in the habitable zone around the DARWIN/TPF targets, and its prevalence as a function of other stellar characteristics (age, spectral type, metallicity, cold debris disc...).

In addition, circumstellar discs are intrinsically linked to the existence of planets and detecting them provides an efficient way to study the formation and evolution of planetary systems. At young ages, most stars are surrounded by protoplanetary discs in which the planetary systems are believed to form (Meyer et al. 2007). In particular, the detection of gaps in these protoplanetary discs is very important to understand the early dynamics of planets, including migration and orbital interaction. At older ages, photometric surveys with mainly IRAS, ISO and SPITZER have revealed the presence of micron-sized grains around dozens of main sequence stars. This is interpreted as the sign of planetary activity, as the production of grains is believed (by analogy with the zodiacal cloud in our solar system) to be sustained by asteroid collisions and outgassing of comets in the first tens of astronomical unit (AU). To improve our understanding of planetary systems, it is necessary to get a global view of the discs, at different scales and distances from the stars. However, to probe the innermost regions of the discs, photometry is generally not sufficient and interferometry is required to separate the starlight from the disc emission. A good example is given by the recent detection of warm dust around Vega with classical interferometry at the CHARA array (Absil et al. 2006b). Several scientific observations using nulling interferometry have also been been carried

Send offprint requests to: D. Defrère

Fig. 1. Overview of the Pegase space-based interferometer. The two siderostats are flying in linear configuration with the beam combiner spacecraft located in the middle of the formation.

out with the Bracewell Infrared Nulling Cryostat (BLINC, Hinz et al. 2000) instrument at the Multi-Mirror Telescope (MMT, Mont Hopkins, Arizona), with the Keck interferometer (Hawaii, Serabyn et al. 2006) and foreseen to begin in 2009 at the Large Binocular Telescope (Mount Graham, Arizona,Wagner 2006). In Europe, ESA has initiated the ground-based Darwin demonstrator, i.e. GENIE (Ground-based European Nulling Interferometer Experiment, Gondoin et al. 2004). GENIE is a nulling interferometer conceived as a focal instrument for the VLTI which has been studied by ESA at the phase A level. The second instrument is ALADDIN (Antarctic L-band Astrophysics Discovery Demonstrator for Interferometric Nulling, Coudé du Foresto et al. 2006), a nulling interferometer project for Dome C, on the high Antarctic plateau. The performance of GENIE has been studied in details (Absil et al. 2006a,Wallner et al. 2006) and compare recently to ALADDIN (Absil et al. 2007). Using 1-m collectors, ALADDIN would have an improved sensitivity with respect to GENIE working on 8-m telescopes, provided that it is placed above the turbulence boundary layer (about 30 m at Dome C). ALADDIN would enable the detection of circumstellar discs 20 times as dense as our local zodiacal cloud for typical Darwin/TPF targets in an integration time of few hours.

The low atmospheric turbulence on the high Antarctic plateau is a significant advantage with respect to other astronomical sites and one of the main reasons of the ALADDIN very good sensitivity. However, as any other ground-based sites, the thermal background and its variation are still major limitations to the performance and active compensation by real-time control systems are mandatory. Observing from space would provide an efficient solution to improve the sensitivity by getting rid of the harmful effect of the atmosphere. The detection of circumstellar dust discs from space could be achieved by the infrared nulling interferometer Pegase (Le Duigou et al. 2006) which was recently submitted to the ESA Cosmic Vision programme. With its two 40-cm diameter telescopes, Pegase has been initially designed to study the extrasolar giant planets at high-angular resolution at near infrared wavelengths (1.5-6 μm). In addition, it could be also a particularly well suited instrument for the detection of circumstellar dust in the first AUs of extrasolar planetary systems. By classical photometry, the presence of this hot dust cannot be unequivocally determined because the typical accuracy is a few percents at best in rather large fields of view. After the detailed studies of ground-based instruments ideally located as GENIE at Cerro Paranal (Absil et al. 2006a, hereafter Paper I) or ALADDIN on the Antarctic plateau (Absil et al. 2007, hereafter Paper II), the study reported in this paper addresses the performance of a space-based nulling instrument for the exozodiacal disc detection.

2. The Pegase space-based interferometer

Pegase is a single Bracewell interferometer that was initially proposed in the framework of the 2004 call by the French space agency (CNES) for its formation flying demonstrator mission. CNES performed a Phase 0 study in 2005 and concluded that the mission is feasible within an 8 to 9 years development plan (Le Duigou et al. 2006). However, the mission was not selected for budgetary reasons and has been consequently submitted to the ESA Cosmic Vision programme in 2007.

2.1. Scientific objectives

The main scientific goal of Pegase is to perform spectroscopy of hot extrasolar giant planets (EGP) and brown dwarfs. Most hot Jupiter-like planets ($M \geq 0.2\ M_{Jup}$) within 150 pc could be surveyed with a good signal-to-noise ratio (SNR) as well as several favorable hot Uranus-type planets ($0.04\ M_{Jup} \leq M \leq 0.2\ M_{Jup}$) with a final SNR ranging between 1 and 6 (Absil 2006). In particular, Pegase will be able to perform spectroscopy on 15% of the extrasolar planets known so far within 25 pc, including several planets outside the hot regime (further than 0.1 AU from the host star, Defrère et al. 2007). The detection of circumstellar discs is also in the core programme but the performance has not yet been carefully assessed. Pegase is expected to provide an accurate estimate of the dust size distribution from the very neighbourhood of the star to several AU from it. It will also help providing maps of the mineralogical composition, with a combination of spectral and spatial information on the discs. Combined with sub-mm observations from the ground providing the gas distribution with a comparable spatial resolution, it will then become possible to study the dust-gas interactions. Additional programmes on brown dwarfs and active galactic nuclei are also foreseen but it is the primary objective (the study of hot EGPs) which drives the design of Pegase.

2.2. Instrumental concept

Following the phase 0 study, the baseline configuration of Pegase have been fixed. Pegase is a two-aperture near-infrared (1.5-6 μm) interferometer formed of three free flying spacecraft planned to orbit at the Lagrange point L2. Thanks to this location, the spacecraft and the focal plane assembly can be passively cooled down to respectively 90 ± 0.1 K and 55 ± 0.1 K. In its nominal configuration, Pegase consists in two 40 cm siderostats and a beam combiner flying in linear formation. Visibility measurements and recombination in nulling mode (Bracewell interferometer) are both possible with a spectral resolution of about

Table 1. Specifications of Pegase resulting from the phase 0 study.

Instrumental parameters	
Baselines	40-500 m
Telescope diameter	0.40 m
Optics temperature	90 ± 0.1 K
Detector temperature	55 ± 0.1 K
IR total transmission	7 %
Science waveband	1.5-6 μm
Fringe sensing waveband	0.8-1.5 μm
Tip-tilt sensing waveband	0.6-0.8 μm

60. The formation flying constrains allow baseline lengths from 40 m to 500 m giving an angular resolution in the range of 0.5-30 mas. The fine-tuning of the optical path difference (OPD) is performed by a dedicated control loop based on a fringe sensor measuring the observed central target in the 0.8-1.5 μm range and an optical delay line. The intensity control is performed by a fine pointing loop using a field relative angle sensor operating in the 0.6-0.8 μm range and fast steering mirrors based on piezo-electric devices. This implementation allows to control the OPD down to a level of 2.5 nm rms and the tip/tilt errors to a value of 30 mas rms, corresponding to a nulling ratio of 10^{-4} stable at the level of 10^{-5}. The instrumental specifications of Pegase are summarized in Table 1. The optical arrangement is represented by the block diagram in Fig. 2 with the following elements on the optical path:

- Two afocal telescopes with an optical magnification which will be a trade-off between dynamics of the tip-tilt errors, the available stroke of the fast steering mirrors, the actuation noise, the mechanical constraints and the polarization limitations. A magnification of the order of 20 is today considered as a good starting value.
- Two fast steering mirrors to correct the tip-tilt errors. They are placed the closest to the afocal telescopes in order to minimize the optical space where the tip-tilt errors are not corrected, and hence reduce differential polarization effects.
- Two achromatic π-phase shifters using field reversal by reflections (Serabyn 1999).
- Two optical delay lines placed after the active mirrors to operate in a tip/tilt corrected optical space.
- Dichroic beam splitters which separate the signal between the science wave band and the tip-til/OPD sensing wave bands.
- A Modified Mach Zehnder (MMZ) to achieve the combination. Another MMZ might be necessary to cover the full wavelength range, depending on the the coating feasibility.
- Small off axis parabolas focus the four outputs of the MMZ into single mode fibres. A fluoride glass fibre can cover the spectral range 1.5-3 μm. A chalcogenide fibre is required for the spectral range 3-6 μm.

3. Nulling performance in space

In order to assess the performance of Pegase for exozodiacal disc detection, the GENIE simulation software (GENIEsim, see Paper I) has been used. GENIEsim has originally been designed to simulate the GENIE instrument at the VLTI interferometer and has the advantage to benefit from extensive validation efforts by cross-checking with performance estimations carried out by industrial partners during the GENIE phase A study. GENIEsim performs end-to-end simulations of ground-based

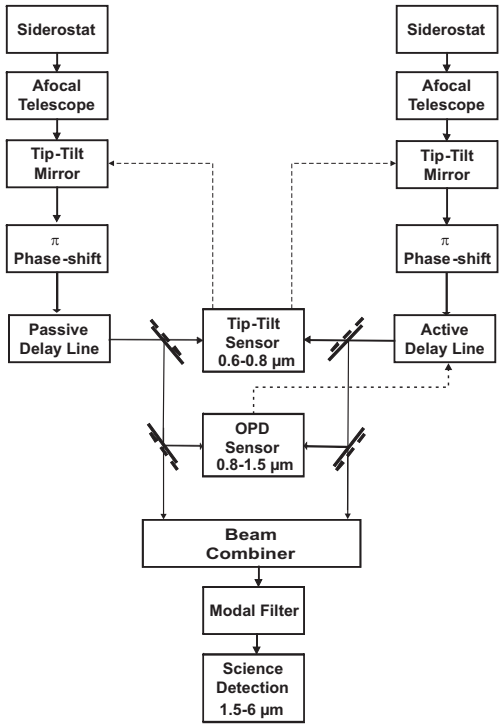

Fig. 2. Block diagram of the Pegase optical layout. Feed-back signals driving the tip-tilt/OPD control are shown in dashed lines.

nulling interferometers which includes the simulation of astronomical sources (star, circumstellar disc, planets, background emission), atmospheric turbulence (piston, longitudinal dispersion, wavefront errors, scintillation), as well as a realistic implementation of closed-loop compensation of atmospheric effects by means of fringe tracking and wavefront correction systems. The output of the simulator basically consists in time series of photo-electrons recorded by the detector at the two outputs of the nulling combiner (constructive and destructive outputs). To enable the simulation of a space-based nulling interferometer, few modifications were necessary due to the versatility of GENIEsim. Beside disabling all atmospheric effects, the main modification was to introduce the random sequences of OPD and tip/tilt generated by the vibrations of the telescopes in the ambient space environment. This is discussed in the following section.

3.1. Vibrations in space environment

The vibrations of the spacecraft are a critical issue for nulling interferometry because they induce mismatches in the optical paths and pointing errors which give rise to instability noise (Lay 2004). These vibrations are caused by disturbance forces which can be either internal (due to on-board systems) or external (caused by the ambient space environment). For Pegase, the internal disturbance forces arise mainly from the thrusters, the Optical Delay Line (ODL), the steering mirrors and the reaction wheels. The requirements on these on-board systems have been assessed recently by two R&D studies (Villien et al. 2007). The external disturbance forces are mainly caused by particulate impacts, solar radiation pressure and charging effects but these effects are not expected to be dominant at the L2 point. A recent comparative study concludes that the ambient space en-

Table 2. Control loop performance and optimum repetition frequencies for a 100 sec observation sequence. The observations are carried out for a G2V star located at 20 pc using either the 47-m UT2-UT3 baseline at the VLTI, a baseline length of 20 m for ALADDIN or a 40-m baseline length for Pegase. The total null is the mean nulling ratio including both the geometric and instrumental leakage contributions. The rms null is the standard deviation of the instrumental nulling ratio. The goal performance for exozodiacal disc detection discussed in Paper I appears in the last column.

	GENIE-UT	ALADDIN	Pegase	Goal
Piston	6.2 nm @ 13 kHz	10 nm @ 2 kHz	1.6 nm @ 100 Hz	< 4nm
Inter-band disp.	4.4 nm @ 300 Hz	7.0 nm @ 0 kHz	0 nm @ 0 kHz	< 4nm
Intra-band disp.	1.0 nm @ 300 Hz	7.4 nm @ 0 Hz	0 nm @ 0 kHz	< 4nm
Tip-tilt	11 mas @ 1 kHz	7 mas-1 kHz	26 mas @ 500 Hz	(see intensity)
Intensity mismatch	4% @ 1 kHz	1.2% @ 0 Hz	0.09% @ 0 kHz	< 1%
Total null	6.2×10^{-4}	2.2×10^{-4}	4.9×10^{-4}	f(baseline)
Instrumental null	1.5×10^{-4}	1.3×10^{-4}	8.8×10^{-5}	10^{-5}
Rms null	1.6×10^{-4}	1.2×10^{-4}	8.7×10^{-6}	10^{-5}

vironment causes no larger OPD than the disturbances induced by on-board equipments for Darwin and its precursor missions (Sterken 2005). The total disturbance force can be related to the induced vibrations by the basic equation of the rigid body motion:

$$S_{\rm vib} = \frac{1}{16\pi^4 m^2 f^4} S_{\rm in}\,, \tag{1}$$

where m is the mass of the spacecraft, f the frequency, $S_{\rm in}$ the Power Spectral Density (PSD) of the total disturbance force in N^2/Hz and $S_{\rm vib}$ the PSD of the spacecraft displacement in m^2/Hz. Assessing the shape and magnitude of the input disturbance PSD requires a specific R&D study and is beyond the scope of this paper. Following the results of Sterken about the Darwin mission (Sterken et al. 2005), we will assume that the global disturbance force is distributed as white noise, so that the PSD of the spacecraft displacement ($S_{\rm out}$) decays linearly with a slope of -40 dB/dec (see vib$_{in}$ curve in Fig. 3). The relative displacement induced by internal disturbances (rms$_{\rm vib}$) should not exceed 1 μm rms as indicated by the phase 0 study performed by CNES in 2005. Based on this value, the PSD of the spacecraft tip-tilt before correction (rms$_{\rm tt}$) can be computed as:

$$\mathrm{rms}_{\rm tt} = \frac{M}{R}\mathrm{rms}_{\rm vib}\,, \tag{2}$$

where M is the magnification factor (20 according to the phase 0 study) and R the telescope radius. This gives a rms tip-tilt error of about 35″ ($\sim$ 2000 mas) rms. This value does not take into account an additional noise of 10 mas/$\sqrt{(Hz)}$ per tip-tilt mirror which has been considered separately in GENIEsim as an actuator noise. Finally, note that the frequencies at which resonances are present should cause additional peaks in the input vibrations (for instance, due to the sun-shields) but these frequencies have not been considered since they are not yet well defined. Their impact on the residual OPD could however be minimised by the use of an appropriate Butterworth filter.

3.2. Control loop performance

As indicated in the previous section, the level of OPD would be of the order of 1 μm rms without an appropriate control loop. This is prohibitive for exozodiacal disc detection and fringe tracker is by consequent mandatory to stabilize the OPD to a smaller value. In GENIEsim, the simulation of the control loop is achieved by a simultaneous optimization of the repetition frequency and of the controller parameters (a simple PID[1]). Optimising the repetition frequency of the control loops, the residual OPD and tip/tilt disturbances can be reduced to the values given in Table 2, computed for a Sun-like star located at 20 pc. As for ALADDIN, dispersion and intensity control loops have been disabled in GENIEsim to enable the simulation of Pegase. This is indicated by a 0 Hz control frequency. Note that the results presented for GENIE and ALADDIN assume the "best case scenario" which takes into account pupil averaging; a method which reduces the power spectral density of piston and dispersion (see paper I for more details).

In the case of Pegase, Table 2 shows that the fringe tracking can be carried out at much lower frequencies (about 100 HZ instead of 2 KHz) and lead to lower residual positional errors. The pointing accuracy can also be controlled at lower frequencies (500 Hz instead of 1 kHz) but the residual tip/tilt is larger. The instrumental nulling performance is however slightly better than in the cases of ALADDIN and GENIE because it is dominated by the residual OPD error. Taking into account the geometric leakage, the overall nulling performance of ALADDIN is still better by a factor 2 than the one of Pegase. This is a direct consequence of the minimum baseline length of Pegase imposed by the free-flying collision avoidance distance of 20 m (corresponding to a 40 m nulling baseline length in the linear configuration).

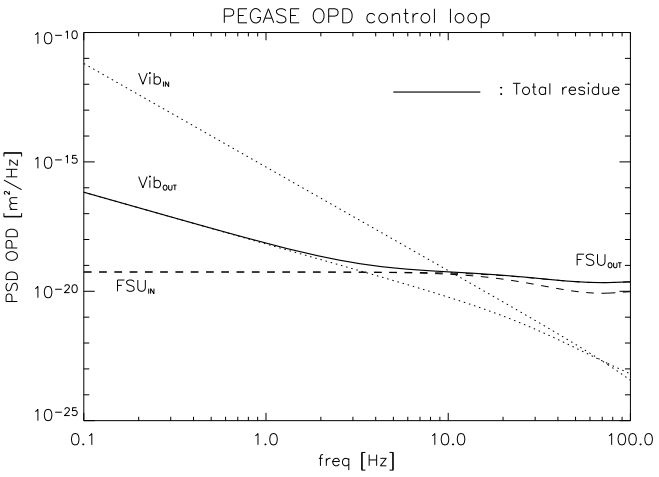

Fig. 3. Dotted curves: power spectral density of the OPD at the input (vib$_{in}$) and at the output (vib$_{out}$) of the Pegase control loop. Dashed curves: PSD of the fringe sensing unit before (FSU$_{in}$) and after (FSU$_{out}$) the Pegase control loop. The solid line shows the total closed-loop OPD jitter.

[1] PID stands for "Proportional, Integral and Differential" which is a basic controller device for closed-loop control

Table 3. Expected sensitivity of Pegase for the linear and triangular configurations (40-m and 20-m baseline lengths respectively), given in number of zodis that can be detected around a Sun-like star located at 20 pc in 30 min. The individual contributions are given in photo-electrons detected at the nulled output, assuming a 1% precision on diameter measurements. The dash sign indicates that no calibration is performed.

	LINEAR	TRIANGULAR
20-zodi signal [e-]	3.7×10^4	1.6×10^4
Shot noise [e-]	1.1×10^3	1.1×10^3
Detector noise [e-]	5.7×10^2	5.7×10^2
Instability noise [e-]	3.3×10^2	3.3×10^2
Calibrated geom. leakage [e-]	2.0×10^4	4.9×10^3
Raw instr. leakage [e-]	1.4×10^4	1.4×10^4
Calibrated instr. leakage [e-]	-	5.0×10^3
Zodis for SNR=5 (raw)	2612	1487
Zodis for SNR=5 (calibrated)	74	43

By consequent, Pegase should fly in triangular configuration in order to be able to compete with ALADDIN.

Finally, Fig. 3 shows the PSD of vibrations before and after the control loop. The PSD of the fringe sensing unit (FSU) is also represented. The solid curve indicates the total residue after correction by the FSU, limited at low frequencies (below $\sim$ 10 Hz) by the non-perfect control of the input perturbations and by the noise of the FSU beyond 10 Hz. Note that the value derived by GENIEsim for the FSU noise is in agreement with the requirements of 0.56 nm/$\sqrt{\text{Hz}}$ derived by the Astrium study (Villien et al. 2007).

4. Performance of Pegase

In this section, we report the results obtained with GENIEsim applied to Pegase for the exozodiacal disc detection. Let us remind that the primary objective of Pegase is the spectral characterisation of hot giant extrasolar planets and that its design has been optimised for this purpose.

4.1. Signal-to-noise ratio

Before giving a general overview of the performance expected from Pegase (see section 4.2), it is necessary to present the level at which each individual source of noise generally contributes to the final SNR. Considering a Sun-like star located at 20 pc, Table 3 gives the individual contributions to the SNR in photo-electrons detected at the nulled output for an integration time of 30 min and assuming 1% precision on diameter measurements ($\Delta\theta_\star$). The circumstellar disc is assumed to follow the same model as in the solar system (Kelsall et al. 1998), except for a global density factor of 20.

As evidenced for GENIE and ALADDIN, Table 3 shows that calibrating the nulled output improves significantly the sensitivity of Pegase. However, whereas the calibration of the instrumental leakage is very efficient for the ground-based instruments (see Papers I and II), it would impair the performance of the linear Pegase since the calibrated geometric leakage is largely dominant (for a knowledge of 1% on the stellar angular diameter). Indeed, the calibration of the instrumental leakage is achieved by observing a calibrator star which is affected by its own geometrical leakage. The absence of calibration is indicated by a dash sign in Table 3. For the triangular configuration, the geometric leakage is much lower due to the shorter baseline length and the calibration of the instrumental leakage can be restored.

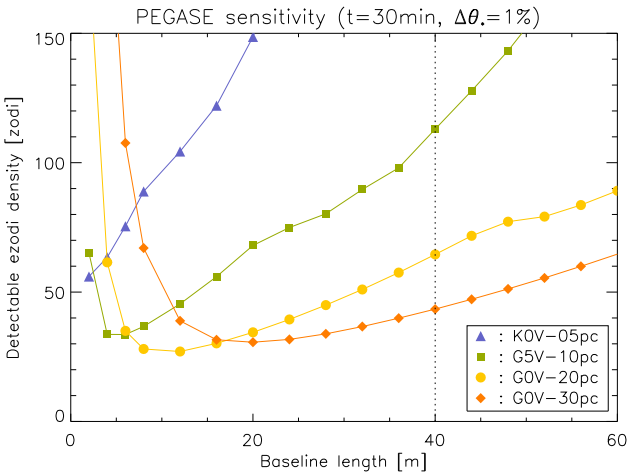

Fig. 4. Simulated performance of Pegase for four typical Darwin targets with respect to the baseline length, assuming 1% uncertainty on the stellar angular diameter ($\Delta\theta_\star$) and an integration time of 30 min.

These results confirms that the triangular configuration is much more suited for the detection of exozodiacal discs.

Finally, note that shot and detector noises are not dominant contributors to the noise budget and increasing the integration time should not improve significantly the sensitivity. The shot noise is dominated by the stellar leakage and the emission of the local zodiacal cloud. In the absence of atmosphere, the latter becomes the main background contributor and overwhelms the instrumental brightness by a factor $\sim$1000 at 3.5 μm.

4.2. Estimated sensitivity

Following the method used for the GENIE and ALADDIN studies (see Paper I and II), the performance of Pegase is presented for 4 hypothetic targets representative of the Darwin catalogue (Kaltenegger et al. 2007): a K0V at 5 pc, a G5V at 10 pc, a G0V at 20 pc and a G0V at 30 pc. Unless specified otherwise, the integration time has been fixed to 30 min and the accuracy on the stellar angular diameters to 1%.

Using the parameters listed in Table 1, the results of the simulation are presented in Fig. 4 taking into account the usual calibration procedures (i.e. background subtraction, geometric leakage calibration and instrumental leakage calibration - see Paper I) when it is necessary. The detection threshold for detection is set at a global SNR of 5, including the residuals from background subtraction and from the calibration of the stellar leakage. As suggested by Table 3, the sensitivity at long baseline lengths is fully dominated by the geometric leakage, especially for the closest targets which have a larger angular diameter. By reducing the baseline length, the geometric cancellation of the starlight gets better and the sensitivity curves decrease towards a minimum, indicating the optimum baseline length. At short baseline lengths, the instability noise becomes dominant and the sensitivity curves rise again due to the decrease of the exozodiacal disc transmission. The slight deviation of the sensitivity curves (see for instance at a baseline length of 8 m for the K0V star) indicates where the instrumental leakage calibration is restored. Comparing with the results of Paper II, Fig. 4 shows that the optimum baseline length for surveying typical Darwin targets with Pegase is always shorter than with ALADDIN. This is due to the higher thermal background in the case of ALADDIN, which constraints the sensitivity curves at short baseline lengths.

Table 4. Performance comparison between GENIE, ALADDIN and Pegase expressed in detectable exozodiacal disc densities as compared to the solar zodiacal disc (for different uncertainties on the stellar angular diameter and an integration time of 30 min).

Star	0%	0.5%	1%	1.5%	Instrument
K0V - 5pc	39	90	120	150	GENIE - AT
	2.0	220	450	680	GENIE - UT
	5.0	33	55	79	ALADDIN
	0.5	200	390	580	LIN. Pegase
	0.5	81	150	220	TRI. Pegase
G5V - 10pc	91	130	150	180	GENIE - AT
	4.5	59	120	180	GENIE - UT
	8.6	24	37	51	ALADDIN
	0.8	63	110	160	LIN. Pegase
	0.8	34	68	92	TRI. Pegase
G0V - 20pc	240	260	280	300	GENIE - AT
	10	29	50	73	GENIE - UT
	17	25	39	48	ALADDIN
	1.5	32	64	90	LIN. Pegase
	1.5	18	34	51	TRI. Pegase
G0V - 30pc	570	590	600	620	GENIE - AT
	26	46	59	71	GENIE - UT
	61	62	66	72	ALADDIN
	3.7	22	43	65	LIN. Pegase
	3.7	18	30	42	TRI. Pegase

Since the optimum baseline is in any case shorter than 40 m, we can conclude from Fig. 4 that the sensitivity of Pegase can be significantly improved by considering a triangular configuration. For instance, the triangular Pegase is sensitive to a 60-zodi disc around a G5V star located at 10 pc while the linear configuration only to a 110-zodi disc. This gain by considering a triangular configuration decreases with the target distance as illustrated by Fig. 5. Note however from Fig. 4 that the sensitivity can still be improved by considering baseline lengths shorter than 20 m for the 3 closest targets. The feasibility of such a compact flight configuration is however beyond the scope of this paper and will not be addressed.

4.3. Comparison with ground-based sites

As discussed in the previous sections, Pegase is generally limited by the geometric leakage due to the free-flying constraints which make unavailable the optimum baseline length. Beside reducing the nulling baseline length, another way to minimise the geometric leakage is to improve the knowledge of the stellar angular diameter. This parameter is thereby very important in the actual performance of Pegase. Considering the four targets representative of the Darwin catalogue, Tab. 4 gives the sensitivity to exozodiacal discs of Pegase for different uncertainties on the stellar angular diameter. The results of GENIE on the auxiliary telescopes (AT - 1.8 m diameter), unit telescopes (UT - 8 m diameter) and ALADDIN are also presented for comparison (from Paper I and Paper II).

Table 4 shows that in its triangular configuration, Pegase always outperforms GENIE while in its linear configuration, it is less efficient than GENIE only for the K0V star located at 5 pc. The comparison with ALADDIN is more contrasted. Both linear and triangular Pegase present a better sensitivity than ALADDIN for the G0V star at 30 pc. For the G0V star located at 20 pc, ALADDIN and the triangular Pegase show very similar sensitivities but the advantage of ALADDIN rises for the two closest stars. The triangular Pegase has generally a better sensitivity than the linear one due to its smallest nulling baseline. The gain by considering a triangular configuration with a minimum nulling baseline length of 20 m is evidenced in Fig. 5. In Table 4, the results for a perfect knowledge the stellar angular diameter ($\Delta\theta_\star$=0) are useful to indicate the performance of each instrument disregarding the limitation coming from the baseline constraints. This can be interpreted as the "instrumental performance". In that case, Pegase always largely exceeds the ground-based instruments.

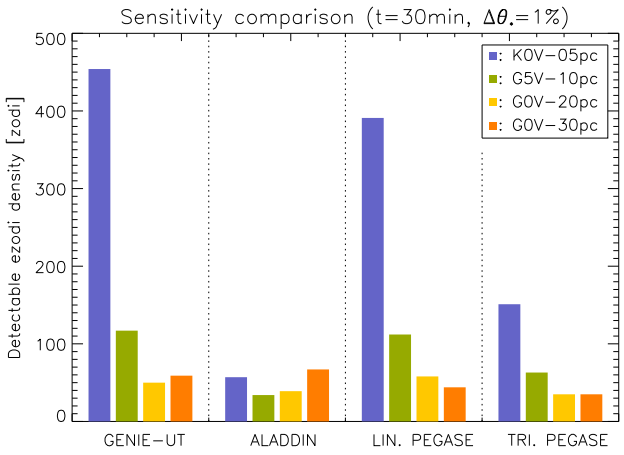

Fig. 5. Expected performance for the triangular Pegase compared to the other concepts considering a 20-m nulling baseline (for 30 min integration time and 1% uncertainty on the stellar angular diameters).

The conclusion of this part is that the triangular Pegase should be preferred to the linear configuration since it presents in any cases a better sensitivity. For the most distant targets, Pegase is more efficient than ALADDIN, which remains the best solution to survey the closest stars. Finally, to give a thorough comparison between the achievable sensitivity from space and from the main ground-based sites, it is interesting to investigate the impact on the performance of the integration time. This is discussed in the following section.

4.4. Influence of the integration time

Increasing the integration time has different influences on the individual SNRs. For instance, shot noise, detector noise and instability noise (to the first order) have the classical $t^{1/2}$ dependance and their relative impacts on the final SNR decrease for longer integration times. On the other hand, the imperfect calibration of geometric and instrumental stellar leakage is proportional to time and increasing the integration time has no influence on the final SNR. Therefore, since it is geometric leakage rather than shot noise which is the dominant noise contributor (see section 4.1), increasing the integration time does not improved significantly the sensitivity to exozodiacal disc detection. The sensitivity of the triangular Pegase for different integration times is represented in Fig. 6, considering that the stellar angular diameter is known with a precision of 1% and the optimum baseline length.

After an integration times of about 15 minutes, Pegase has reached its maximum sensitivity and as expected, increasing the integration time would be useless. For the two closest stars (the K0V at 5 pc and the G5V at 10 pc), the integration time can be reduced down to 1 min without loosing sensitivity. For the fainter targets, the sensitivity begins to decay significantly below 5 min and 15 min of integration time for G0V stars located respectively

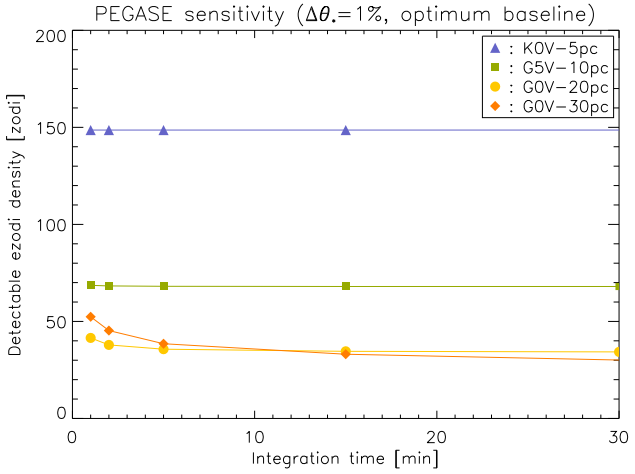

Fig. 6. Simulated performance of the triangular Pegase in terms of exozodiacal disc detection for an uncertainty on the stellar angular diameter of 1% ($\Delta\theta_\star$) with respect to the integration time.

at 20 and 30 pc. Due to the low thermal background, Pegase achieves its maximum sensitivity much faster than GENIE and ALADDIN. Nevertheless, the goal sensitivity of 20 zodis could not be achieved on the contrary to ALADDIN which could reach this level after about 8 hours of integration time for G0V stars located between 20 and 30 pc.

5. Conclusions

Despite relatively small telescopes (40 cm diameter), the space-based nulling interferometer Pegase presents very attractive capabilities for the exozodiacal disc detection. In its nominal linear configuration, Pegase generally exceeds the sensitivity of GENIE and competes with the 1-m telescope nulling interferometer for Antarctica (ALADDIN) for the most distant targets of the Darwin/TPF catalogue. The performance would be significantly boosted by considering a shorter-baseline configuration (i.e. a triangular Pegase), since the nominal linear Pegase is in any case limited by the stellar geometric leakage. Reducing the free-flying collision avoidance distance is thereby of crucial relevance to the final sensitivity of Pegase. For an integration time of 15 minutes, a triangular Pegase with a minimum baseline length of 20 m could detect exozodiacal discs about 30 times as dense as our own solar disc to outperform ALADDIN for the most distant targets. The optimum sensitivity is achieved very quickly (in few minutes) due to the low thermal background. However, the 20-zodi sensitivity goal, achievable with ALADDIN for long integration times, seems out-of-reach.

Even if it has not been designed for that, Pegase could be a very valuable instrument to assess quickly the level of circumstellar dust around the Darwin/TPF targets. However, in addition to be less expensive, ALADDIN generally achieves a better sensitivity for long integration times. Regarding the exozodiacal disc detection around the Darwin/TPF targets as sole objective, ALADDIN presents a better performance/price ratio than PEGASE and should be preferred, particularly if the final objective is to reach a sensitivity at the level of 20 zodis.

Acknowledgements. The authors are indebted to R. den Hartog for his major contribution to the development of GENIEsim and his expert advice for the adaptation to Pegase. The first author acknowledges the support of the Belgian National Science Foundation (“FRIA”).

References

Absil, O. 2001, Master’s thesis, Liège University, Liège, Belgium, *http://vela.astro.ulg.ac.be/themes/telins/harigs/*
Absil, O. 2006, PhD thesis, Liège University, Liège, Belgium
Absil, O., Coudé du Foresto, V., Barillot, M., & Swain, M. 2007, A&A, submitted
Absil, O., den Hartog, R., Gondoin, P., et al. 2006a, A&A, 448, 787
Absil, O., di Folco, E., Mérand, A., et al. 2006b, A&A, 452, 237
Beichman, C., Lawson, P., Lay, O., et al. 2006, in Advances in Stellar Interferometry. Edited by Monnier, John D.; Schöller, Markus; Danchi, William C.. Proceedings of the SPIE, Volume 6268, pp. 62680S (2006)., Vol. 6268
Coudé du Foresto, V., Absil, O., Swain, M., Vakili, F., & Barillot, M. 2006, in Presented at the Society of Photo-Optical Instrumentation Engineers (SPIE) Conference, Vol. 6268, Advances in Stellar Interferometry. Edited by Monnier, John D.; Schöller, Markus; Danchi, William C.. Proceedings of the SPIE, Volume 6268, pp. 626810 (2006).
Defrère, D., Absil, O., Hanot, C., & Fridlund, M. 2007, in Proceedings of the SPIE (2007)., Presented at the Society of Photo-Optical Instrumentation Engineers (SPIE) Conference, 6693–6694
Fridlund, C. V. M., d’Arcio, L., den Hartog, R., & Karlsson, A. 2006, in Advances in Stellar Interferometry. Edited by Monnier, John D.; Schöller, Markus; Danchi, William C.. Proceedings of the SPIE, Volume 6268, pp. 62680R (2006)., Vol. 6268
Gondoin, P. A., Absil, O., den Hartog, R. H., et al. 2004, in New Frontiers in Stellar Interferometry, Proceedings of SPIE Volume 5491. Edited by Wesley A. Traub. Bellingham, WA: The International Society for Optical Engineering, 2004., p.775, ed. W. A. Traub, Vol. 5491, 775–+
Hinz, P. M., Angel, J. R. P., Woolf, N. J., Hoffmann, W. F., & McCarthy, D. W. 2000, in Presented at the Society of Photo-Optical Instrumentation Engineers (SPIE) Conference, Vol. 4006, Proc. SPIE Vol. 4006, p. 349-353, Interferometry in Optical Astronomy, Pierre J. Lena; Andreas Quirrenbach; Eds., ed. P. J. Lena & A. Quirrenbach, 349–353
Kaltenegger, L., Eiroa, C., Stankov, A., & Fridlund, M. 2007, A&A, submitted
Kelsall, T., Weiland, J. L., Franz, B. A., et al. 1998, ApJ, 508, 44
Lay, O. P. 2004, Appl. Opt., 43, 6100
Le Duigou, J. M., Ollivier, M., Léger, A., et al. 2006, in Space Telescopes and Instrumentation I: Optical, Infrared, and Millimeter. Edited by Mather, John C.; MacEwen, Howard A.; de Graauw, Mattheus W. M.. Proceedings of the SPIE, Volume 6265, pp. 62651M (2006)., Vol. 6265
Meyer, M. R., Hillenbrand, L. A., Backman, D., et al. 2007, ArXiv Astrophysics e-prints
Serabyn, E. 1999, Appl. Opt., 38, 4213
Serabyn, E., Booth, A., Colavita, M. M., et al. 2006, in Advances in Stellar Interferometry. Edited by Monnier, John D.; Schöller, Markus; Danchi, William C.. Proceedings of the SPIE, Volume 6268, pp. 626815 (2006)., Vol. 6268
Sterken, V. 2005, Master’s thesis, Delft University of Technology
Sterken, V., Kamp, A., Kampen, S., & van den Dool, T. 2005, in Proceedings of the IAC (2005)., IAC-05- C.2.5
Villien, A., Morand, J., Delpech, M., & Guidotti, P. 2007, in 17th IFAC Symposium on Automatic Control in Aerospace
Wagner, R. M. 2006, in Presented at the Society of Photo-Optical Instrumentation Engineers (SPIE) Conference, Vol. 6269, Ground-based and Airborne Instrumentation for Astronomy. Edited by McLean, Ian S.; Iye, Masanori. Proceedings of the SPIE, Volume 6269, pp. 626909 (2006).
Wallner, O., Flatscher, R., & Ergenzinger, K. 2006, Appl. Opt., 45, 4404

3.4 The Pegasus mission

Pegasus was initially referred to as "DARWIN Lite" or "Super-Pegase" and is a Bracewell interferometer built on the previously described Pegase mission. It has been studied to assess the relevance of a down-scoped DARWIN for the Cosmic Vision 2015-2025 programme. The idea was to study the single Bracewell concept to assess which of DARWIN's objectives could be achieved. This has been done first by optimising Pegase specifications for the detection of Earth-like planets, which means particularly bigger telescopes, cooler optics and an optimised wavelength range. The analysis was then extended to planets with different orbits to give a general overview of the instrument's capabilities. One of the major challenges in detecting an Earth-like planet is to mitigate the emission of the exozodiacal cloud which cannot be subtracted by internal modulation, as in the case of DARWIN. Specific methods for Bracewell interferometers, such as split-pupil and OPD modulation, have been investigated. The study was performed in the framework of the present master thesis in partnership with ESA/ESTEC.

3.4.1 Concept overview

Pegasus consists in two 1-m diameter telescopes and one beam combiner spacecraft, free flying at least 20 m away from each other (20 m is the minimum distance to avoid the collision of the spacecraft). The linear configuration of Pegase with a central beam combiner is not convenient for Pegasus since most of the targets in the DARWIN catalogue would require a baseline length shorter than 40 m when observing the host star's HZ (at 10 μm, see Figure 3.8).

Pegasus is therefore better configured as being triangular, which makes baseline lengths shorter than 40 m available (see Figure 1 in the article presented in section 3.5.3). According to CNES, it is conceivable to consider a minimal baseline reduced to 20 m if a triangular configuration is adopted, with the beam combiner at one angle. In that case, the payload has to be designed with an angle of 120° between the incoming beams instead of the 180° in the linear case. This point has still to be assessed. The waveband ranges from 9 to 13 μm with a spectral resolution of 60. In the nulling mode, control loops have to stabilise the OPD to an rms value of 1 nm and the pointing accuracy to 20 mas (instead of 2.5 nm and 30 mas respectively for Pegase). An rms OPD error of 1 nm is very challenging but should be realistic in the near-term future (Lawson 2006). At 10 μm, the main challenge to detect an Earth-like planet is nevertheless the exozodiacal emission, which can be up to 400 times brighter than an Earth located at 20 pc. Internal modulation used in the case of DARWIN is not appropriate since it requires at least 3 telescopes. On the other hand, modulation by rotation of the interferometer can generally

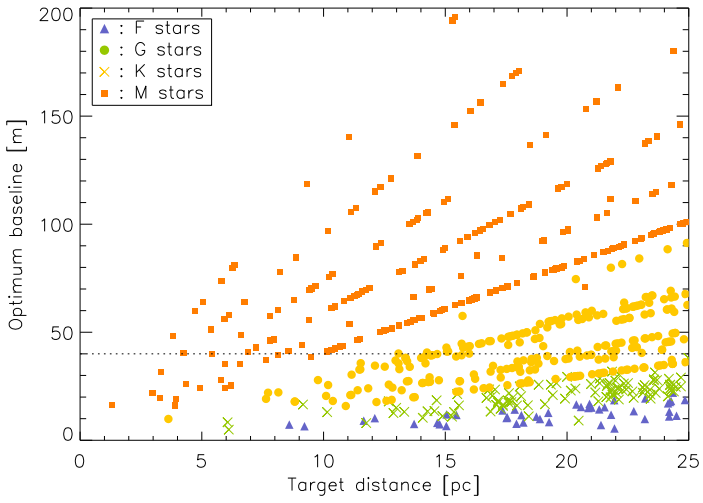

Figure 3.8: Optimum baseline length to observe the habitable zone of Darwin targets with respect to the target distance (at 10 μm).

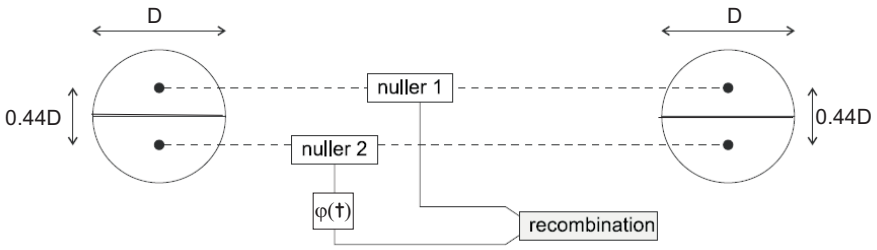

Figure 3.9: Principle of the pupil division technique ("split-pupil Bracewell"). The corresponding transmission maps are given in Figure 3.10.

not be implemented sufficiently fast and the planet signal is easily corrupted by long term drifts and $1/f$ noise. The solution to remove the exozodiacal emission (at least partially) with a single Bracewell interferometer is rather to use one of the specific schemes described hereafter.

3.4.2 The split-pupil technique

Pupil division is a technique developed for the KIN (Serabyn *et al.* 2006) to perform phase modulation with only two telescopes. In this configuration, both telescope pupils are spatially divided into two parts, creating two independent Bracewell interferometers (see Figure 3.9). The outputs of these two interferometers are then combined with a time-varying phase shift (φ(t)). Assuming that the final beam combination is done in a co-axial way on a lossless beam combiner, the same background flux will be measured in both outputs of the beam splitter, simultaneously in time, allowing in theory a perfect background subtraction. A recent review of this method in the context of the Darwin mission has been done by Hanot (2005).

There are two ways to perform the phase modulation, corresponding to two possibilities for the modulation function φ(t):

- **Discrete phase modulation.** In this method, an achromatic phase shift is applied to one of the two nulled beams before the final combination so that the half pupils are put out of phase. In this condition, all coherent signals will be directed to only one of the two outputs of the beam splitter. A simple subtraction of the two detected fluxes will thus be sufficient to single out the coherent signals. In order to avoid potential systematic errors, the role of the two outputs should be repeatedly changed by putting the phase shift alternately in one or the other nulled beam. The transmission map of the total instrument, including the final beam combination, is illustrated in Figure 3.10 (top row), where the left figure corresponds to a phase shift of $\pi/2$ and the right figure to a phase shift of $3\pi/2$ between the semi-pupils.
- **Continuous phase modulation**. Phase modulation can also be implemented as a variation of the OPD in one arm of the interferometer (chromatic phase modulation). In this configuration, the background subtraction can benefit both from the variation of coherent signals in each output and from the fact that two complementary outputs are available. Moreover, additional information on the morphology of the circumstellar disc can be retrieved from the shape of the time-modulated signals. For instance, if the brightness of the disc mainly comes from the inner region, the modulation will show steep gradients as the wide fringe pattern associated with the short baseline scans this region. An extended disc emission, on the other hand, will produce a smooth modulation curve. Disc asymmetries could also be detected, because they produce a slightly asymmetric modulation curve.

The modulation map, proportional to the difference between the transmission maps (see Equation 2.25), is shown in the bottom row of Figure 3.10, displaying a maximum rotational modulation

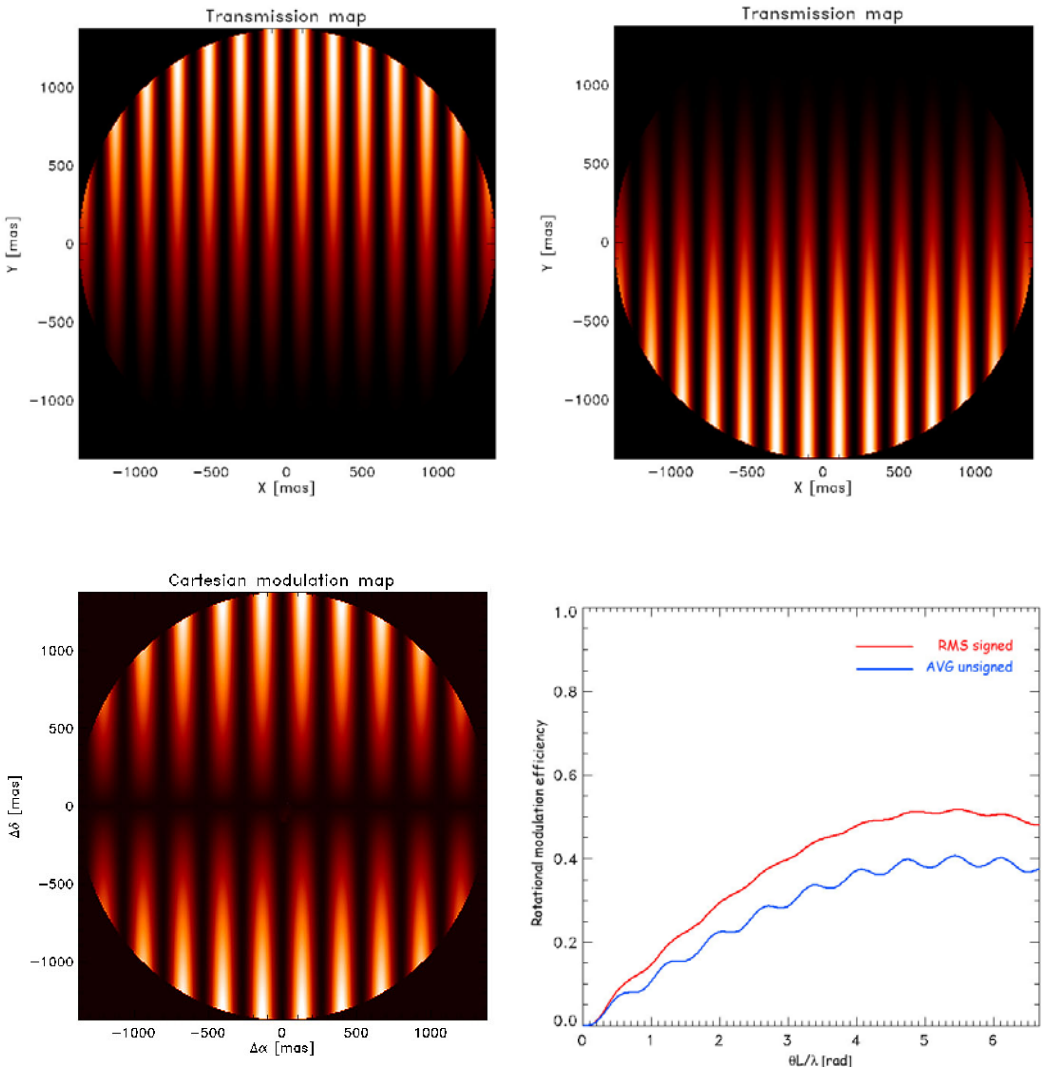

Figure 3.10: Top row, monochromatic transmission maps of a split pupil interferometer with 2-m collectors for a factor λ/b fixed at 2×10^{-6} (corresponding for example to λ=10 μm and a baseline length of 5 m). The left figure corresponds to $\varphi(t)=\pi/2$ while the right figure to $\varphi(t)=3\pi/2$. Bottom row, corresponding modulation map (left) and rotational modulation efficiency (right).

efficiency of about 50%. Although splitting the pupil provides theoretically a perfect background subtraction, splitting the pupil introduces significant additional complexity: instead of having only one nuller, this configuration would require two nullers and an additional beam combiner. Most of the hardware will thus be duplicated, including the control sub-systems, such as required for fringe tracking and intensity control.

3.4.3 The OPD modulation technique

The principle of OPD modulation is to sweep back and forth the dark fringe of the transmission map by modulating the path length in one arm of the interferometer. In this way, all centro-symmetric sources are modulated at twice the modulation frequency. The principle of this technique is illustrated in Figure 3.11. Starting from a situation where the minimum of the transmission map (null) is centered on the star, any shift either to left or right will increase the stellar leakage. By placing the planet in between a crest and a valley (i.e. on the grey fringe), a shift of the transmission map to the right will decrease the planetary transmission while a shift to the left will increase it. As a result, the stellar

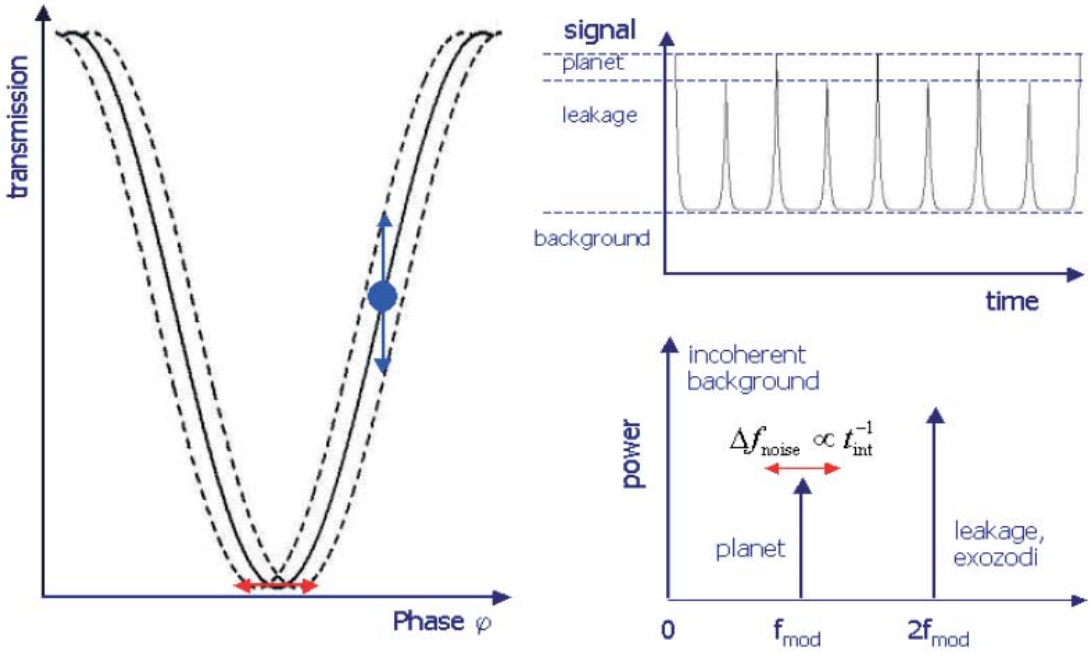

Figure 3.11: Principle of OPD modulation. By locating the planet on a grey fringe, any excursion of phase (OPD) induces a maximum change of the planetary signal, whereby in the illustrated case an increase of phase induces a decrease of planetary signal and vice versa. Provided the null in the transmission map is centered on the star, any phase excursion will only induce an increase in the stellar leakage. When the phase is modulated with a frequency f_{mod}, the stellar leakage is therefore modulated at twice this frequency, allowing a separation of the planetary signal and the leakage in frequency space. The more modulation cycles are present in the data, the sharper the lines in frequency space will become (figure from den Hartog *et al.* 2004) .

leakage is modulated at twice the frequency as in any other symmetric source such as the exozodiacal cloud whereas the planetary signal is modulated at the modulation frequency (see Figure 3.11). Hence both signals can be separated in frequency space, using synchronous coherent demodulation.

In principle, fast planet modulation could be implemented at little increase of the system complexity as a simple sinusoidal offset to the zero point setting of the OPD controller. However, OPD modulation is chromatic, i.e. the phase modulation amplitude varies as the inverse of the wavelength. Nominal response over the full bandwidth could be restored by modulating the phase of the beams, instead of their path length. At least one of the Achromatic Phase Shifter (APS) devices developed for DARWIN could operate as an achromatic phase modulator over the required range of $\pm$ 0.5 radians. Unfortunately, in presence of instrumental errors, the planetary signal is not the only signal to be modulated at the modulation frequency. If the null in the transmission map is not exactly centered on the star (e.g. due to a systematic offset or quasi-static residuals in the OPD between the arms), the part of the stellar disc that is asymmetric with respect to the modulation of the transmission map will start to act as a pseudo-planet. The instrumental errors are a severe limitation to this technique (D'Arcio *et al.* 2004).

3.5 Performance for planet detection

Although GENIEsim is now ready to simulate the performance of Pegase for planet detection, the results presented in this section have been obtained by adapting a top-level performance prediction tool developed by O. Absil for Pegase (Absil 2006) and using several routines of the Darwin science simulator, DARWINsim (see section 4.3 for more details, den Hartog 2005b). The main reason is because the

results presented in this section have been computed before the adaptation of GENIEsim to Pegase. This simulation software is built on excell work-sheets in combination with Visual Basic for Applications (VBA). It can be considered as an approximation of GENIEsim, with several simplifying assumptions. In particular, the most restrictive assumption is relative to the instability noise, only computed at the first order. This is a major limitation to the performance assessment since it has been shown that second order effects of the instability noise are the dominant noise contributors (Lay 2004). However, first performance comparisons with the GENIEsim software already indicates similar results.

3.5.1 The simulation software

The initial simulation tool is a static excel worksheet which looks like as in Table 3.2. In this figure, the output of the software is presented for Pegase and for 5 representative targets (τ *Boo b, 55 Cnc b, 51 Peg b, 55 Cnc e* and *Gl 876 d*). Any modifications in the instrumental configuration or in the data of the target system results in an immediate update of the individual SNRs. The way to compute each cell value is thoroughly discussed in the thesis of Absil (2006) and briefly reminded in the paper hereafter (see section 3.5.3). In the following paragraphs, we give some details on the contents of Table 3.2 necessary to the understanding of the table. Each group of lines is related to one specific aspect of the SNR computation:

- The instrument block describes the interferometer with its fundamental parameters such as collector diameter, baseline length, observing wavelength, spectral resolution, etc. The baseline length is always optimised so as to provide an optimum SNR at the optimum wavelength (in the Pegase waveband in the present case). Note that the actual optimum baseline is smaller than the baseline which would locate the planet on a maximum of the transmission map (see the planetary transmission line). This is due to the fact that the planetary transmission does not significantly decrease when increasing the baseline, while stellar leakage is much more sensitive to the baseline length (see section 3.5.2 for more details). The values given for the total throughput and total emissivity both take into account the detector quantum efficiency. The instrumental rejection ratio is deduced from the contributions of OPD and tip-tilt errors, characterised by their standard deviation.

- The target star data comes from the extrasolar planet encyclopedia (Schneider 2007) when available and otherwise from the Darwin full extrasolar planet catalogue (Stankov 2005). The flux of the star is computed with a blackbody model. The total stellar flux on output is computed by considering both the geometric and the instrumental rejection ratios. The geometric rejection (the inverse of the nulling ratio) is computed using Equation 2.15 while the instrumental rejection is computed using Equation 1 and 2 in the paper presented in section 3.5.3.

- The planetary parameters come also from the extrasolar planet encyclopedia (Schneider 2007) and the thermal and reflected emissions are computed according to Equation 6 in the paper presented in section 3.5.3.

- The background block considers the emissions of the local zodiacal dust, computed using the model of Kelsall (Kelsall *et al.* 1998), and of the instrumental background, computed as a grey body with an emissivity given in the instrument block of the table. The background fluctuation is the standard deviation of the instrumental background and is only related to the temperature fluctuations of the payload. The output flux is computed by multiplying these contributions by the effective field-of-view area, i.e. $0.772(\lambda/D)^2$. The emission of the exozodiacal cloud is also taken into account when necessary. This is the case for Pegusus which works at longer wavelengthes where the exozodiacal emission becomes dominant. A specific routine ("exo_zodi.pro") of DARWINsim has been used to assess the level of exozodiacal emission.

- The individual noise block summarizes the contribution of each source as a function of time. Due to its Poisson statistics, shot noise increases as the square root of time. Read-out noise shows the same

time behaviour because the individual noise realisations experienced in successive read-outs add quadratically. The three other sources of noise are all proportional to time. These contributions are in fact biases, i.e. the residues of imperfect calibration or subtraction processes. Instrumental nulling noise and stellar leakage calibration noise are both proportional to the stellar signal, while background fluctuation noise is proportional to the background signal. The knowledge of the stellar diameter is assumed to be equal to 1% which gives a calibration accuracy for geometric stellar leakage of 2%. Note that this value is different from the one considered by Absil (2006) (a calibration accuracy for geometric stellar leakage of 2%). In addition to the new specifications of Pegase, this explains the discrepancy with the previous performance assessment of Pegase (Absil 2006).

- Using the integration time specified in the first line of this block, the individual signal-to-noise ratios are computed for the four noise sources. Shot noise and read-out noise are taken into account jointly in the detection SNR. While the detection SNR increases as the square root of time, the three others remain the same whatever the integration time. It must be noted that, with an integration time of 10 hours, the detection SNR is already comfortably larger than the instrumental SNR for most targets. Longer integration times would thus only marginally improve the final SNR.

- The final SNR has been computed by the combination of the individual SNRs, assuming that the three biases, respectively related to calibration, instrumental errors and background fluctuations, add linearly. Adding them quadratically as totally uncorrelated noise sources would be too optimistic because stellar calibration noise is expected to be correlated with instrumental leakage noise, which is itself correlated with background subtraction noise through the instrumental temperature fluctuations (which also produce OPD and tip-tilt errors). The final SNR should thus be regarded as a minimum SNR.

This static worksheet is not convenient for optimisation purposes because it requires several attempts "by hands" and an expert eye. For this reason and in the context of this master thesis, the software has been updated using Visual Basic for Application (VBA). The software now performs various optimisations (e.g. wavelength, baseline length) automatically. For each wavelength, the optimum baseline length is computed. The software then compares the results at different wavelengths to give the optimum wavelength-baseline pair. This process can be executed on the whole list of known extrasolar planets as well as on the Darwin catalogue. After the optimisation phase, the targets are sorted by ascending integration time, either in the optimum wavelength element (for spectroscopy) or on the full wavelength range (for detection). Considering 50% downtime and that each system has to be surveyed three times in order to reach a good confidence in case of non detection, the sorted list is cut off where the cumulative integration time exceeds the nominal survey period. The resulting list defines the number of targets that can be surveyed. Several other outputs are given such as the number of targets of a given spectral type which can be surveyed in a given time, the list of planets sorted by increasing integration time, decreasing SNR, etc.

	Tau Boo b	*55 Cnc b*	*51 Peg b*	*55 Cnc e*	*Gl 876 d*
Instrument					
Diameter [m]	0.4	0.4	0.4	0.4	0.4
Optimum baseline [m]	70	50	61	89	59
Wavelength [μm]	4.5	5.5	5	5	5.5
Spectral resolution	60	60	60	60	60
Total throughput	0.042	0.042	0.042	0.042	0.042
Total emissivity	0.25	0.25	0.25	0.25	0.25
Calib. accuracy	0.02	0.02	0.02	0.02	0.02
Instrument temp. [K]	90	90	90	90	90
Rms temp. fluct. [K]	0.1	0.1	0.1	0.1	0.1
Rms OPD error [nm]	2.5	2.5	2.5	2.5	2.5
Rms pointing error [mas]	30	30	30	30	30
Instrumental nulling	323761	485855	400754	400754	485855
Star					
Distance [pc]	15.0	13.4	15.4	13.4	4.7
Spectral type	F7V	G8 V	G2 IV	G8 V	M4 V
Radius [$R_\odot$]	0.84	0.6	1.17	0.6	0.36
Angular radius [mas]	0.26	0.21	0.35	0.21	0.36
Effective temperature [K]	6309	5243	5770	5243	3500
Flux [Jy]	3.31	1.18	4.56	1.39	2.01
Geometric nulling	1039.8	4886.6	927.8	1244.5	1173.7
Total stellar nulling	1036.5	4838.0	925.6	1240.7	1170.9
Output flux [Jy]	1.3E-04	1.0E-05	2.1E-04	4.7E-05	7.2E-05
Output flux [ph-el/s]	8.48	0.65	13.07	2.98	4.56
Planet					
Semi-major axis [AU]	0.05	0.12	0.05	0.04	0.02
Mass $\times$ sin(i) [M_{Jup}]	3.90	0.78	0.47	0.05	0.02
Radius [R_{Jup}]	1.6	0.9	0.8	0.4	0.3
Bond albedo	0.1	0.1	0.1	0.1	0.1
Equilibrium temp. [K]	1266.5	562.6	1285.7	978.7	683.9
Thermal flux [Jy]	7.1E-03	1.8E-04	1.6E-03	2.1E-04	2.8E-04
Reflected flux [Jy]	4.4E-05	8.7E-07	1.2E-05	1.4E-06	3.6E-06
Star/planet contrast	467	6394	2768	6565	7120
Interf. transmission	0.42	0.81	0.33	0.46	0.42
Output flux [Jy]	1.3E-04	6.3E-06	2.3E-05	4.1E-06	5.0E-06
Output flux [ph-el/s]	7.96	0.40	1.43	0.26	0.31
Background					
Local zodi [Jy/sr]	1.8E+05	6.7E+05	3.5E+05	3.5E+05	6.7E+05
Exo zodi [Jy/sr]	1.2E+05	1.1E+05	1.6E+05	1.1E+05	1.8E+05
Instr. brightness [Jy/sr]	4.1E+01	1.4E+04	1.0E+03	1.0E+03	1.4E+04
Rms bckg fluctuations [Jy/sr]	1.6E+00	4.6E+02	3.7E+01	3.7E+01	4.6E+02
Output flux [Jy]	6.2E-07	4.0E-06	1.4E-06	1.4E-06	4.1E-06
Output flux [ph-el/s]	2.0E-02	1.3E-01	4.5E-02	4.5E-02	1.3E-01
Individual noises					
Shot noise [ph-el/$s^{0.5}$]	4.1E+00	1.1E+00	3.8E+00	1.8E+00	2.2E+00
Detector noise [ph-el/$s^{0.5}$]	1	1	1	1	1
Instr. leakage noise [ph-el/s]	2.7E-02	6.5E-03	3.0E-02	9.2E-03	1.1E-02
Leakage calib. noise [ph-el/s]	1.7E-01	1.3E-02	2.6E-01	6.0E-02	9.1E-02
Bckg fluct. noise [ph-el/s]	6.0E-06	2.6E-03	1.7E-04	1.7E-04	2.6E-03
Individual SNRs					
Integration time [hours]	10	10	10	10	10
Detection SNR	361.4	51.3	68.8	23.9	24.3
Instrumental SNR	293.1	61.6	47.4	28.2	28.5
Calibration SNR	46.9	30.7	5.5	4.4	3.4
Bckg fluctuation SNR	1.3E+06	1.6E+02	8.4E+03	1.5E+03	1.2E+02
Final SNR	36.4	13.4	4.6	3.3	2.7

Table 3.2: Details of the computation of the final signal-to-noise ratio for five extrasolar planets. Full results are given in Section 3.5.4.

3.5.2 Optimum baseline

Figure 3.12 shows the simulated signal-to-noise ratio as a function of the baseline length for three different wavelength (1.5 μm, 3 μm and 5 μm), and for the observation of the hot giant planet *51 Peg b* (a total integration time of 10 hours has been considered). Since the maximum angular separation between *51 Peg b* and its host star is 3.385 mas, the baseline lengths which locate *51 Peg b* on a maximum of each transmissions map should be 46 m, 91 m and 152 m, respectively at 1.5 μm, 3 μm and 5 μm (according to Equation 2.4). However, as illustrated in Figure 3.12, the optimum baseline lengths are smaller and correspond to interferometric transmissions not necessarily close to 1 (see Table 3.2). This behaviour is due to the fact that the planetary transmission does not significantly decrease when increasing the baseline, while stellar leakage is much more sensitive to the baseline length (see the discussions on the stellar leakage in Chapter 2). This conclusion supports and reinforced the relevance of shorter-baseline configurations, as for the detection of exozodiacal discs (see section 3.3).

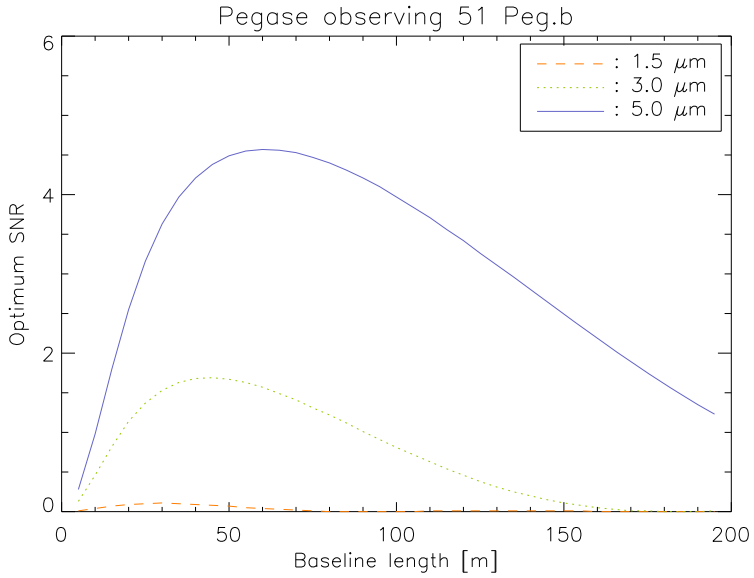

Figure 3.12: Simulated signal-to-noise ratio as a function of the baseline length for three different wavelengths (1.5 μm, 3 μm and 5 μm), and for the observation of the hot giant planet *51 Peg b*. A total integration time of 10 hours has been considered.

3.5.3 Article: *Potential of space-based infrared Bracewell interferometers for planet detection*

The following article (Defrère *et al.* 2007b) presents a performance study of space-based nulling interferometers. In particular, PEGASE and PEGASUS are addressed and their sensitivities towards the detection of known extrasolar planets compared. The performance of PEGASUS to survey the HZ of Darwin targets is also thoroughly addressed.

Potential of space-based infrared Bracewell interferometers for planet detection

D. Defrère*[a], O. Absil[b], C. Hanot[a] and M. Fridlund[c]

[a] Institut d'Astrophysique et de Géophysique de Liège (IAGL), Université de Liège, Belgium
[b] Laboratoire d'Astrophysique de l'Observatoire de Grenoble, France
[c] Astrophysics Mission Division, ESA (ESTEC), The Netherlands

ABSTRACT

The Darwin and TPF-I space missions will be able to study the atmosphere of distant worlds similar to the Earth. Flying these space-based interferometers will however be an extraordinary technological challenge and a first step could be taken by a smaller mission. Several proposals have already been made in this context, using the simplest nulling scheme composed of two collectors, i.e., the original Bracewell interferometer. Two of these projects, viz. Pegase and the Fourier-Kelvin Space Interferometer, show very good perspectives for the characterisation of hot extra-solar giant planets (i.e., Jupiter-size planets orbiting close to their parent star). In this paper, we build on these concepts and try to optimise a Bracewell interferometer for the detection of Earth-like planets. The major challenge is to efficiently subtract the emission of the exo-zodiacal cloud which cannot be suppressed by classical phase chopping techniques as in the case of multi-telescopes nulling interferometers. We investigate the potential performance of split-pupil configurations with phase chopping and of OPD modulation techniques, which are good candidates for such a mitigation. Finally, we give a general overview of the performance to be expected from space-based Bracewell interferometers for the detection of extra-solar planets. In particular, the prospects for known extra-solar planets are presented.

Keywords: Nulling interferometry, space-based mission, extra-solar planets.

1. INTRODUCTION

Nulling interferometry is one of the most promising techniques to study extra-solar planets. The simplest way to implement it is to use a Bracewell interferometer.[1] The principle is to combine the beams coming from two telescopes in phase opposition so that a dark fringe appears on the line of sight, which strongly reduces the starlight emission while letting through the light from an off-axis source by adjusting the baseline length. This concept is used in several space mission projects, like Pegase[2] and the Fourier-Kelvin Stellar Interferometer,[3] aiming at studying extra-solar giant planets (EGP) located close to their parent star. The detection of Earth-like planets is much more challenging due to the higher star/planet contrast. It requires a higher nulling stability over a longer period and specific methods of modulation to suppress the emissions of the local and exo-zodiacal clouds. This should be achieved by the Darwin[4] and TPF-I[5] projects, which are based on a more complex scheme of nulling using at least three collectors. These missions will achieve direct detection and atmospheric characterization of Earth-like planets orbiting in the habitable zone (HZ) of nearby main sequence stars (within ~ 30 pc). They will be fantastic tools to search for biological signatures in our vicinity.[6] Beyond these ambitious objectives, the scientific goals of these missions also include the origin of the planetary systems, its evolutionary history and its future development. The study of hot EGP with Pegase or the Fourier-Kelvin Space Interferometer (FKSI) would already be very fruitful in that respect, but it would be interesting to know what could be achieved with a more advanced Bracewell concept. Improving the specifications of these missions, such as the size of the telescopes, could increase the sensitivity and give additional information on smaller planets. The goal of this study is to assess the performance of such a mission.

* E-mail: defrere@astro.ulg.ac.be, Telephone: 003243669713

2. INSTRUMENTAL CONCEPT

2.1 Overview of the Pegase design

This study considers the CNES formation flying demonstrator Pegase as a baseline.[2] Pegase consists in a two 40-cm diameter apertures interferometer observing in the near-infrared (2.5-5 μm) and formed of three free flying spacecrafts orbiting at the Lagrange point L2. Thanks to this location, the spacecrafts and the focal plane assembly can be passively cooled down to respectively 90 $\pm$ 1 K and 55 $\pm$ 0.1 K. Visibility measurements and recombination in nulling mode are both possible with a spectral resolution of about 60. The formation flying constraints allow baseline lengths from 40 m to 500 m giving an angular resolution in the range of 0.5 mas to 30 mas. The fine-tuning of the optical path difference (OPD in the following) is performed by a dedicated control loop based on a fringe sensor measuring the observed central target in the 0.8-1.5 μm range and an optical delay line. The intensity control is performed by a fine pointing loop using a field relative angle sensor operating in the 0.6-0.8 μm range. This implementation allows to control the OPD down to a level of 2.5 nm rms and the tip/tilt errors to a value of 30 mas rms, corresponding to a nulling ratio of 10^{-4} stable at the level of 10^{-5}.[2]

2.2 Modifying Pegase

If Pegase was pointed towards a Solar system located at 20 pc, it would be inefficient for Earth-like planet detection for several reasons. The main show-stopper is the starlight cancellation which is not sufficiently stable and requires a better control of the OPD. Of minor relevance when observing hot EGPs, the local and exo-zodiacal clouds become very problematic for Earth-like planets and will be major sources of noise in the final budget. A way to improve the sensitivity of the instrument is to optimise the wavelength range of observation. Since Earth-like planets are cooler than hot EGPs, their maximum brightness is shifted toward longer wavelengths. For example, at 10 μm, the emission of an Earth is about 30 times larger than at 2.5 μm while the flux of the exo-zodiacal cloud increases only by a factor 4. In addition, the stellar flux decreases and is 10 times lower at 10 μm than at 2.5 μm. Nevertheless, increasing the observation wavelength is limited by the thermal emission of the instrument which becomes dominant at long wavelengths. The thermal specifications of Pegase would cause overwhelming background fluctuations for Earth-like planets detection. To reach this objective, the instrument has to be cooled down and more thermally stable. This is part of the optimisation presented in this study. The parameters used in our simulations are listed in Table 1.

Spectral	
Wavelength	10 μm
Resolution	60
Target system	
Distance	20 pc
Star radius	1 R_{Sun}
Star eff. temperature	5770 K
Star flux	0.56 Jy
Planet radius	1 R_{Earth}
Planet angular offset	50 mas
Planet eff. temperature	265 K
Planet flux	6.00E-8 Jy
Exo-zodi dust	1 solar system zodi
Local zodi brightness	1.13E+7 Jy/sr
Bracewell specifications	
Telescope diameter	1 m
Baseline length	20 m
Throughput	7%

Table 1. Parameters used in this study

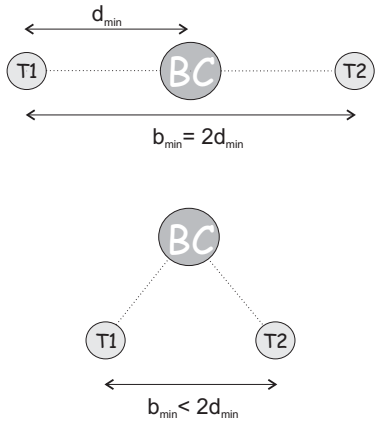

Figure 1. Above: nominal linear flying configuration of Pegase with a central beam combiner. Bottom: modified flying configuration of Pegase allowing a shorter interferometric baseline length.

The observing scenario is based on the one of Pegase. Since the inclination and the position angle of the planetary orbit are unknown, three observations with baselines separated by 60° will be obtained on each target. By consequence, the bright fringe will be closer than 30° from the actual planet position angle for at least one observation and the planet flux will be reduced by a maximum of 5% in the worst case. In addition, since the ephemeris of the planet is unknown, 3 different sets of observations along the orbit are necessary to reach a high level of confidence in case of non detection. A duty cycle of 50% is also considered.

Finally, assuming a minimum anti-collision baseline length of 20 m (d_{min}), the linear configuration of Pegase with a central beam combiner is not convenient to survey the habitable zone of most F and G stars of the Darwin catalogue[7,8] which require baselines shorter than 40 m at 10 μm. To solve this problem, a triangular flying configuration is considered, with the beam combiner spacecraft at equal distance from collector spacecrafts (see Figure 1).

3. SIGNALS AND NOISES IN SPACED-BASED INTERFEROMETRY

3.1 Instrumental stellar leakage

In nulling interferometry, a key quantity is the null depth which determines the level of on-axis stellar rejection. This null depth undergoes fluctuations due to instrumental imperfections such as co-phasing errors, wavefront errors or mismatches in the intensities of the beams. The influence of all these contributions is called instrumental leakage, which acts both as bias, by introducing an additional amount of unwanted signal in the nulled output, and as a noise through its instability. Assuming that the instrument behaves in the same way during the three successive observations of the same system, the average instrumental stellar leakage can be calibrated and only instability noise (including long-term drifts) and shot noise associated to the mean stellar leakage have to be considered in the total noise budget.

Leakage due to the OPD

Since the actual power spectral densities of instrumental perturbations are not available, the estimation of instability noise will be made assuming that the rms leakage is equal to its mean value. This assumption is supported by the results obtained on the GENIE and ALADDIN studies.[9,10] The contribution of the residual OPD error to the stellar leakage can be estimated using the following formula:[11]

$$\sigma_{\mathrm{OPD}} \leq \frac{\lambda}{\pi}\sqrt{N_i}\,, \tag{1}$$

where N_i is the required stability for the instrumental nulling ratio. This means that a stability at the level of $\sigma_{\mathrm{OPD}} \leq 1$ nm is required to cancel the star emission by a factor of 10^7 at an observing wavelength of 10 μm. Very encouraging results have been obtained recently with the adaptive nuller[12] at Jet Propulsion Laboratory with the demonstration of a broadband null of 1.2×10^{-5} over a 32% bandwidth centered in the 8-12 μm band*. Reaching a stability of 1 nm at 10 μm is still challenging but should be realistic in the near-term future.[13] This value will be considered in this study. Note however that Eq. 1 is a first order estimation and does not take into account the non-linear second order error terms which are expected to dominate the instrumental leakage.[14]

Leakage due to tip/tilt errors

The other major contributors to the stellar leakage are the wavefront errors and the intensity mismatch between the beams. Because modal filtering is used, wave front errors will be traded against intensity errors which are less severe source of instrumental leakage and add to the true intensity mismatch. In fact, true intensity errors are not expected to be a significant source of intensity mismatch and will be neglected in the following discussion. The instrumental nulling ratio N_i due to the tip-tilt error can be estimated with the following formula, taking into account the modal filtering process:[15]

$$N_i = \frac{(\pi D \sigma_\theta)^4}{64\lambda^4}\,, \tag{2}$$

*see the adaptive nuller website: *http://planetquest.jpl.nasa.gov/TPF-I/adaptiveNullerTestbed.cfm*

where D is the telescope diameter and σ_θ the residual tip/tilt error. The tip-tilt control device which will be implemented in Pegase should reach a typical residual of 30 mas rms.[2] At 10 μm and for 1-m size telescopes, a tip/tilt residual below 22 mas rms is necessary to get an SNR of 5 for an Earth located at 20 pc. The use of larger telescopes in combination with a two-stage control loop implementation will improve the pointing accuracy with respect to the Pegase nominal value (30 mas rms). Without an appropriate system study, it is difficult to give an accurate estimation of this value but a tip/tilt residual of 20 mas rms should not be too optimistic and will be assumed in this study.

3.2 Geometric stellar leakage

Because of the finite size of the target star, a residual stellar flux appears in the nulled output. This deterministic part of the stellar leakage is called the geometric leakage and is given by:[10]

$$N = \frac{\pi^2}{4}\left(\frac{b\theta_\star}{\lambda}\right)^2, \tag{3}$$

where b is the baseline length and $\theta_\star$ the stellar angular radius. At 10 μm, the contribution of geometric leakage for a Sun-like star located at 20 pc is about 125 times larger than the flux of the planet in the nulled output. To reveal the hypothetic planetary companion, the most straightforward method relies on the knowledge of the target star angular radius, which is the only unknown parameter in Eq. 3. The angular radii of Darwin target stars can be determined with a typical accuracy of 1% which gives a precision of 2% on the estimation of the stellar leakage.[16] This level of calibration is however not sufficient to get a SNR of 5 for an Earth located at 20 pc.

3.3 The thermal background and its fluctuations

Exo-zodiacal dust emission

An exo-zodiacal cloud similar to the local zodiacal disk is much brighter than an Earth-like planet with an integrated flux about 400 times larger at 10 μm. Filtered through the interferometer transmission map, the residual contribution does not exceed 30% of the total flux for a disk located at 20 pc. In addition, since several observations of the same system will be performed, the morphology of the dust cloud can be constrained and model-fitted. Taking into account both contributions, a conservative value of 10% is assumed in this study for the residual exo-zodiacal emission. To go further, fast modulation techniques have been developed in the context of Darwin/TPF but they require the use of at least 3 collectors.[1,17] More specific methods such as the split-pupil configuration and the OPD modulation have to be used for a single Bracewell.[18,19] These good candidates are reviewed by Hanot[20] and briefly discussed in section 5.3.

Local zodiacal dust emission

The local zodiacal dust cloud produces a foreground through which the interferometer will observe. Its thermal emission is estimated by the zodiacal disk model of Kelsall.[21] The model takes into account the dust in the line of sight of the interferometer located at the Lagrange point L2 and pointing in the anti solar direction. At 10 μm, the total background emission associated with the local zodiacal disk is about 2×10^{-4} times larger than the flux coming from an Earth at 20 pc and received by an 1-m telescope. This emission presents a slow variation with typical periods of 13, 27, 36, 47, 52, and 72 days[21] which are very problematic for long integration times. However, for integration times of the order of some hours, the variation of this emission can be considered as negligible[22] and remains below the residual contribution of the exo-zodiacal cloud.

Instrumental background

The thermal emission of the instrument is modelled as a grey body emission, i.e. a black-body emission multiplied by a constant emissivity factor related to the optical train. The mean value of the instrumental background can be removed with the three inclined observations and only the fluctuations remain. In order not to induce significant variations of the background emission, a high thermal stability is therefore required. To detect at 10 μm an Earth located at 20 pc (SNR of 5), the thermal stability has to be as low as 0.1 K rms for an instrument cool down to 45 K.

4. ANALYSIS FOR AN EARTH AT 20 PC

Following the previous discussion, Table 2 shows the different requirements on a 1-m Bracewell to achieve at 10 μm an SNR of 5 when observing an Earth located at 20 pc. It also shows the specifications considered for this study and the minimum size of the planet (located in the middle of the HZ) detectable with it.

	Req.	Spec.	R_{Earth}
OPD [nm]	0.47	1	2.1
Tip/tilt [mas]	22	20	0.8
Stellar radius knowledge [%]	0.8	1	3.6
Exo-zodiacal subtraction [%]	0.05	10	11.2
Instrument temperature [K]	45.3	45	1
Integration time [days]	3000		
20 surveys/year [h]	-	24	5.7
50 surveys/year [h]	-	10	7.2
100 surveys/year [h]	-	5	8.5

Table 2. First column: requirements on an 1-m Bracewell to detect an Earth-like planet located at 20 pc at 10 μm. Second column: specifications of the 1-m Bracewell considered in this study. Third column: minimum radius of the planet detectable with it. The shot and detector noises impose a lower limit on the integration time and the three last rows give the minimum radius of the planet detectable in 5, 10 or 24 hours (corresponding respectively to 100, 50 or 20 systems surveyed per year).

Due to the limited suppression of the exo-zodiacal emission, a 1-m aperture single Bracewell could not detect planets smaller than Jupiter (about 11 R_{Earth}) and orbiting in the middle of the HZ of a Sun located at 20 pc. With an appropriate method to subtract the exo-zodiacal emission, 7 Earth-radii planets would be possible to detect in 10 hours which corresponds to 50 systems surveyed per year. In 24 hours, the detection of 6 Earth-radii planets could be achieved and potentially 4 Earth-radii planets for a longer integration time. The reason is that the limitation coming from the integration time is due to the shot and detector noises which can be minimized by a sufficiently long integration time as shown by Eq. 4, giving the SNR per spectral channel:

$$\mathrm{SNR}_n = \frac{F_p \cdot t}{\sqrt{(N_s^2 + N_d^2)t} + (\sigma_i + \sigma_c + \sigma_b)t}\,, \tag{4}$$

where F_p is the planet's flux, N_s the shot noise, N_d the detector noise, σ_i the instrumental nulling noise, σ_c the instrumental calibration noise, σ_b the background fluctuation noise and t the integration time. Shot noise is dominated mainly by the stellar leakage and the contribution from the local zodiacal cloud. The detection unit features a Si:As focal plane array with a read out noise assumed to amount to 10 electrons per pixel. Dark current is supposed to be negligible by cooling down the detector to an appropriate temperature (a few K). The SNR per spectral element is represented by the solid line in Figure 2 with respect to the wavelength.

Figure 2 shows that the optimum wavelength is effectively near 10 μm and that the exo-zodiacal emission is dominant in the 5-12 μm band. In order to improve the detection capability, one can combine the spectral channels, using Eq. 5:[14]

$$\mathrm{SNR}_{\mathrm{tot}} = \left[\sum_{n_{\mathrm{indep}}} \mathrm{SNR}_n^2\right]^{1/2}\,, \tag{5}$$

where the sum is performed over the noise independent spectral channels. Determining their number would require a full analysis and is beyond the scope of this paper (some clues are given in the paper of Lay[14]). For the time being, with a spectral resolution of 60, the spectral channels are narrow at 10 μm (about 0.16 μm wide) and we will assume than only 10% of the channels are noise independent (about 1.6 μm wide). The percentage of noise independent spectral channels is denoted η in the following.

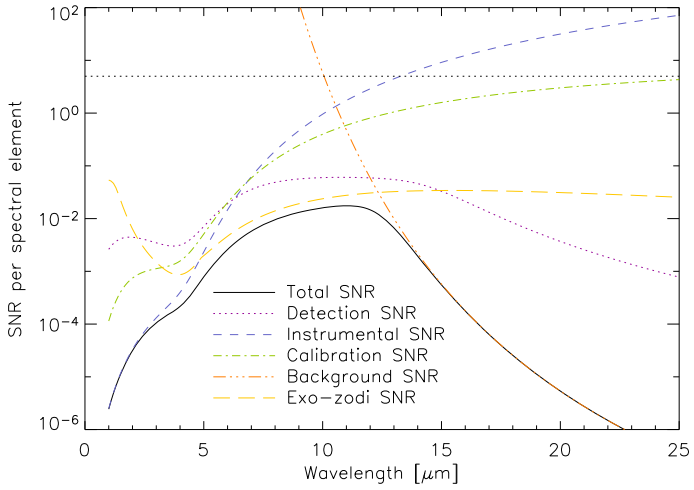

Figure 2. Individual SNRs contributing to the total SNR (solid line) for an Earth-like planet located at 20pc with respect to the wavelength, after 10 hours of integration and 1-m diameter collectors.

5. DETECTION THRESHOLD

5.1 Planet signal

In good approximation, the flux emitted by an extra-solar planet and detected by an Earth-based observer writes:[16]

$$F_p(\lambda) = A_b \frac{\pi R_\star^2}{d^2} B_\lambda(T_\star) \Phi(\Theta) \frac{R_p^2}{4a^2} + \frac{\pi R_p^2}{d^2} f(\Theta) B_\lambda(T_p)\,, \tag{6}$$

where $B_\lambda(T)$ represents the surface brightness per wavelength unit for a blackbody at temperature T, d is the distance to the target star, a the semi-major axis of the planetary orbit and R_p the planetary radius. $\Phi(\Theta)$ and $f(\Theta)$ are the phase function affecting respectively the reflected and the emitted emissions. A_b is the Bond albedo, defined as the ratio between the total reflected and total incident powers. The first term in Eq. 6 represents the reflected part of the stellar spectrum while the second term represents the thermal emission of the planet. T_p is the equilibrium temperature of the planet and can be calculated by the following formula:[16]

$$T_p = T_\star (1 - A_b)^{1/4} \left(\frac{R_\star}{2a} \right)^{1/2} . \tag{7}$$

The Bond albedo used to compute the equilibrium temperature depends on several parameters such as the chemical composition of the planet's atmosphere and surface. The results presented in this paper assume a Bond albedo of 0.306 for rocky planets by analogy to the Earth's albedo, although the surface and the potential atmosphere are probably not the same. This value has also the advantage to be intermediate among the Bond albedos of the Solar system rocky planets (0.119 for Mercur and 0.750 for Venus). For the giants planets, a value of 0.10 is assumed as derived by Baraffe[23] for hot EGPs instead of Jupiter's classical value of 0.342, since the regions close to the star will mostly be investigated. Finally, following the simulations of core accretion reported by Ida,[24] the limit between gaseous and rocky planets will be considered around 15 Earth masses.

5.2 Results for a Sun at 20 pc

The purpose of this section is to extend the analysis presented in the previous sections by considering planets with different orbits. This general approach requires numerical simulations which have been done by adapting a top-level performance prediction tool developed by O. Absil for Pegase[16] and using several routines from the Darwin science simulator, DARWINsim.[25] A crucial parameter in the performance assessment is the distance

between the planet and its parent star. In accordance with Eq. 6 and Eq. 7, the closer the planet is to its parent star the brighter it is, which improves also the contrast with the background sources. The optimum wavelength is also modified since the planet becomes hotter. Optimizing the wavelength in agreement with the semi-major axis of the planet's orbit, the detection threshold, i.e. the minimum size of the planet detectable, is represented in Figure 3 for a Sun-like star located at 20 pc (the detection threshold for detection is set at a global SNR of 5). For practical reasons (it is difficult to cover the full wavelength range with one set of glasses and single-mode spatial filters), the width of the total wavelength band has been set to 4 μm.

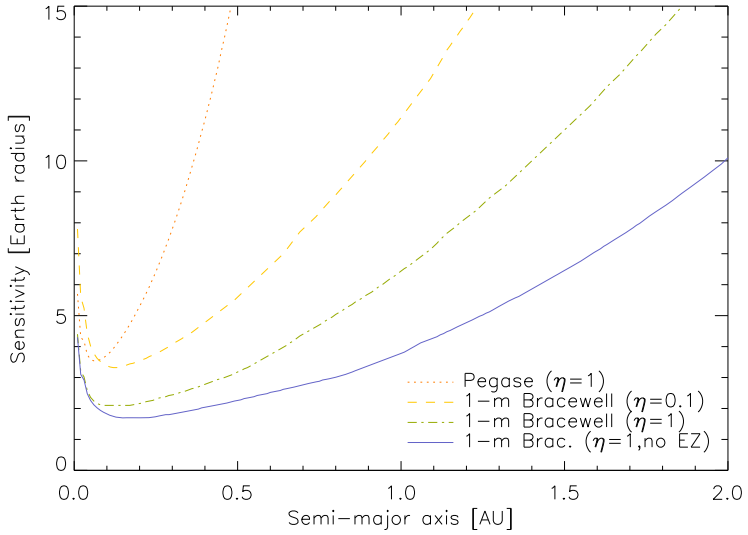

Figure 3. Sensitivity of Pegase (dotted), 1-m Bracewell with respectively 10% (dashed) and 100% (dash-dot) independent spectral channels and without exo-zodiacal cloud (solid) for 10 hours integration time and observing a Sun-like star located at 20 pc. For each semi-major axis, the sensitivity is computed in the optimum 4-μm wide wavelength band.

Each curve represents the detection threshold for an integration time of 10 hours (about 50 surveys per year). The dotted curve shows the sensitivity domain of Pegase assuming a perfect combination of the spectral channels (η=1) in the 2.5-5 μm wavelength range. The best sensitivity arises for planets located very close to the star with 4 Earth-radii planets detectable at about 0.05 AU and Jupiter-size planets detectable till 0.4 AU. Including the exo-zodiacal emission, the dash-dot curve shows the improvement of the capabilities by considering a 1-m Bracewell working at 10 μm. Jupiter-size planets are detectable till about 1.6 AU while in the middle of the HZ, Neptune-size planets could be detected. Rocky planets are detectable in the close vicinity of the star ($\sim$ 0.1 AU). Going further, the solid curve shows the potential of the concept on the basis of 10 hours integration time, assuming a perfect subtraction of the exo-zodiacal emission in addition to the perfect combination of the spectral channels ($\eta = 1$). Small Neptune-like planets orbiting around a Sun located at 20 pc are detectable within 10 hours in the middle of the HZ. Shot noise is now the limiting factor and a longer integration time is required to improve the sensitivity.

Finally, a more realistic assessment of the capabilities is given by the dashed curve, plotted considering that only 10% of the spectral channels are independent. This curve gives also an approximation of the minimum size of planets for which spectroscopy can be performed. As expected from the previous section, the performance would be limited to Jupiter-size planets in the middle of the HZ.

5.3 Removing the exo-zodiacal emission

As shown by Table 2, the residual of the exo-zodiacal emission is the main limiting factor. The level of performance could be considerably improved (4 Earth-radii instead of Jupiter-size planets detectable) by removing it from the nulled output. The basic method to modulate the planet signal against the exo-zodiacal emission is to

rotate the interferometer along the line of sight but this can generally not be performed sufficiently fast and the planet signal is easily corrupted by long term drifts. Fast modulation can be implemented with the split-pupil configuration[18] or with OPD modulation.[19] In the case of split-pupil, both telescopes are divided in two parts, creating two independent Bracewell interferometers. The outputs of these two interferometers are then combined with a time-varying phase shift which allows to remove all point-symmetric emissions (in the ideal case). The division of the pupil introduces however significant additional complexity.[16] The principle of OPD modulation is to sweep back and forth the dark fringe of the transmission map by modulating the pathlength in one arm of the interferometer.[19] In that manner, all centro-symmetric sources are modulated at twice the modulation frequency. If the baseline length is chosen such as the planet locates on a grey fringe, the planet signal will be modulated at the modulation frequency and can be retrieved by using synchronous coherent demodulation. In principle, OPD modulation could be implemented at little increase of the system complexity. For both methods, only 50% of the planet signal is generally retrieved which reduces the actual performance. In his master thesis, Hanot shows that the split-pupil technique leads to better SNRs than the OPD modulation but remains pessimistic about the ability of both methods to reveal Earth-like planets in presence of instrumental errors and typical asymmetries of the cloud.[20] A full investigation of these techniques will be the object of an upcoming paper.

5.4 Study of the habitable zone: application to the Darwin catalogue

The application to the Darwin catalogue[7,8] allows to extend the study to stars of different spectral types. The prime targets of the catalogue, i.e. the single star systems, amount to 628 stars (43 F, 100 G, 244 K and 241 M stars), in our close neighbouroud ($\leq$25 pc). Around each of these stars, a planet is supposed to be present in the middle of the HZ. Expressed in AU, the position of the HZ is given in good approximation by the following formula:[26]

$$r_{\mathrm{HZ}} = \left(\frac{T_\star}{T_\odot}\right)^2 \frac{R_\star}{R_\odot}\,, \tag{8}$$

which corresponds to 2.3, 1.3, 0.7 and 0.2 AU for F0V, G0V, K0V and M0V stars respectively. To estimate the performance of a 1-m Bracewell, the integration time required to reach an SNR of 5 for each target of the Darwin catalogue is computed. The SNRs are computed with the assumption that there is no exo-zodiacal emission so that the full potential of methods described in section 5.3 can be reached. The spectral channels are combined in the optimum 4-μm wide wavelength range with η=1. Note that according to Eq. 4, only the part of the SNR due to the shot and detector noises can be improved by increasing the integration time. Targets for which $\sigma_i + \sigma_c + \sigma_b > 5F_p$ cannot reach an SNR of 5 and are thus not considered. The integration times of the remaining targets are then sorted by increasing values and added till the sum reaches the mission lifetime. The results are presented in Figure 4 which indicates the number of stars around which a planet of a given radius can be detected during the mission lifetime.

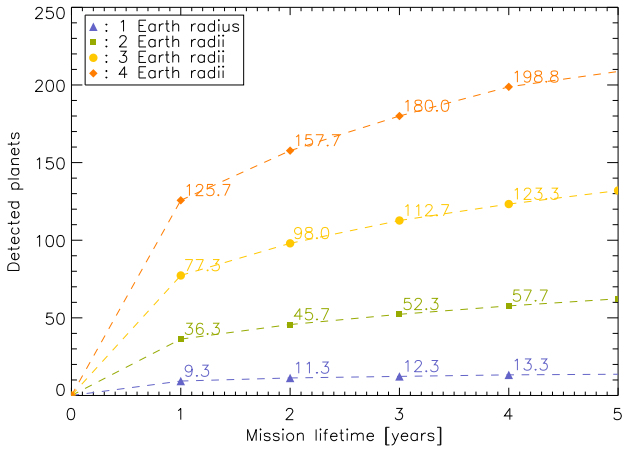

Figure 4. Number of stars around which a planet of a given radius can be detected with respect to the mission lifetime.

During the first year of the mission, about 9 Earth-like or 36 two Earth-radii planets could be detected. A planet is considered detected when a total SNR of 5 is reached for at least one of the three observations for each position on the orbit. The gain by increasing the mission lifetime is not significative, particularly for the smallest planets. These detected planets are mainly around M stars as illustrated in Figure 5, showing the total integrated SNR for a rocky planet of 2 Earth radii and an integration time of 10 hours.

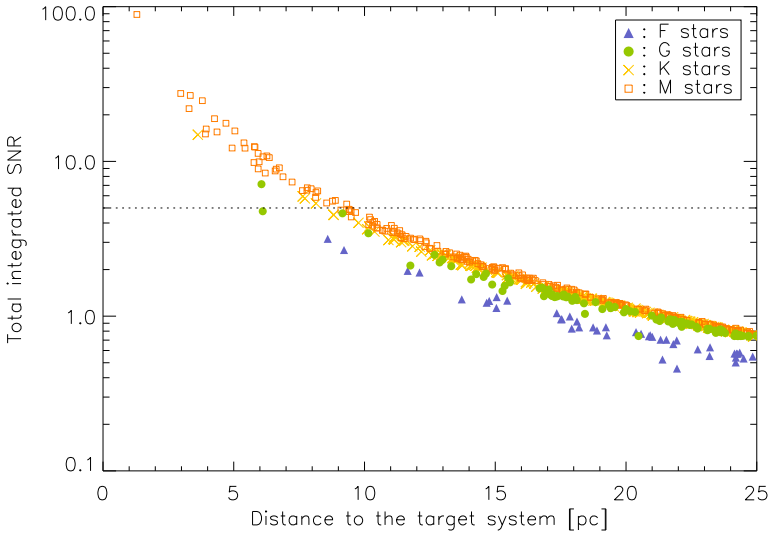

Figure 5. Total SNR for a two Earth-radii planet orbiting in the middle of the HZ of Darwin targets and for an integration time of 10 hours (assuming no exo-zodiacal cloud).

While an SNR of 5 is out of reach for F stars, all M-star planets within ∼10 pc could be detected as well as several K-star and 1 G-star planets. M stars have been identified as relevant targets for future HZ planet search programs[27] and would therefore be very good candidates to survey. Note also that all 2 Earth-radii planets located beyond 10 pc would not be detectable. In conclusion, the Bracewell interferometer presented in this study would be a convenient instrument to search M stars located within 10 pc for planets of 2 Earth-radii. Some K and G stars might also be added to the target list.

5.5 Application to known extra-solar planets

Whereas 246 extra-solar planets have been discovered so far[†], only 61 of them are in our close vicinity (closer than 25 pc). Considering a sample of these 61 favorable targets, Table 3 gives the SNRs achievable by Pegase, the classic Bracewell with 1-m diameter telescopes including the noise contribution of the exo-zodiacal emission (1-m Bracewell) or not (1-m+ configuration), in the optimum spectral element and for an integration time of 10 hours. By definition, the 1-m+ configuration gives upper limits on the actual SNRs that we could expect from the split-pupil configuration and the OPD modulation technique.

Defining the good candidates for spectroscopy as those for which an SNR of 5 can be achieved in the optimum spectral element, Pegase could perform spectroscopy on 9 of the 61 targets (about 15%), including 3 planets in the hot regime (closer than 0.1 AU from its parent star, see for instance τ *Boo b* and *51 Peg b* in Table 3) and 6 cooler planets like *70 Vir b* and *55 Cnc b*. These results suggest that the Pegase target list could be extended to a significant number of planets outside the hot regime (see the master thesis of Defrère[28] for the SNRs of the full target list).

[†]see *http://exoplanet.eu/catalog.php* or *http://exoplanets.org/* for an up-to-date list.

	Star			Planet			SNR		
	spectral type	dist. [pc]	eclipt. lat.	s-maj. axis [AU]	Min. mass [M_{Jup}]	T_{eq} [K]	Peg.	1-m	1-m+
Ups And b	F8V	13.5	28.9	0.06	0.69	1570	2	3	4
Ups And c	F8V	13.5	28.9	0.83	1.98	420	2	18	41
Ups And d	F8V	13.5	28.9	2.53	3.95	240	0	4	14
Tau Boo b	F7V	15.6	26.5	0.05	3.90	1270	36	79	85
55 Cnc b	G8V	13.4	10.4	0.12	0.78	560	13	47	76
55 Cnc c	G8V	13.4	10.4	0.24	0.22	390	1	10	22
55 Cnc d	G8V	13.4	10.4	5.26	4.00	80	0	0	0
55 Cnc e	G8V	13.4	10.4	0.04	0.05	980	3	7	8
70 Vir b	G5V	18.1	21.3	0.48	7.44	500	6	39	59
51 Peg b	G2V	15.4	25.2	0.05	0.47	1290	5	8	9
HD 69830 b	K0V	12.6	-0.55	0.08	0.03	830	2	4	5
HD 69830 c	K0V	12.6	-0.55	0.19	0.04	540	1	5	7
HD 69830 d	K0V	12.6	-0.55	0.63	0.06	290	0	2	3
GI 581 b	M3	6.26	10.26	0.04	0.05	675	3	13	18
GI 581 c	M3	6.26	10.26	0.07	0.02	510	0	4	7
GI 581 d	M3	6.26	10.26	0.25	0.02	205	0	0	1
Gliese 876 b	M4V	4.7	-6.6	0.21	1.93	220	0	18	47
Gliese 876 c	M4V	4.7	-6.6	0.13	0.56	270	1	22	53
Gliese 876 d	M4V	4.7	-6.6	0.02	0.02	680	3	7	9

Table 3. Sample of known extra-solar planets located within 25 pc from our solar system given with the SNRs achievable by Pegase, the classic 1-m Bracewell and the 1-m Bracewell without exo-zodiacal cloud (1-m+). The SNRs are given per spectral element at the optimum wavelength and for an integration time of 10 hours.

The use of the 1-m classic Bracewell allows to go up to 27 of the 61 targets (about 45%), including 5 of the 9 remaining planets in the hot regime (see for instance *55 Cnc e*, the hot-Neptune *Gliese 876 d* and *GI 581 b* in Table 3). Finally, with the 1-m+ configuration, spectroscopy can be performed on 38 targets, which represents about 60% of known extra-solar planets within 25 pc. The achievable SNRs can also be much better as illustrated by the *Ups And* system. More interesting, a SNR of 7 could be achieved in 10 hours on the recently discovered planet orbiting close to the HZ of its star, *GI 581 c*. Since the values given for the 1-m+ configuration are only upper limits, a realistic assessment of the capabilities of split-pupil/OPD modulation techniques would be the ability to do spectroscopy on 45 to 60% of all known extra-solar planets within 25 pc.

6. SUMMARY AND CONCLUSION

Infrared nulling interferometry is the core technique of several projects dedicated to the study of extra-solar planets. The most promising in terms of scientific return is undoubtedly the Darwin/TPF missions which should enable the spectroscopy of Earth-like planets in our close vicinity (within 30 pc). The achievement of this objective requires a complex scheme of nulling using at least 3 beam collectors. In this paper, we assess the capabilities of a simpler version of Darwin/TPF, which apart from consisting in only two 1-m diameter telescopes, presents Darwin-like specifications. The study is based on the infrared Bracewell interferometer Pegase, aimed at studying known hot Jupiters located within 150 pc. The main challenge to detect an Earth-like planet is the exo-zodiacal cloud which is 400 times brighter than an Earth located at 20 pc (at 10 μm). Specific methods to mitigate the exo-zodiacal emission in the case of Bracewell interferometers (viz. OPD modulation and split-pupil configuration) are addressed and results are given separately from those of the classic scheme (without the implementation of these methods).

Around a Sun located at 20 pc, the Bracewell interferometer presented in this study could detect in one year about 50 Neptune-like planets ($M \sim 0.05\ M_{Jup}$) orbiting in the middle of the habitable zone. The application to the Darwin catalogue has shown that smaller planets could be detected, with about 40 two Earth-radii planets detectable the first year of the mission. In particular, this "upgraded" Pegase or "down-scoped" Darwin would

be a very efficient instrument to search M stars located within 10 pc for planets of 2 Earth-radii. Finally, 45% of the 61 known extra-solar planets in the close vicinity of the solar system (within 25 pc) could be surveyed for spectroscopy instead of 15% with Pegase. This value reaches 60% if the exo-zodiacal emission is efficiently subtracted. These preliminary results need to be confirmed by detailed simulations, taking particularly into account the continuous rotation of the array and second order effects of the instability noise.

ACKNOWLEDGMENTS

The authors would like to thank R. den Hartog for his expert advice. Thanks also to J. Surdej, P. Riaud, D. Mawet and A. Magette for their contribution to the work presented in this paper. The first author acknowledges the financial support from the Belgian National Science Foundation ("FRIA").

REFERENCES

1. R. N. Bracewell, "Detecting nonsolar planets by spinning infrared interferometer," *Nature* **274**, pp. 780–+, Aug. 1978.
2. J. M. Le Duigou, M. Ollivier, A. Léger, F. Cassaing, B. Sorrente, B. Fleury, G. Rousset, O. Absil, D. Mourard, Y. Rabbia, L. Escarrat, F. Malbet, D. Rouan, R. Clédassou, M. Delpech, P. Duchon, B. Meyssignac, P.-Y. Guidotti, and N. Gorius, "Pegase: a space-based nulling interferometer," *Presented at the Society of Photo-Optical Instrumentation Engineers (SPIE) Conference* **6265**, July 2006.
3. R. K. Barry, W. C. Danchi, L. D. Deming, L. J. Richardson, M. J. Kuchner, S. Seager, B. J. Frey, A. J. Martino, K. A. Lee, M. Zuray, J. Rajagopal, T. T. Hyde, R. Millan-Gabete, J. D. Monnier, R. J. Allen, and W. A. Traub, "The Fourier-Kelvin stellar interferometer: a low-complexity low-cost space mission for high-resolution astronomy and direct exoplanet detection," *Presented at the Society of Photo-Optical Instrumentation Engineers (SPIE) Conference* **6265**, July 2006.
4. C. V. M. Fridlund, L. d'Arcio, R. den Hartog, and A. Karlsson, "Status and recent progress of the Darwin mission in the Cosmic Vision program," *Presented at the Society of Photo-Optical Instrumentation Engineers (SPIE) Conference* **6268**, July 2006.
5. C. Beichman, P. Lawson, O. Lay, A. Ahmed, S. Unwin, and K. Johnston, "Status of the terrestrial planet finder interferometer (TPF-I)," *Presented at the Society of Photo-Optical Instrumentation Engineers (SPIE) Conference* **6268**, July 2006.
6. L. Kaltenegger, W. A. Traub, and K. W. Jucks, "Spectral Evolution of an Earth-like Planet," *ApJ* **658**, pp. 598–616, Mar. 2007.
7. A. Stankov, "All sky target stars catalogue - no limit in ecliptic latitude," 2005.
8. L. Kaltenegger, C. Eiroa, A. Stankov, and M. Fridlund, "Nearby Stellar sample for the search for terrestrial planets. Target star catalogue for the Darwin Mission Study," *A&A* , 2007 (submitted).
9. O. Absil, V. Coudé du Foresto, M. Barillot, and M. Swain, "Nulling interferometry: comparison of performances between Antarctica and other ground-based sites," *A&A* , 2007 (submitted).
10. O. Absil, R. den Hartog, P. Gondoin, P. Fabry, R. Wilhelm, P. Gitton, and F. Puech, "Performance study of ground-based infrared Bracewell interferometers. Application to the detection of exozodiacal dust disks with GENIE," *A&A* **448**, pp. 787–800, Mar. 2006.
11. M. Ollivier, *Contribution a la recherche d'exoplanetes coronographie interfrentielle pour la mission Darwin*. PhD thesis, Universit Paris-Sud, Paris, France, 1999.
12. R. D. Peters, O. P. Lay, A. Hirai, and M. Jeganathan, "Adaptive nulling for the Terrestrial Planet Finder Interferometer," *Presented at the Society of Photo-Optical Instrumentation Engineers (SPIE) Conference* **6268**, July 2006.
13. P. Lawson, "Results of Laboratory Experiments Kin Nulling Interferometry (1998-2006)," in *the proceedings of the TPF/Darwin 2006 conference*, 2006.
14. O. P. Lay, "Systematic Errors in Nulling Interferometers," *Appl. Opt.* **43**, pp. 6100–6123, Nov. 2004.
15. B. Mennesson, M. Ollivier, and C. Ruilier, "Use of single-mode waveguides to correct the optical defects of a nulling interferometer," *Journal of the Optical Society of America A* **19**, pp. 596–602, Mar. 2002.

16. O. Absil, *Astophysical studies of extrasolar planetary systems using infrared interferometric techniques*. PhD thesis, Liège University, Liège, Belgium, 2006.
17. O. Absil, A. Karlsson, and L. Kaltenegger, "Inherent modulation: a fast chopping method for nulling interferometry," in *Interferometry in Space. Proceedings of the SPIE, Volume 4852*, M. Shao, ed., pp. 431–442, Feb. 2003.
18. E. Serabyn, "An overview of the Keck Interferometer Nuller," in *ESA SP-539: Earths: DARWIN/TPF and the Search for Extrasolar Terrestrial Planets*, M. Fridlund, T. Henning, and H. Lacoste, eds., pp. 91–98, Oct. 2003.
19. L. L. D'Arcio, A. L. Karlsson, and P. A. Gondoin, "Use of OPD modulation techniques in nulling interferometry," in *New Frontiers in Stellar Interferometry, Proceedings of SPIE Volume 5491*, W. A. Traub, ed., pp. 851–+, Oct. 2004.
20. C. Hanot, "Investigation of a down scoped version of the darwin mission," Master's thesis, Liège University, Liège, Belgium, 2005.
21. T. Kelsall, J. L. Weiland, B. A. Franz, W. T. Reach, R. G. Arendt, E. Dwek, H. T. Freudenreich, M. G. Hauser, S. H. Moseley, N. P. Odegard, R. F. Silverberg, and E. L. Wright, "The COBE Diffuse Infrared Background Experiment Search for the Cosmic Infrared Background. II. Model of the Interplanetary Dust Cloud," *ApJ* **508**, pp. 44–73, Nov. 1998.
22. C. Leinert, S. Bowyer, L. K. Haikala, M. S. Hanner, M. G. Hauser, A.-C. Levasseur-Regourd, I. Mann, K. Mattila, W. T. Reach, W. Schlosser, H. J. Staude, G. N. Toller, J. L. Weiland, J. L. Weinberg, and A. N. Witt, "The 1997 reference of diffuse night sky brightness," *A&AS* **127**, pp. 1–99, Jan. 1998.
23. I. Baraffe, G. Chabrier, T. S. Barman, F. Allard, and P. H. Hauschildt, "Evolutionary models for cool brown dwarfs and extrasolar giant planets. The case of HD 209458," *A&A* **402**, pp. 701–712, May 2003.
24. S. Ida and D. N. C. Lin, "Toward a Deterministic Model of Planetary Formation. I. A Desert in the Mass and Semimajor Axis Distributions of Extrasolar Planets," *Astrophysical Journal of Physics* **604**, pp. 388–413, Mar. 2004.
25. R. den Hartog, "The DARWINsim science simulator," Tech. Rep. Issue 1, ESA (SCI-A/297), May 2005.
26. J. F. Kasting, D. P. Whitmire, and R. T. Reynolds, "Habitable Zones around Main Sequence Stars," *Icarus* **101**, pp. 108–128, Jan. 1993.
27. J. Scalo, L. Kaltenegger, A. G. Segura, M. Fridlund, I. Ribas, Y. N. Kulikov, J. L. Grenfell, H. Rauer, P. Odert, M. Leitzinger, F. Selsis, M. L. Khodachenko, C. Eiroa, J. Kasting, and H. Lammer, "M Stars as Targets for Terrestrial Exoplanet Searches And Biosignature Detection," *Astrobiology* **7**, pp. 85–166, Feb. 2007.
28. D. Defrère, "Performance study of spaced-based infrared nulling interferometers," Master's thesis, Liège University, Liège, Belgium, 2007.

3.5.4 Complementary results

In the article presented in the previous section, the results are given for a representative sample of known extrasolar planets. In order to provide a more complete performance overview, Table 3.3 hereafter lists (by spectral type) all the extrasolar planets known within 25 pc and gives the expected SNRs at the optimum wavelength and for the different instrumental configurations. Note that several targets located beyond 25 pc could also be surveyed by Pegase and Pegasus (as shown by Absil 2006).

	Star			Planet			SNR		
	spectral type	dist. [pc]	eclipt. lat.	s-maj. axis [AU]	Min. mass [M_{Jup}]	T_{eq} [K]	Peg.	1-m	1-m+
HD 33564 b	F6 V	21.0	-	1.10	9.10	294	1	13	45
Tau Boo b	F7V	15.0	7.55°	0.05	3.90	1267	36	79	85
Ups And b	F8V	13.5	-34.3°	0.06	0.69	1567	2	3	4
Ups And c	F8V	13.5	15.1°	0.83	1.98	418	2	18	41
Ups And d	F8V	13.5	-44.7°	2.53	3.95	239	0	4	14
HD 10647 b	F8V	17.4	35.4°	2.10	0.91	205	0	1	2
HD 19994 b	F8V	22.4	24.9°	1.30	2.00	222	0	1	4
HD 210277 b	G0	21.3	-54.7°	1.10	1.23	268	0	3	7
47 Uma b	G0V	13.7	-30.7°	2.11	2.60	212	0	2	7
47 Uma c	G0V	13.7	-47.5°	7.73	1.34	111	0	0	0
HR 810 b	G0V	15.5	-61.0°	0.91	1.94	402	1	17	30
HD 39091 b	G1IV	20.6	-76.0°	3.29	10.35	221	0	4	9
HD 142 b	G1IV	20.6	-44.5°	0.98	1.00	272	0	3	8
51 Peg b	G2IV	15.4	-19.8°	0.05	0.47	1286	5	8	9
rho CrB b	G2V	17.4	43.3°	0.22	1.04	680	7	20	31
HD 160691 e	G3IV-V	15.3	-28.4°	0.92	0.52	311	0	5	11
HD 195019 b	G3IV-V	20.0	36.6°	0.14	3.70	865	15	43	49
HD 147513 b	G3/G5V	12.9	-43.6°	1.26	1.00	239	0	4	9
HD 160691 d	G3V	15.3	-49.3°	0.09	0.04	994	1	2	3
HD 160691 b	G3V	15.3	47.2°	1.50	1.67	243	0	4	10
HD 160691 c	G3V	15.3	56.9°	4.17	3.10	146	0	0	0
70 Vir b	G4V	22.0	57.9°	0.48	7.44	502	6	39	59
HD 4308 b	G5V	21.9	-60.2°	0.11	0.05	747	1	5	6
HD 134987 b	G V	25.0	-7.09°	0.78	1.58	324	0	9	14
16 Cyg b	G5V	21.4	7.56°	1.67	1.68	269	0	4	8
HD 190360 b	G6IV	15.9	48.9°	3.92	1.50	203	0	1	2
HD 190360 c	G6IV	15.9	48.9°	0.13	0.06	1125	0	1	1
GJ 3021 b	G6V	17.6	-43.1°	0.49	3.32	363	2	18	60
55 Cnc b	G8V	13.4	10.4°	0.12	0.78	563	13	47	76
55 Cnc c	G8V	13.4	10.4°	0.24	0.22	389	1	10	22
55 Cnc d	G8V	13.4	10.4°	5.26	3.92	83	0	0	0
55 Cnc e	G8V	13.4	10.4°	0.04	0.05	979	3	7	8
HD 114783 b	K0	22.0	-20.8°	1.20	0.99	199	0	1	1
HD 128311 b	K0	16.6	-28.3°	1.01	2.18	210	0	3	5
HD 128311 c	K0	16.6	-9.18°	1.76	3.21	159	0	1	1
HD 62509 b	K0IIIb	10.3	-	1.69	2.90	500	0	2	2
HD 3651 b	K0V	11.1	-19.6°	0.28	0.20	439	1	12	20
Gl 86 b	K0V	10.9	-53.3°	0.11	4.01	679	34	52	139
14 Her b	K0V	18.1	31.7°	2.80	4.64	141	0	0	0
HD 69830b	K0V	12.6	4.72°	0.08	0.03	833	2	4	5
HD 69830c	K0V	12.6	4.72°	0.19	0.04	541	1	5	7

	Star			Planet			SNR		
	spectral type	dist. [pc]	eclipt. lat.	s-maj. axis [AU]	Min. mass [M_{Jup}]	T_{eq} [K]	Peg.	1-m	1-m+
HD 69830 d	K0V	12.6	4.72°	0.63	0.06	294	0	2	3
HD 164922 b	K0V	21.9	-	2.11	0.36	165	0	0	0
HD 189733 b	K1-K2	19.3	-	0.03	1.15	1143	12	28	30
HD 27442 b	K2 IV	18.1	-76.3°	1.18	1.28	528	0	2	2
Gam Cep b	K2V	11.8	64.7°	2.04	1.60	393	0	3	3
Eps Eri b	K2V	3.2	-5.95°	3.39	1.55	123	0	1	1
HD 99492 b	K2V	18.0	33.0°	0.12	0.11	594	2	9	11
HD 192263 b	K2V	19.9	4.72°	0.15	0.72	522	6	22	37
GJ 674 b	M2.5	4.5	-	0.04	0.04	492	3	17	23
GJ 436 b	M3	10.2	-23.5°	0.03	0.07	619	3	8	13
Gl 581 b	M3	6.3	-	0.04	0.05	506	3	13	18
Gl 581 c	M3	6.3	-	0.07	0.02	379	0	4	7
Gl 581 d	M3	6.3	-	0.25	0.02	205	0	0	1
GJ 849 b	M3.5	8.8	-	2.35	0.82	78	0	0	0
GJ 317 b	M3.5	9.2	-	0.95	1.20	105	0	0	0
GJ 317 c	M3.5	9.2	-	0.95	0.83	105	0	0	0
Gliese 876 b	M4V	4.7	-70.5°	0.21	1.94	216	0	18	47
Gliese 876 c	M4V	4.7	-63.6°	0.13	0.56	274	1	22	53
Gliese 876 d	M4V	4.7	-37.1°	0.02	0.02	684	3	7	9
SCR 1845 b	M8.5 V	3.9	-	4.50	8.50	33	0	0	0

Table 3.3: Known extrasolar planets located within 25 pc from the solar system given with the SNRs achievable by Pegase, Pegasus ("1-m" row) and Pegasus in the absence of exozodiacal clouds ("1-m+" row). The SNRs are given per spectral element at the optimum wavelength and for an integration time of 10 hours.

The results of Table 3.3 are discussed at the point 5.5 in the article presented in section 3.5.3. In order to have a global overview of the capabilities of each instrument, Figure 3.13 gives the SNR achievable by Pegase (left) and Pegasus (right) with respect to the minimum mass and the semi-major axis of each planet. Pegase (resp. Pegasus) could achieve SNRs larger than 10 for 5 targets (resp. 15). Unlike Pegase, Pegasus could also achieve SNRs larger than 1 for most targets.

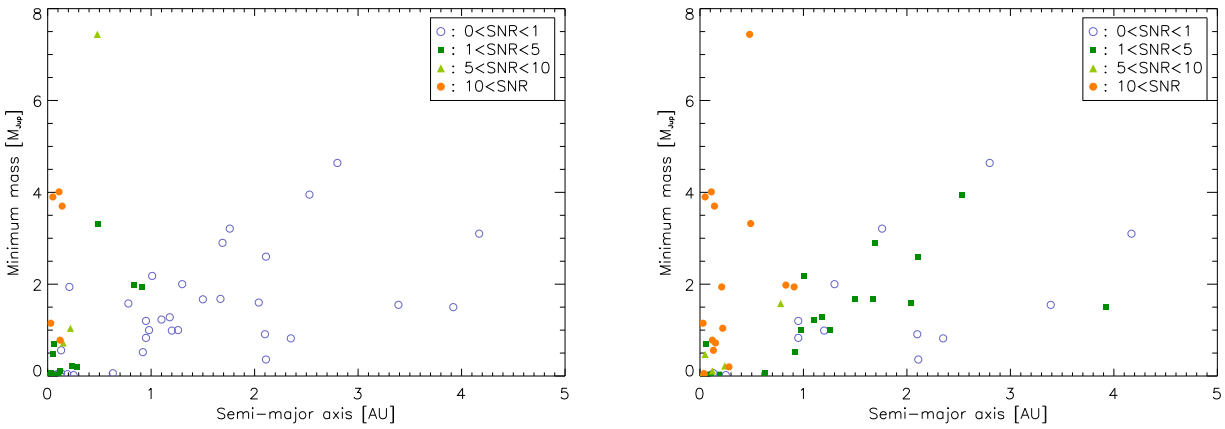

Figure 3.13: Expected SNR at the optimum wavelength for Pegase (left) and Pegasus (right), given with respect to the planetary semi-major axes and minimum masses.

4

Darwin: the European life-finding mission

Contents

Abstract. With its NASA's counterpart (TPF), Darwin is probably the most beautiful application of nulling interferometry. Using 4 telescopes observing in the infrared, Darwin is aimed at the detection and characterisation of Earth-like extrasolar planets, with the search for life as a cornerstone. This scientific objective corresponds exactly to the first priority of the theme 1 in the ESA Cosmic Vision science plan. Based on the recent convergence between ESA and NASA on the mission architecture (Emma X-array), this chapter presents the simulated performance of Darwin, which benefits from a joint effort with NASA/JPL. These performance predictions have been used as input values for the ESA's Cosmic Vision proposal (2007).

4.1 The Darwin mission

4.1.1 Scientific objectives

The main scientific objectives of Darwin are detecting rocky planets similar to Earth and performing the spectroscopic analysis of their atmosphere at mid-infrared wavelengths (6 - 20 μm, Fridlund *et al.* 2006). In addition to presenting the most advantageous star/planet contrast, this wavelength range holds several spectral features relevant for the search of biological activity (CO_2, H_2O, CH_4, O_3, see section 1.1.4 and Figure 1.4). The observing scenario of Darwin consists in two phases, detection and spectral characterisation, whose relative duration can be adjusted to optimise the scientific return. During the detection phase of the mission (nominally 2 years), Darwin will examine nearby stars for evidence of terrestrial planets. A duration of 3 years is foreseen for the spectroscopy phase, for a total nominal mission lifetime of 5 years. An extension to 10 years is possible and will depend on the results obtained

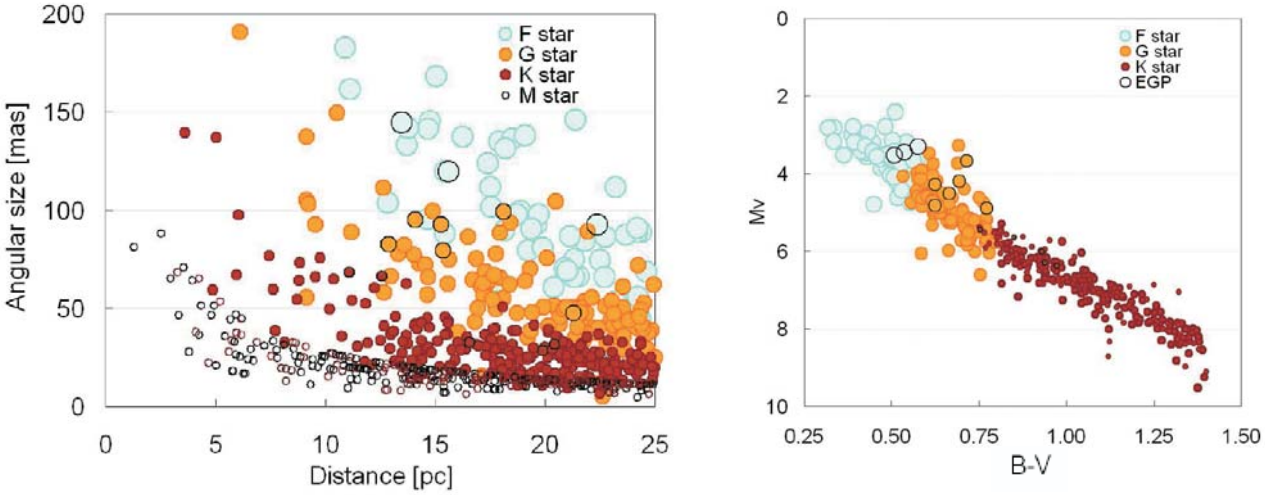

Figure 4.1: Size of the habitable zone for the different spectral types of Darwin target (left), and color-magnitude diagram for the same stars (right). Dark circles indicate the stars that host EGPs (Figures from Kaltenegger *et al.* 2007a).

during the 5 first years. Such an extension could be valuable to observe more M stars, only 10% of the baseline time is attributed to them, search for big planets around a significantly larger sample of stars, and additional measurements on the most interesting targets already studied.

The Darwin target star list has been generated from the Hipparcos catalogue, considering several criteria: the distance (< 25 pc), the brightness (< 12 V-mag), the spectral type (F, G , K, M main sequence stars), and the multiplicity (no companions within $1''$). The corresponding star catalogue contains 758 targets, including 54 F stars, 114 G stars, 240 K stars and 350 M stars (Kaltenegger *et al.* 2007a). Some features of these stars are shown in Figure 4.1. The survey of the Darwin stars and the possible detection of terrestrial planets will start a new era of comparative planetology, especially by studying the relationship between habitability and stellar characteristics (e.g. spectral type, metallicity, age), planetary system characteristics (e.g. orbit), and atmospheric composition.

In addition to its primary goals, Darwin could provide a wealth of information on the following topics:

- **Planetary formation**. Darwin will be able to spatially resolve structures below 1 AU in nearby star forming regions, allowing to witness directly the formation of terrestrial planets in the thermal infrared (see Figure 4.2 for an overview of the imaging capabilities of Darwin with respect to JWST). In particular, Darwin will be very efficient to study gaps and determine if the clearing is due to the influence of already-formed giant planets or to another mechanisms (e.g. viscous evolution, photo-evaporation).

- **Formation, evolution, and growth of massive black holes**. Darwin will be able to probe the immediate environments of very different black holes (BH), ranging from very massive BH in different types of Active Galactic Nuclei (AGN), to the massive black hole at the centre of the Milky Way, down to BH associated with stellar remnants.

- **Galaxy formation and evolution**. With its high resolution, Darwin will be able to measure the detailed spatial structure of very distant galaxies, which places essential constraints on galaxy formation models.

The general astrophysics programme, if adopted, will comprise 10% to 20% of the mission time. The primary science time allocation would then be reduced accordingly, with limited impact on its outcome.

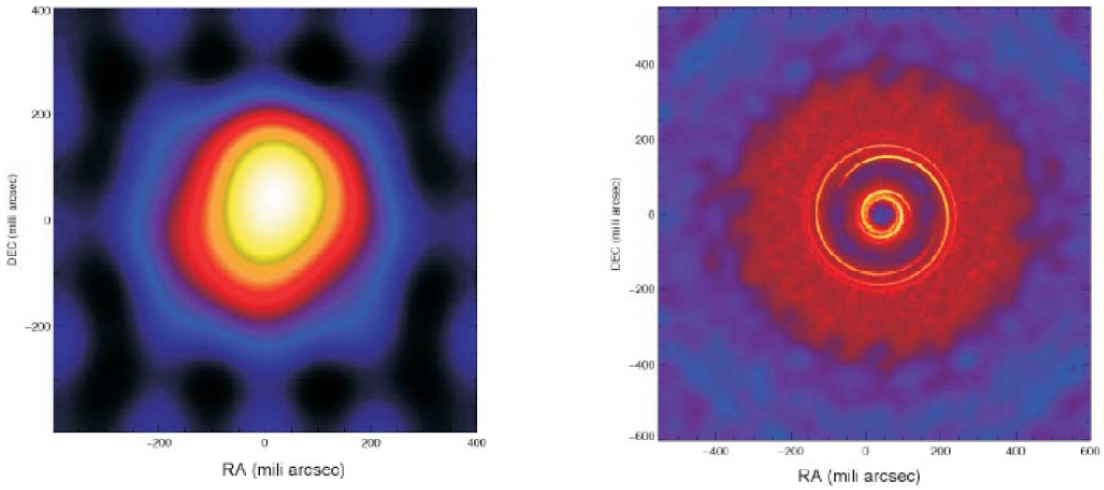

Figure 4.2: Simulation of a hot accretion disc in Taurus (140 pc) as seen by JWST (left) and Darwin in its imaging mode (Right). Simulated JWST and Darwin images are based on scaled models by D'Angelo *et al.* (2006) for the formation of a planet of one Jupiter mass at 5.2 AU, orbiting a solar type star. The most prominent features in the model are a gap along the planet's path and spiral wave patterns emanating from the Lagrangian point, only visible with Darwin (courtesy C. de Vries).

4.1.2 Instrumental concept

Considerable efforts have been carried out the past decade by both ESA[10] and NASA to define a mission design that provides excellent scientific performance while minimizing cost and technical risks. After the investigations of several interferometer architectures, these efforts culminated in 2005-2006 with two parallel assessment studies of the Darwin mission, carried out by EADS Astrium and Alcatel-Alenia Space. Two array architectures have been thoroughly investigated during these industrial studies: the four-telescope X-array and the Three-Telescope Nuller (TTN, Karlsson *et al.* 2004). These studies included the launch requirements, payload spacecraft, and the ground segment during which the actual mission science would be executed. Almost simultaneously, NASA/JPL initiated a similar study for the Terrestrial Planet Finder Interferometer (TPF-I). These efforts on both sides of the Atlantic have finally resulted in a convergence and consensus on mission architecture, the so-called non-coplanar or Emma-type X-array (represented in Figure 4.3). The baseline design consists in four 2-m aperture collector spacecraft, flying in rectangular formation and feeding light to the beam combiner spacecraft located approximately 1200 m above the array. This arrangement makes available baselines up to 170 m for nulling measurements and up to 500 m for the general astrophysics programme (constructive imaging). Note that the size of the collecting apertures has not yet been fixed and will depend mainly on the final cost of the mission.

The optical layout of the X-array configuration separates the nulling and imaging functions, the shortest baselines being used for nulling while the longest for imaging. This configuration has the advantage to allow optimal tuning of the shorter dimension of the array for starlight suppression while keeping a relatively longer dimension to resolve the planet. The X-array design is also appropriate to consider techniques for removing instability noise, a key limit to the sensitivity of Darwin (see section 4.2). Beam combination takes place on a serie of optical benches arranged within the beam combiner spacecraft. The necessary optical processing includes:

- Transfer optics and spacecraft metrology;
- Correction and modulation, including optical delay lines, tip-tilt, deformable mirrors;

[10] Darwin is a mission that has been under study by the European Space Agency since 1996.

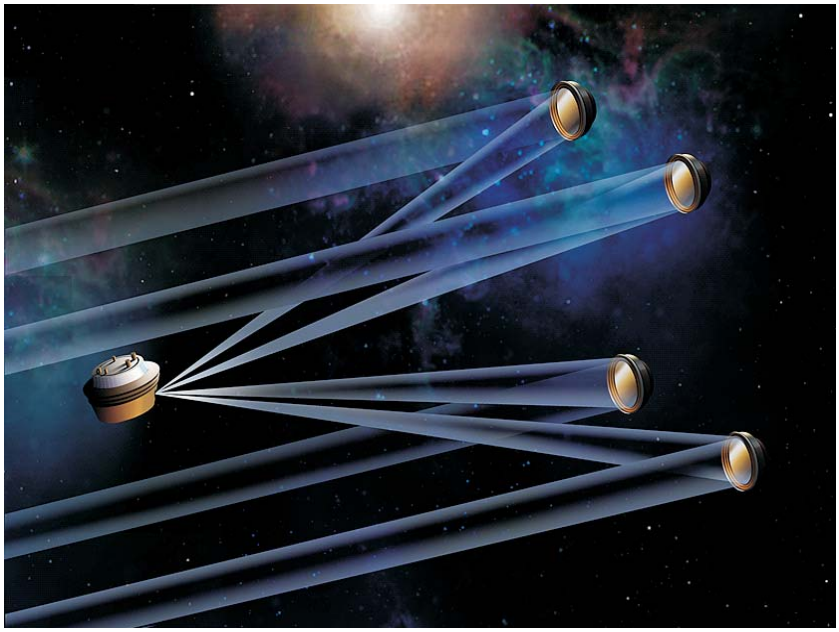

Figure 4.3: Artist impression of the Darwin space interferometer in its baseline "Emma X-array" configuration. It presents 4 telescopes and a beam combiner spacecraft, deployed and observing at the Sun-Earth Lagrange point L2.

- Mirrors, wavefront sensors and beam switching;
- Spectral separation, if necessary, to feed the science photons into 2 separate channels;
- Phase shifting, beam mixing;
- Recombination, spectral dispersion and detection.

Darwin is foreseen to be placed at the second Lagrange point (L2) by an Ariane 5 ECA vehicle (the total mass is significantly less than 6.6 tons, the launcher capability for delivery to L2). This placement at L2 is ideal to achieve passive cooling below 50 K of the collector and beam combiner spacecraft by means of sunshades. An additional refrigerator within the beam combiner spacecraft cools the detector assembly to below 10 K. Due to the configuration of the array and the need for solar avoidance, the instantaneous sky access is limited to an annulus with inner and outer half-angles of 46° and 83° centred on the anti-sun vector (Carle 2005, see Figure 4.4). This annulus transits the entire ecliptic circle during one year, giving access to almost the entire sky (see section 4.4).

4.2 The instability noise

Instability noise is defined as the component of the demodulated nulled signal that arises from phase and amplitude errors (see section 2.2.3). The underlying mechanism is that phase and amplitude errors induce an asymmetry between the two chopping states. Accordingly, the modulation map is no more centred on the nominal position of the line of sight (i.e. the position of the star) and a fraction of the starlight survives the modulation process and mixes with the planet photons. Instability noise is directly proportional to the stellar flux, so that it increases rapidly towards shorter wavelengths and for hotter stars. Moreover, at wavelengths where instability noise dominates, the SNR does not depend on the size of the apertures and is only weakly dependent on the target distance.

To estimate the mission performance in a realistic way, instability noise has to be taken into account. In the case of Darwin, the main imperfections result from vibrations and thermal drifts of the spacecraft,

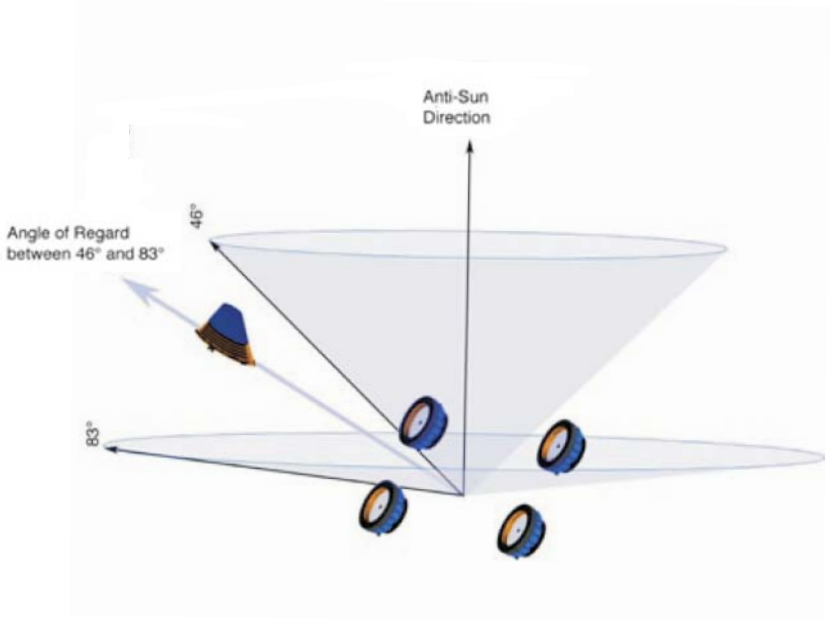

Figure 4.4: Observational constraints of the Emma X-array. At any given time, it can observe an annular region on the sky between 46° and 83° from the anti-Sun direction. During one Earth year, this annulus executes a complete circle, giving access to amost all regions of the celestial sphere.

which in turn generate small fluctuations in the phase and amplitude of the input light beams (d'Arcio 2005). Three independent studies (Lay 2004; d'Arcio 2005; Chazelas *et al.* 2006) have recently revisited the instrumental requirements on the Darwin mission in order to reduce the instrumental stellar leakage down to a sufficiently low level for Earth-like planet detection. Assuming the presence of 1/f-type noise, these studies showed that the requirements on amplitude and phase control are not driven by the null-floor leakage, but by the instability noise. In particular, the different analyses show that a null depth of $\sim 10^{-5}$ is generally sufficient to control the level of shot noise from the stellar leakage, but that a null depth of $\sim 10^{-6}$ is required to prevent instability noise from becoming the dominant source of noise. A 10^{-6} null requires rms path control to within about 1.5 nm, and rms amplitude control of about 0.1%. In order to relax these very stringent requirements, several techniques have been recently investigated:

- A first solution, proposed by Lay (2006), consists in stretching the array and applying a low-order polynomial fit to the instability noise (as a function of wavelength). By stretching the array, i.e. increasing the imaging baseline of the X-array, the interference pattern orthogonal to the nulling pattern shrinks. As the modulation map scales with wavelength, the planetary signal transmitted by the interferometer will then be a rapidly oscillation function of wavelength. On the other hand, instability noise is shown to be a low-order polynomial of the optical frequency $(1/\lambda)$. Therefore, by removing a low-order polynomial fit to the detected signal as a function of wavelength, the instability noise contribution is efficiently subtracted while preserving most of the planetary signal. This operation can actually be performed directly in the cross-correlation, by using a modified planet template where the polynomial components have been removed. Because this method strongly relies on the separation of the nulling and imaging baselines, it can only be efficiently applied with the X-array architecture.

- Another solution, based on the coherence properties of starlight, has been proposed by Lane *et al.* (2006) to separate the contributions from the planet and the instrumental leakage. The idea is to mix the electric fields of the leakage with that of a separate reference beam, also from the star, in order to form fringes (as long as the relative path delays are maintained within the coherence length). The light from the planet, being not coherent with the starlight, will not form fringes. Using as reference beam the bright output of a pair-wise nulling beam combiner, the amplitude

and phase mismatches in the input beams can be extracted from the fringe pattern, allowing the reconstruction of the the stellar leakage.

- A third solution has recently been proposed and tested by A. Léger and his team at IAS. The principle is to successively apply two ($< \lambda/2$) opposite OPD offsets to one of the beams in order to derive the actual position of the minimum in the transmission map. In this way, one feeds back the actual OPD errors to the delay line and prevents drifts from appearing. The same principle can be used to avoid amplitude drifts, by either blocking all but one beam to measure its actual amplitude or by modulating its amplitude as in the case of the OPD. The frequency at which this process is carried out depends on the input power spectra of the noise sources. It has been demonstrated experimentally in the lab that this process efficiently suppresses the 1/f-type noise generally present in the stellar contribution at the output of a Bracewell interferometer. This technique can theoretically be applied to any nulling configuration, but its efficiency decreases as the number of beams increases.

Others possible approaches (e.g. application of closure phase techniques, new chopping processes, exploiting correlations between measurements taken at different wavelength bins) have been suggested but still need to be investigated.

4.3 DARWINsim, the Darwin science simulator

The DARWINsim science simulation tool is an IDL-written code developed at ESA/ESTEC by R. den Hartog to assess the scientific return of the Darwin mission (den Hartog 2005b). For given instrumental configuration and target catalogue, DARWINsim computes the number of stars that can be surveyed for the presence of habitable planets and the number of possible follow-up spectroscopic observations during a nominal mission time.

The basic calculation in DARWINsim consists in an assessment of the required integration times for each individual target to fulfil user-specified SNR values for detection and for different spectroscopy scenarios. Note that the catalogue used in DARWINsim at the time of the simulations presented in section 4.4 is larger than the new Darwin target list (Kaltenegger *et al.* 2007a) as it contains 1132 stars (114 F, 200 G, 417 K and 401 M stars). In accordance to the interferometer architecture, DARWINsim first selects the stars which are observable during one year. For instance, among the 1132 stars of the catalogue, 625 are observable by the Emma X-array (43 F, 100 G, 241 K and 241 M stars). This is significantly more targets than with a planar configuration (about 440 stars observable during one year). For each of these observable stars, the baseline length is optimised to obtain the minimum integration time for a given SNR, taking into account shot noise contributions from stellar leakage, local and exozodiacal clouds, and instrumental infra-red foreground. The instability noise is also thoroughly implemented using the analytical method of Lay (Lay 2004, see section 2.2.1 for a brief overview of the method). All these noise contributors are described in details in the documentation of DARWINsim (den Hartog 2005b).

4.3.1 Detection phase

The observational strategy implemented in DARWINsim is different from the one discussed in section 3.5.1 for Pegase (3 observations, assuming that the planet is located in the middle of the HZ and at maximum elongation). Since the location of the planet inside the HZ is a priori unknown, three independent detections are necessary and each integration time is multiplied by three. For the same reason, the integration time (for one of the three observations) is computed from the requirement that it should be long enough to ensure the detection of a planet at 90% of the possible locations. As a first step, the probability distribution for finding a planet at a certain angular distance from the star has to be computed (see Figure 4.5). Note that it is necessary to consider a non-uniform distribution of orbit

inclinations in order to get a uniform distribution of orbital axes on the celestial sphere (edge-on systems are more probable). For each position the maximum SNR is then computed, obtained by the simultaneous optimisation of the baseline length and the wavelength range. Note that tests performed by R. den Hartog indicate that reconfiguration to other baselines to perform two or more shorter integrations is never advantageous compared to one single optimised baseline.

After the initial integration time assessment for detection, the targets are sorted by ascending integration time, removing from the list the targets for which the total integration time exceeds the total time during which they are visible from L2. Considering a slew time for re-targeting (nominally 6 hours) and some efficiency for the remaining observing time (nominally 70%), the sorted list is cut off where the cumulative integration time exceeds the nominal survey period. The resulting list defines the number of targets that can be surveyed.

4.3.2 Spectroscopy phase

The number of targets which can be surveyed for spectroscopy in a given time is computed similarly to the method described in the previous section for the detection phase. The only difference is that the integration times for spectroscopy are computed for the most likely position of the planet, which corresponds to circular orbits at random inclination. Then, the total integration time is determined by the requirement to detect the absorption lines of O_3, CO_2 and H_2O to a specified SNR. For the spectroscopy of CO_2 and O_3 (without H_2O), an SNR of 5 would actually be sufficient for a secure detection (Fridlund 2005). Considering the spectroscopy of H_2O is relatively more complex. Recent results suggest that, using a spectral resolution greater than 20, a SNR of 10 from 7.2 to 20 μm would be sufficient for H_2O, CO_2, and O_3 spectroscopy (private communication with F. Selsis, L. Kaltenegger and J. Paillet). In particular, the H_2O located below 7.2 μm, which is much more constraining that the H_2O band beyond 17.2 μm, could be discarded.

DARWINsim considers two types of spectroscopy: the staring spectroscopy, where the array is kept in a position such that the planet resides on a peak of the modulation map and the rotating spectroscopy, where the array keeps on rotating with respect to the target system such as the planet moves in and out of the peaks of the modulation map. Staring spectroscopy is more efficient in terms of signal acquisition, but requires an accurate knowledge of the planetary orbit. As for the detection phase, the total spectroscopy integration time should not exceed the total time during which the target is visible during the characterization phase. Accounting again for a certain fraction of overhead loss, the targets are sorted on ascending integration time, terminated where the cumulative time exceeds the length of nominal characterization period.

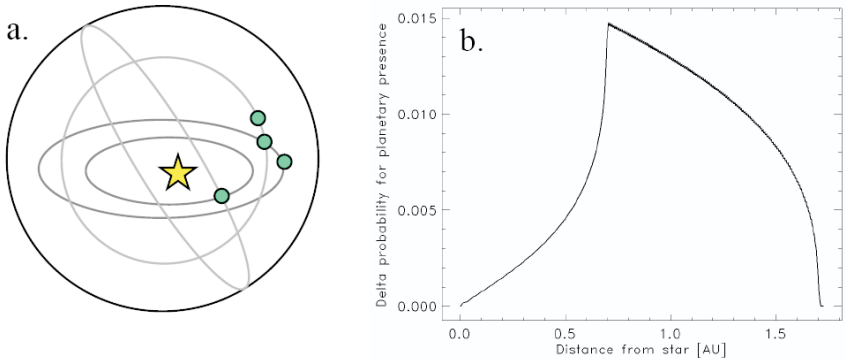

Figure 4.5: Left, a planet orbiting in the HZ of its host star can present various apparent distances, because the inclinations and phases of the orbits are a priori unknown. Right, probability distribution with respect to the apparent planet-star distance (figure from den Hartog 2005a).

4.4 Performance simulation

In order to prepare the Cosmic Vision proposal, performance predictions have been simulated using the DARWINsim software and cross-checked with comparable simulations at NASA/JPL with a home-made star count model. This section reports the results obtained.

4.4.1 Simulated performance for the Cosmic Vision proposal

The starting point of the simulations is the Darwin target list from which main sequence stars are selected in agreement with the array configuration. In the case of the Emma X-array architecture, 625 nearby main sequence stars are selected. For each target, the integration time is computed such that the probability for detecting an Earth-like planet within the (extended) HZ (located between 0.7 and 1.7 AU), at a signal-to-noise ratio of 5, is 90%. In average, the corresponding integration time is 30% longer than in the case where the planet is located in the middle of the HZ and at maximum elongation. As discussed in the previous section, a slew time of 6 hours is considered for re-targeting and about 70% of the remaining mission time is spent collecting data. In addition, it is assumed that 50% of the observing time is spent on G stars, 30% on K stars, and 10% on both F and M stars. Each star is assumed to host a terrestrial planet orbiting in the HZ ($\eta_\oplus = 1$). For instance, the solar system presents two planets in the HZ (Earth and Mars, Venus being very close). The CoRoT mission should reveal the abundance of small hot planets, and Kepler will evaluate $\eta_\oplus$, as well as the size distribution of these objects several years before Darwin flies. These inputs will allow the refinement of Darwin's observing strategy well in advance of launch. The thermal flux the habitable planet has been assumed to be identical to that of Earth whatever the distance to their host star. The flux of the exozodiacal clouds has been computed

Telescope diameter	1-m	2-m	3-m	2-m	2-m
Planet radius [$R_\oplus$]	1	1	1	1.5	2
Detection					
Surveyed (5 years)	119	346	599	611	625
Surveyed (2 years)	76	218	405	437	593
♯ F stars	5	14	30	36	43
♯ G stars	15	53	100	100	100
♯ K stars	20	74	152	167	241
♯ M stars	36	77	123	134	209
Spectroscopy					
Staring (CO_2,O_3)	26	72	136	173	323
Rotating (CO_2,O_3)	17	49	87	113	217
♯ F stars	1	2	3	6	11
♯ G stars	4	8	15	22	48
♯ K stars	3	12	25	33	72
♯ M stars	9	27	44	52	86
Staring (H_2O)	17	36	62	85	170
Rotating (H_2O)	14	24	43	55	110
♯ F stars	0	1	1	3	6
♯ G stars	2	4	7	9	21
♯ K stars	1	5	10	14	32
♯ M stars	11	14	25	29	51

Table 4.1: Expected performance in terms of number of stars surveyed and planets characterised during the nominal 5-year mission for various telescope diameters and planet radii. All stars are assumed to host a planet in the habitable zone and to be surrounded by an exozodiacal cloud 3 times denser that in the solar system.

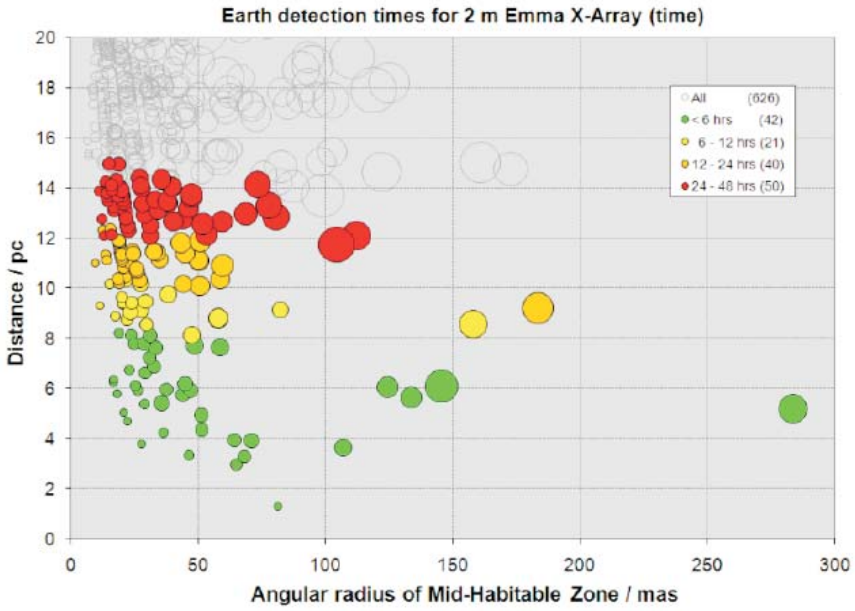

Figure 4.6: Integration times needed to detect Earth-sized planets with an SNR of 5 around each of the Darwin candidate targets, represented as circles proportional to their intrinsic diameter. Integration times longer than 24 hours are not shown, but are not precluded.

assuming a mean density 3 times that in the solar system (an assumption supported by the theoretical models, see Chapter 1). Under the assumption that the exozodiacal emission is symmetric around the target star, it will be suppressed by the chopping process, and therefore only contribute to the shot noise (the impact of the exozodiacal level on the performance is addressed in section 4.4.2).

Assuming an optical throughput of 10%, the results of the simulations for the Emma X-array (with an aspect ratio of 6:1) are presented for different aperture sizes in Table 4.1. The science band ranges from 6 to 20 μm and has been subdivided into two sub-bands, that match two different fibers: 6-11.5 μm and 11.5-20 μm. Considering Earth-radius planets within the HZ, about 200 stars, well spread among the four selected spectral types, can be surveyed during the nominal 2-year survey. This number reaches about 400 with 3-m aperture telescopes. Darwin will thus provide statistically meaningful results on nearby planetary systems. Figure 4.6 shows that nearby K and M dwarfs (small circles to the lower left) are the best-suited targets in terms of Earth-like planet detection (the same conclusion has been drawn for the Pegasus mission, see section 3.4).

For the spectroscopy phase, a required SNR of 5 has been assumed for the detection of CO_2 and O_3, as discussed in section 4.3. For the full characterisation (i.e. searching for the presence of H_2O, CO_2, and O_3), the required SNR has been fixed to 10 on the 7.2-20-μm wavelength range. With these assumptions, CO_2 and O_3 could be searched in about 50 planets (resp. 70) with rotational spectroscopy (resp. staring spectroscopy) while H_2O could potentially be detected on 24 (resp. 36) planets during the 3-year characterisation phase. These values would be roughly doubled (resp. halved) for 3-m aperture telescopes (resp. 1-m aperture telescopes). Although staring spectroscopy presents (as expected) better results, rotational spectroscopy is more secure since it does not rely on any uncertainty on the localisation of the planet. It is also interesting to note that in the case of planets with radii 1.5 time (resp. 2 times) as large as that of Earth, the number of planets for which H_2O spectroscopy could be performed, is doubled (resp. quadrupled), as shown in Table 4.1. For 2 Earth-radius planets, almost the whole Darwin catalogue (restricted to the part of the sky available to the Emma X-array configuration) could even be surveyed.

4.4.2 Impact of the exozodiacal level

As discussed in section 3.1.1, the level of exozodiacal emission is an important parameter to consider in the process of assessing the performance of a nulling interferometer. In order to provide an overview of its impact, Table 4.2 reports the simulated performance of Darwin for various assumptions on the exozodiacal density. Increasing the exozodiacal level from 3 to 20 zodis has a relatively low (negative) impact on the performance of both detection and spectroscopy phases. For a 100-zodi level, the decrease in performance is more pronounced but the results remain roughly of the same order. However, the simulations performed with DARWINsim have been carried out under the assumption that the exozodiacal emission is symmetric around the target star, so that it is suppressed by the chopping process (and therefore only contribute to the shot noise). If the exozodiacal cloud is asymmetric[11], a part of its emission would not be cancelled by the chopping process and could mimic the planetary signal. This behaviour would be particularly harmful for bright exozodiacal clouds and in practice, it is expected that exozodiacal clouds with a density level larger than 20 zodis will significantly hamper the detection of Earth-like planets. More investigations are necessary in the context of the present mission architecture to define a secure upper limit on the exozodiacal cloud density.

Telescope diameter	2-m	2-m	2-m
Exozodiacal density	3	20	100
Detection			
Surveyed (5 years)	346	335	284
Surveyed (2 years)	218	212	175
♯ F stars	14	12	8
♯ G stars	53	50	35
♯ K stars	74	72	59
♯ M stars	77	78	73
Spectroscopy			
Staring (CO_2,O_3)	72	64	45
Rotating (CO_2,O_3)	49	44	32
♯ F stars	2	2	1
♯ G stars	8	6	4
♯ K stars	12	10	7
♯ M stars	27	26	20
Staring (H_2O)	36	34	23
Rotating (H_2O)	24	19	16
♯ F stars	1	1	0
♯ G stars	4	3	2
♯ K stars	5	4	4
♯ M stars	14	11	10

Table 4.2: Expected performance in terms of number of stars which can be surveyed and planets which can be characterised during the nominal 5-year mission lifetime, for various assumptions on the exozodiacal density.

4.4.3 Impact of the H_2O detection strategy

In this section, two different strategies for the H_2O spectroscopy are briefly addressed. As already discussed in section 4.3, recent results suggest that requiring an SNR of 10 from 7.2 to 20 μm would be sufficient for H_2O, CO_2, and O_3 spectroscopy, provided that the spectral resolution is greater than 20. In particular, this new approach (the A strategy) for H_2O spectroscopy does not consider the H_2O band

[11] For instance, the solar zodiacal cloud is shifted from the Sun by about 0.013 AU in the ecliptic plane.

Telescope diameter	2-m	2-m	2-m	2-m
Catalogue	Darwin	TPF	Darwin	TPF
Exozodiacal density	3	3	3	3
H_2O strategy	A	A	B	B
Staring (H_2O)	36	33	21	16
Rotating (H_2O)	24	19	11	10
♯ F stars	1	1	1	0
♯ G stars	4	5	3	3
♯ K stars	5	10	1	5
♯ M stars	14	3	6	2

Table 4.3: Performance prediction for two H_2O spectroscopy strategies: the strategy A for which an SNR of 10 is required on the 17.2-20-μm H_2O band and the strategy B for which an SNR of 10 is also required on the 6.0-7.2-μm band. The results of DARWINsim applied to the TPF catalogue are also given for comparison.

between 6 and 7.2 μm. On the other hand, the B strategy takes both H_2O bands into account. The comparative results are shown in Table 4.3, showing that considering the H_2O band between 6 and 7.2 μm is significantly harmful for the spectroscopy (the performance is roughly divided by a factor 2). The results of DARWINsim applied to the TPF catalogue are also given for comparison. The TPF catalogue is slightly different from that of Darwin since it contains targets located up to 30 pc (instead of 25 pc for Darwin) and amounts to 1001 main sequence stars (for the Emma X-array configuration). The simulated performance indicates that about the same number of stars could be the spectroscopically characterised, with a deficit of M stars compensated by an excess of K stars.

Conclusion

Infrared nulling interferometry is the core technique of several life-finding space missions such as ESA's Darwin and NASA's Terrestrial Planet Finder (TPF). Observing in the infrared (6-20 μm), these missions will be able to characterise the atmosphere of habitable extrasolar planets orbiting around nearby main sequence stars. This ability to study distant planets strongly depends on the density of exozodiacal clouds around the stars, which can hamper the planet detection. As a consequence, assessing the level of circumstellar dust around nearby main sequence stars is a necessary pre-requisite to prepare the observing programmes of Darwin and TPF. Several ground-based nulling instruments (e.g. KIN and LBTI) will be dedicated to this purpose. Complementary European projects, such as the 1-m telescope nulling interferometer for Antarctica (ALADDIN), are also under study. However, these ground-based demonstrators will suffer from the atmospheric thermal background and its variations. Observing from space would provide an efficient way to get round this problem. In that context, the Pegase mission, aimed at studying known hot extrasolar giant planets located within 150 pc, could be a valuable scientific precursor.

The first part of this work is dedicated to the performance study of Pegase for the detection of exozodiacal discs. To this end, the GENIEsim software has been adapted to enable the simulation of space-based nulling interferometers. The results obtained for four representative targets of the Darwin catalogue show the very attractive capabilities of Pegase, achieving its optimum sensitivity very quickly (in a few minutes) due to the low thermal background. In particular, the performance of Pegase might be significantly boosted by considering a shorter-baseline configuration (e.g. triangular rather than linear). With a minimum baseline length of 20 m, a triangular Pegase can detect exozodiacal discs about 30 times denser than the solar disc and outperform ALADDIN for the most distant targets of the Darwin/TPF catalogue. However, ALADDIN is generally more sensitive for long integration times. Regarding the exozodiacal disc detection around the Darwin/TPF targets as sole objective, ALADDIN presents a better performance/price ratio than PEGASE and should be preferred, particularly if the final objective is to reach a sensitivity level of 20 zodis.

Another major contribution of this work is the investigation of the performance for planet detection of Pegase and Pegasus. Pegasus is an upgraded version of Pegase presenting Darwin-like specifications and using only two telescopes (of 1-m diameter). Considering the 61 extrasolar planets known in the close vicinity of the solar system (within 25 pc), Pegasus could perform spectroscopy for about 45% of them instead of 15% with Pegase. Performance improvements are also considered by addressing specific modulation methods (namely the split-pupil and OPD modulation techniques) to mitigate the harmful exozodiacal emission. Further investigations of Pegasus have been carried out to assess which objectives of Darwin could be achieved. Observing the habitable zone of a Sun-like star located at 20 pc, Pegasus could detect in one year about 50 Neptune-like planets ($M \sim 0.05\ M_{Jup}$). In particular, Pegasus would be very efficient to search for 2 Earth-radius terrestrial planets orbiting around M stars located within 10 pc. As for the exozodiacal disc detection, a short-baseline configuration presents a significant advantage to the final number of planets which can be studied.

Finally, the performance of Darwin is addressed. Based on the recent convergence between ESA and NASA on the mission architecture (Emma X-array), the performance of Darwin is computed in collaboration with NASA/JPL, carrying out similar simulation efforts for TPF. The new baseline configuration

of Darwin (Emma X-array) could detect about 200 Earth-like planets during the 2-year detection phase and perform spectroscopy for about 25 of them in the remaining three years of the mission lifetime. These performance predictions have been used as input values for the Cosmic Vision proposal (2007).

Prospects and follow-on activities

The next step will be to validate the performance predictions for the extrasolar planet detection of Pegase and Pegasus with GENIEsim. Since GENIEsim is now ready to simulate the performance of space-based nulling interferometers, this will be relatively straightforward. Another interesting study will be to compare the performance for exozodiacal disc detection of Pegase with US ground-based nulling interferometers, particularly with KIN and LBTI. For Darwin, the follow-on activities will be to pursue and consolidate the simulation efforts, particularly if the mission is selected by ESA as part of the 2015-2025 Cosmic Vision plan.

Bibliography

O. Absil, R. den Hartog, P. Gondoin, P. Fabry, R. Wilhelm, P. Gitton, and F. Puech. Performance study of ground-based infrared Bracewell interferometers. Application to the detection of exozodiacal dust disks with GENIE. *A&A*, 448:787–800, March 2006.

O. Absil, E. di Folco, A. Mérand, J.-C. Augereau, V. Coudé Du Foresto, J. P. Aufdenberg, P. Kervella, S. T. Ridgway, D. H. Berger, T. A. Ten Brummelaar, J. Sturmann, L. Sturmann, N. H. Turner, and H. A. McAlister. Circumstellar material in the Vega inner system revealed by CHARA/FLUOR. *A&A*, 452:237–244, June 2006.

O. Absil, V. Coudé du Foresto, M. Barillot, and M.R. Swain. Nulling interferometry: comparison of performances between Antarctica and other ground-based sites. *A&A, submitted*, 2007.

O. Absil. Nulling interferometry with IRSI-Darwin: Detection and Characterization of Earth-like Exoplanets. Master's thesis, Liège University, Liège, Belgium, *http://vela.astro.ulg.ac.be/themes/telins/harigs/*, 2001.

O. Absil. *Astophysical studies of extrasolar planetary systems using infrared interferometric techniques.* PhD thesis, Liège University, Liège, Belgium, 2006.

Y. Alibert, C. Mordasini, W. Benz, and C. Winisdoerffer. Models of giant planet formation with migration and disc evolution. *A&A*, 434:343–353, April 2005.

J. R. P. Angel and N. J. Woolf. An Imaging Nulling Interferometer to Study Extrasolar Planets. *ApJ*, 475:373–+, January 1997.

J. C. Augereau and J. C. B. Papaloizou. Structuring the <ASTROBJ>HD 141569 A</ASTROBJ> circumstellar dust disk. Impact of eccentric bound stellar companions. *A&A*, 414:1153–1164, February 2004.

H. H. Aumann, C. A. Beichman, F. C. Gillett, T. de Jong, J. R. Houck, F. J. Low, G. Neugebauer, R. G. Walker, and P. R. Wesselius. Discovery of a shell around Alpha Lyrae. *ApJ*, 278:L23–L27, March 1984.

D. E. Backman and F. Paresce. Main-sequence stars with circumstellar solid material - The VEGA phenomenon. In E. H. Levy and J. I. Lunine, editors, *Protostars and Planets III*, pages 1253–1304, 1993.

A. Baglin, M. Auvergne, P. Barge, E. Michel, C. Catala, M. Deleuil, and W. Weiss. The CoRoT mission and its scientific objectives. In *American Institute of Physics Conference Series*, volume 895 of *American Institute of Physics Conference Series*, pages 201–209, March 2007.

T. S. Barman, P. H. Hauschildt, and F. Allard. Irradiated Planets. *ApJ*, 556:885–895, August 2001.

T. S. Barman. Identification of Absorption Features in an Extrasolar Planet Atmosphere. *ApJ*, 661:L191–L194, June 2007.

P. Baudoz, A. Boccaletti, P. Riaud, C. Cavarroc, J. Baudrand, J. M. Reess, and D. Rouan. Feasibility of the Four-Quadrant Phase Mask in the Mid-Infrared on the James Webb Space Telescope. *PASP*, 118:765–773, May 2006.

C. A. Beichman, G. Bryden, T. N. Gautier, K. R. Stapelfeldt, M. W. Werner, K. Misselt, G. Rieke, J. Stansberry, and D. Trilling. An Excess Due to Small Grains around the Nearby K0 V Star HD 69830: Asteroid or Cometary Debris? *ApJ*, 626:1061–1069, June 2005.

C. A. Beichman, G. Bryden, G. H. Rieke, J. A. Stansberry, D. E. Trilling, K. R. Stapelfeldt, M. W. Werner, C. W. Engelbracht, M. Blaylock, K. D. Gordon, C. H. Chen, K. Y. L. Su, and D. C. Hines. Planets and Infrared Excesses: Preliminary Results from a Spitzer MIPS Survey of Solar-Type Stars. *ApJ*, 622:1160–1170, April 2005.

C. Beichman, P. Lawson, O. Lay, A. Ahmed, S. Unwin, and K. Johnston. Status of the terrestrial planet finder interferometer (TPF-I). In *Advances in Stellar Interferometry. Edited by Monnier, John D.; Schöller, Markus; Danchi, William C.. Proceedings of the SPIE, Volume 6268, pp. 62680S (2006).*, volume 6268, July 2006.

C. A. Beichman, G. Bryden, K. R. Stapelfeldt, T. N. Gautier, K. Grogan, M. Shao, T. Velusamy, S. M. Lawler, M. Blaylock, G. H. Rieke, J. I. Lunine, D. A. Fischer, G. W. Marcy, J. S. Greaves, M. C. Wyatt, W. S. Holland, and W. R. F. Dent. New Debris Disks around Nearby Main-Sequence Stars: Impact on the Direct Detection of Planets. *ApJ*, 652:1674–1693, December 2006.

C. A. Beichman, A. Tanner, G. Bryden, K. R. Stapelfeldt, M. W. Werner, G. H. Rieke, D. E. Trilling, S. Lawler, and T. N. Gautier. IRS Spectra of Solar-Type Stars: A Search for Asteroid Belt Analogs. *ApJ*, 639:1166–1176, March 2006.

H. Beust, A.-M. Lagrange, F. Plazy, and D. Mouillet. The β Pictoris circumstellar disk. XXII. Investigating the model of multiple cometary infalls. *A&A*, 310:181–198, June 1996.

P. Bodenheimer. The Role of Dust in Star and Planet Formation: Theory. In Y. J. Pendleton, editor, *From Stardust to Planetesimals*, volume 122 of *Astronomical Society of the Pacific Conference Series*, pages 37–+, 1997.

P. Bordé, D. Rouan, and A. Léger. Exoplanet detection capability of the COROT space mission. *A&A*, 405:1137–1144, July 2003.

W. J. Borucki, D. G. Koch, J. Lissauer, G. Basri, T. Brown, D. A. Caldwell, J. M. Jenkins, J. J. Caldwell, J. Christensen-Dalsgaard, W. D. Cochran, E. W. Dunham, T. N. Gautier, J. C. Geary, D. Latham, D. Sasselov, R. L. Gilliland, S. Howell, D. G. Monet, and N. Batalha. KEPLER Mission Status. In C. Afonso, D. Weldrake, and T. Henning, editors, *Transiting Extrapolar Planets Workshop*, volume 366 of *Astronomical Society of the Pacific Conference Series*, pages 309–+, July 2007.

A. P. Boss. The Jeans Mass Constraint and the Fragmentation of Molecular Cloud Cores. *ApJ*, 501:L77+, July 1998.

A. P. Boss. Rapid Formation of Outer Giant Planets by Disk Instability. *ApJ*, 599:577–581, December 2003.

R. N. Bracewell. Detecting nonsolar planets by spinning infrared interferometer. *Nature*, 274:780–+, August 1978.

G. Bryden, C. A. Beichman, D. E. Trilling, G. H. Rieke, E. K. Holmes, S. M. Lawler, K. R. Stapelfeldt, M. W. Werner, T. N. Gautier, M. Blaylock, K. D. Gordon, J. A. Stansberry, and K. Y. L. Su. Frequency of Debris Disks around Solar-Type Stars: First Results from a Spitzer MIPS Survey. *ApJ*, 636:1098–1113, January 2006.

A. Burrows, D. Sudarsky, and I. Hubeny. Spectra and Diagnostics for the Direct Detection of Wide-Separation Extrasolar Giant Planets. *ApJ*, 609:407–416, July 2004.

A. Burrows, D. Sudarsky, and I. Hubeny. Theory for the Secondary Eclipse Fluxes, Spectra, Atmospheres, and Light Curves of Transiting Extrasolar Giant Planets. *ApJ*, 650:1140–1149, October 2006.

A. G. W. Cameron. Physics of the primitive solar accretion disk. *Moon and Planets*, 18:5–40, February 1978.

E. Carle. EMMA configuration: evaluation of optical performances. Technical Report Issue 1, ESA (SCI-A/279), 2005.

G. Chabrier, I. Baraffe, F. Allard, and P. Hauschildt. Deuterium Burning in Substellar Objects. *ApJ*, 542:L119–L122, October 2000.

D. Charbonneau, L. E. Allen, S. T. Megeath, G. Torres, R. Alonso, T. M. Brown, R. L. Gilliland, D. W. Latham, G. Mandushev, F. T. O'Donovan, and A. Sozzetti. Detection of Thermal Emission from an Extrasolar Planet. *ApJ*, 626:523–529, June 2005.

D. Charbonneau, J. N. Winn, D. W. Latham, G. Bakos, E. E. Falco, M. J. Holman, R. W. Noyes, B. Csák, G. A. Esquerdo, M. E. Everett, and F. T. O'Donovan. Transit Photometry of the Core-dominated Planet HD 149026b. *ApJ*, 636:445–452, January 2006.

B. Chazelas, F. Brachet, P. Bordé, B. Mennesson, M. Ollivier, O. Absil, A. Labèque, C. Valette, and A. Léger. Instrumental stability requirements for exoplanet detection with a nulling interferometer: variability noise as a central issue. *Appl. Opt.*, 45:984–992, February 2006.

D. R. Ciardi, G. T. van Belle, R. L. Akeson, R. R. Thompson, E. A. Lada, and S. B. Howell. On the Near-Infrared Size of Vega. *ApJ*, 559:1147–1154, October 2001.

M. Clampin. Optical Design of the James Webb Space Telescope (JWST). In P. Kalas, editor, *Proceedings of the conference In the Spirit of Bernard Lyot: The Direct Detection of Planets and Circumstellar Disks in the 21st Century. June 04 - 08, 2007. University of California, Berkeley, CA, USA. Edited by Paul Kalas.*, pages 49–+, June 2007.

M. M. Colavita, G. Serabyn, P. L. Wizinowich, and R. L. Akeson. Nulling at the Keck interferometer. In *Advances in Stellar Interferometry. Edited by Monnier, John D.; Schöller, Markus; Danchi, William C.. Proceedings of the SPIE, Volume 6268, pp. 626803 (2006).*, volume 6268 of *Presented at the Society of Photo-Optical Instrumentation Engineers (SPIE) Conference*, July 2006.

V. Coudé du Foresto, O. Absil, M. Swain, F. Vakili, and M. Barillot. ALADDIN: an optimized nulling ground-based demonstrator for DARWIN. In *Advances in Stellar Interferometry. Edited by Monnier, John D.; Schöller, Markus; Danchi, William C.. Proceedings of the SPIE, Volume 6268, pp. 626810 (2006).*, volume 6268 of *Presented at the Society of Photo-Optical Instrumentation Engineers (SPIE) Conference*, July 2006.

F. Crifo and The French Gaia Team. GAIA: present status and preparation of data analysis. In D. Barret, F. Casoli, G. Lagache, A. Lecavelier, and L. Pagani, editors, *SF2A-2006: Semaine de l'Astrophysique Francaise*, pages 459–+, June 2006.

G. D'Angelo, S. H. Lubow, and M. R. Bate. Evolution of Giant Planets in Eccentric Disks. *ApJ*, 652:1698–1714, December 2006.

L. L. D'Arcio, A. L. Karlsson, and P. A. Gondoin. Use of OPD modulation techniques in nulling interferometry. In W. A. Traub, editor, *New Frontiers in Stellar Interferometry, Proceedings of SPIE Volume 5491*, pages 851–+, October 2004.

L. d'Arcio. DARWIN. Variability noise sensitivity analysis. (Issue 1), 2005.

D. Defrère, O. Absil, and V. Coudé Du Foresto. Performance study of space-based infrared Bracewell interferometers. Comparison with ground-based sites for exozodiacal disc detection. *A&A*, in prep., 2007.

D. Defrère, O. Absil, C. Hanot, and M. Fridlund. Potential of space-based infrared Bracewell interferometers for planet detection. In *Proceedings of the SPIE (2007)*, Presented at the Society of Photo-Optical Instrumentation Engineers (SPIE) Conference, pages 6693–6694, 2007.

D. Deming, S. Seager, L. J. Richardson, and J. Harrington. Infrared radiation from an extrasolar planet. *Nature*, 434:740–743, March 2005.

D. Deming, J. Harrington, G. Laughlin, S. Seager, S. B. Navarro, W. C. Bowman, and K. Horning. Spitzer Transit and Secondary Eclipse Photometry of GJ 436b. *ArXiv e-prints*, 707, July 2007.

R. H. den Hartog, O. Absil, P. A. Gondoin, L. L. D'Arcio, P. Fabry, L. Kaltenegger, R. C. Wilhelm, P. B. Gitton, F. Puech, and C. V. M. Fridlund. The simulated detection of low-mass companions with GENIE. In W. A. Traub, editor, *New Frontiers in Stellar Interferometry, Proceedings of SPIE Volume 5491. Edited by Wesley A. Traub. Bellingham, WA: The International Society for Optical Engineering, 2004., p.160*, volume 5491 of *Presented at the Society of Photo-Optical Instrumentation Engineers (SPIE) Conference*, pages 160–+, October 2004.

R. den Hartog. DARWIN science performance prediction. Technical Report Issue 1, ESA (SCI-A/300), May 2005.

R. den Hartog. The DARWINsim science simulator. Technical Report Issue 1, ESA (SCI-A/297), May 2005.

E. Di Folco, F. Thévenin, P. Kervella, A. Domiciano de Souza, V. Coudé du Foresto, D. Ségransan, and P. Morel. VLTI near-IR interferometric observations of Vega-like stars. Radius and age of α PsA, β Leo, β Pic, ϵ Eri and τ Cet. *A&A*, 426:601–617, November 2004.

E. di Folco, O. Absil, J.-C. Augereau, A. Mérand, V. Coudé Du Foresto, F. Thévenin, J. P. Defrère D., J. P. Aufdenberg, P. Kervella, S. T. Ridgway, T. A. Ten Brummelaar, J. Sturmann, L. Sturmann, N. H. Turner, and H. A. McAlister. A near-infrared interferometric survey of debris disc stars. II. Probing the hot dust content around ϵ Eri and τ Cet with CHARA/FLUOR. *A&A*, in press., 2007.

S. B. Fajardo-Acosta, R. E. Stencel, and D. E. Backman. Infrared Space Observatory Mapping of 60 Micron Dust Emission around Vega-Type Systems: Erratum. *ApJ*, 503:L193+, August 1998.

S. B. Fajardo-Acosta, C. A. Beichman, and R. M. Cutri. Discovery of New Candidate Vega-type Systems from IRAS and the 2 Micron All-Sky Survey. *ApJ*, 538:L155–L158, August 2000.

H. Fizeau and L. Foucault. Ueber das Phänomen der Interferenz zweier Lichtstrahlen im Falle grosser Gangunterschiede. *Annalen der Physik*, 149:355–358, 1847.

C. V. M. Fridlund, L. d'Arcio, R. den Hartog, and A. Karlsson. Status and recent progress of the Darwin mission in the Cosmic Vision program. In *Advances in Stellar Interferometry. Edited by Monnier, John D.; Schöller, Markus; Danchi, William C.. Proceedings of the SPIE, Volume 6268, pp. 62680R (2006).*, volume 6268, July 2006.

M. Fridlund. Darwin Science Requirements Document. Technical Report Issue 5, ESA (SCI-A), 2005.

P. Goldreich and S. Tremaine. The excitation of density waves at the Lindblad and corotation resonances by an external potential. *ApJ*, 233:857–871, November 1979.

P. A. Gondoin, O. Absil, R. H. den Hartog, R. C. Wilhelm, P. B. Gitton, L. L. D'Arcio, P. Fabry, F. Puech, M. C. Fridlund, M. Schoeller, A. Glindemann, E. J. Bakker, A. L. Karlsson, A. J. Peacock, S. Volonte, F. Paresce, and A. Richichi. Darwin-GENIE: a nulling instrument at the VLTI. In W. A.

Traub, editor, *New Frontiers in Stellar Interferometry, Proceedings of SPIE Volume 5491. Edited by Wesley A. Traub. Bellingham, WA: The International Society for Optical Engineering, 2004., p.775*, volume 5491, pages 775–+, October 2004.

J. S. Greaves, M. C. Wyatt, W. S. Holland, and W. R. F. Dent. The debris disc around τ Ceti: a massive analogue to the Kuiper Belt. *MNRAS*, 351:L54–L58, July 2004.

J. S. Greaves, D. A. Fischer, and M. C. Wyatt. Metallicity, debris discs and planets. *MNRAS*, 366:283–286, February 2006.

K. E. Haisch, Jr., E. A. Lada, and C. J. Lada. Disk Frequencies and Lifetimes in Young Clusters. *ApJ*, 553:L153–L156, June 2001.

C. Hanot. Investigation of a down scoped version of the darwin mission. Master's thesis, Liège University, Liège, Belgium, 2005.

J. Harrington, B. M. Hansen, S. H. Luszcz, S. Seager, D. Deming, K. Menou, J. Y.-K. Cho, and L. J. Richardson. The Phase-Dependent Infrared Brightness of the Extrasolar Planet υ Andromedae b. *Science*, 314:623–626, October 2006.

S. R. Heap, D. J. Lindler, T. M. Lanz, R. H. Cornett, I. Hubeny, S. P. Maran, and B. Woodgate. Space Telescope Imaging Spectrograph Coronagraphic Observations of β Pictoris. *ApJ*, 539:435–444, August 2000.

P. M. Hinz, J. R. P. Angel, W. F. Hoffmann, D. W. McCarthy, P. C. McGuire, M. Cheselka, J. L. Hora, and N. J. Woolf. First results of nulling interferometry with the Multiple-Mirror Telescope. In R. D. Reasenberg, editor, *Proc. SPIE Vol. 3350, p. 439-447, Astronomical Interferometry, Robert D. Reasenberg; Ed.*, volume 3350 of *Presented at the Society of Photo-Optical Instrumentation Engineers (SPIE) Conference*, pages 439–447, July 1998.

P. M. Hinz, J. R. P. Angel, W. F. Hoffmann, D. W. McCarthy, N. J. Woolf, and P. C. McGuire. Refining Nulling Interferometry with the Old and New Multiple Mirror Telescope. In *Bulletin of the American Astronomical Society*, volume 30 of *Bulletin of the American Astronomical Society*, pages 1393–+, December 1998.

W. S. Holland, J. S. Greaves, B. Zuckerman, R. A. Webb, C. McCarthy, I. M. Coulson, D. M. Walther, W. R. F. Dent, W. K. Gear, and I. Robson. Submillimetre images of dusty debris around nearby stars. *Nature*, 392:788–791, April 1998.

W. S. Holland, J. S. Greaves, W. R. F. Dent, M. C. Wyatt, B. Zuckerman, R. A. Webb, C. McCarthy, I. M. Coulson, E. I. Robson, and W. K. Gear. Submillimeter Observations of an Asymmetric Dust Disk around Fomalhaut. *ApJ*, 582:1141–1146, January 2003.

P. Kalas, M. C. Liu, and B. C. Matthews. Discovery of a Large Dust Disk Around the Nearby Star AU Microscopii. *Science*, 303:1990–1992, March 2004.

P. Kalas, J. R. Graham, M. C. Clampin, and M. P. Fitzgerald. First Scattered Light Images of Debris Disks around HD 53143 and HD 139664. *ApJ*, 637:L57–L60, January 2006.

L. Kaltenegger, C. Eiroa, A. Stankov, and M. Fridlund. Nearby Stellar sample for the search for terrestrial planets. Target star catalogue for the Darwin Mission Study. *A&A, submitted*, 2007.

L. Kaltenegger, W. A. Traub, and K. W. Jucks. Spectral Evolution of an Earth-like Planet. *ApJ*, 658:598–616, March 2007.

A. L. Karlsson, O. Wallner, J. M. Perdigues Armengol, and O. Absil. Three telescope nuller based on multibeam injection into single-mode waveguide. In W. A. Traub, editor, *New Frontiers in Stellar Interferometry, Proceedings of SPIE Volume 5491. Edited by Wesley A. Traub. Bellingham, WA: The*

International Society for Optical Engineering, 2004., p.831, volume 5491 of *Presented at the Society of Photo-Optical Instrumentation Engineers (SPIE) Conference*, pages 831–+, October 2004.

J. F. Kasting, D. P. Whitmire, and R. T. Reynolds. Habitable Zones around Main Sequence Stars. *Icarus*, 101:108–128, January 1993.

T. Kelsall, J. L. Weiland, B. A. Franz, W. T. Reach, R. G. Arendt, E. Dwek, H. T. Freudenreich, M. G. Hauser, S. H. Moseley, N. P. Odegard, R. F. Silverberg, and E. L. Wright. The COBE Diffuse Infrared Background Experiment Search for the Cosmic Infrared Background. II. Model of the Interplanetary Dust Cloud. *ApJ*, 508:44–73, November 1998.

H. Klahr and P. Bodenheimer. Formation of Giant Planets by Concurrent Accretion of Solids and Gas inside an Anticyclonic Vortex. *ApJ*, 639:432–440, March 2006.

M. J. Kuchner and S. Seager. Extrasolar Carbon Planets. April 2005.

A. Labeyrie. Interference fringes obtained on VEGA with two optical telescopes. *ApJ*, 196:L71–L75, March 1975.

B. F. Lane, M. W. Muterspaugh, and M. Shao. Calibrating an Interferometric Null. *ApJ*, 648:1276–1284, September 2006.

R. J. Laureijs, M. Jourdain de Muizon, K. Leech, R. Siebenmorgen, C. Dominik, H. J. Habing, N. Trams, and M. F. Kessler. A 25 micron search for Vega-like disks around main-sequence stars with ISO. *A&A*, 387:285–293, May 2002.

P. Lawson and W. Traub. Earth-Like Exoplanets: The Science of NASA's Navigator Program. Technical report, NASA, 2006.

P. Lawson. Results of Laboratory Experiments Kin Nulling Interferometry (1998-2006). In *the proceedings of the TPF/Darwin 2006 conference*, 2006.

O. P. Lay. Systematic Errors in Nulling Interferometers. *Appl. Opt.*, 43:6100–6123, November 2004.

O. P. Lay. Imaging properties of rotating nulling interferometers. *Appl. Opt.*, 44:5859–5871, October 2005.

O. P. Lay. Removing instability noise in nulling interferometers. In *Advances in Stellar Interferometry. Edited by Monnier, John D.; Schöller, Markus; Danchi, William C.. Proceedings of the SPIE, Volume 6268, pp. 62681A (2006).*, volume 6268 of *Presented at the Society of Photo-Optical Instrumentation Engineers (SPIE) Conference*, July 2006.

J. M. Le Duigou, M. Ollivier, A. Léger, F. Cassaing, B. Sorrente, B. Fleury, G. Rousset, O. Absil, D. Mourard, Y. Rabbia, L. Escarrat, F. Malbet, D. Rouan, R. Clédassou, M. Delpech, P. Duchon, B. Meyssignac, P.-Y. Guidotti, and N. Gorius. Pegase: a space-based nulling interferometer. In *Space Telescopes and Instrumentation I: Optical, Infrared, and Millimeter. Edited by Mather, John C.; MacEwen, Howard A.; de Graauw, Mattheus W. M.. Proceedings of the SPIE, Volume 6265, pp. 62651M (2006).*, volume 6265, July 2006.

A. Léger, M. Ollivier, K. Altwegg, and N. J. Woolf. Is the presence of H_2O and O_3 in an exoplanet a reliable signature of a biological activity? *A&A*, 341:304–311, January 1999.

A. Léger, F. Selsis, C. Sotin, T. Guillot, D. Despois, D. Mawet, M. Ollivier, A. Labèque, C. Valette, F. Brachet, B. Chazelas, and H. Lammer. A new family of planets? "Ocean-Planets". *Icarus*, 169:499–504, June 2004.

D. N. C. Lin, P. Bodenheimer, and D. C. Richardson. Orbital migration of the planetary companion of 51 Pegasi to its present location. *Nature*, 380:606–607, April 1996.

C. H. Lineweaver and D. Grether. What Fraction of Sun-like Stars Have Planets? *ApJ*, 598:1350–1360, December 2003.

W. M. Liu, P. M. Hinz, M. R. Meyer, E. E. Mamajek, W. F. Hoffmann, and J. L. Hora. A Resolved Circumstellar Disk around the Herbig Ae Star HD 100546 in the Thermal Infrared. *ApJ*, 598:L111–L114, December 2003.

W. M. Liu, P. M. Hinz, W. F. Hoffmann, G. Brusa, F. Wildi, D. Miller, M. Lloyd-Hart, M. A. Kenworthy, P. C. McGuire, and J. R. P. Angel. Adaptive Optics Nulling Interferometric Constraints on the Mid-Infrared Exozodiacal Dust Emission around Vega. *ApJ*, 610:L125–L128, August 2004.

W. M. Liu, P. M. Hinz, W. F. Hoffmann, G. Brusa, D. Miller, and M. A. Kenworthy. Resolved Mid-Infrared Emission around AB Aurigae and V892 Tauri with Adaptive Optics Nulling Interferometric Observations. *ApJ*, 618:L133–L136, January 2005.

W. M. Liu, P. M. Hinz, M. R. Meyer, E. E. Mamajek, W. F. Hoffmann, G. Brusa, D. Miller, and M. A. Kenworthy. Observations of Herbig Ae Disks with Nulling Interferometry. *ApJ*, 658:1164–1172, April 2007.

J. E. Lovelock. Thermodynamics and the Recognition of Alien Biospheres. *Royal Society of London Proceedings Series B*, 189:167–180, May 1975.

C. Lovis, M. Mayor, F. Pepe, Y. Alibert, W. Benz, F. Bouchy, A. C. M. Correia, J. Laskar, C. Mordasini, D. Queloz, N. C. Santos, S. Udry, J.-L. Bertaux, and J.-P. Sivan. An extrasolar planetary system with three Neptune-mass planets. *Nature*, 441:305–309, May 2006.

V. Mannings and M. J. Barlow. Candidate Main-Sequence Stars with Debris Disks: A New Sample of Vega-like Sources. *ApJ*, 497:330–+, April 1998.

V. Mannings, A. Boss, and S. Russell. Protostars and Planets IV. *Icarus*, 143:1–+, January 2000.

G. Marcy, R. P. Butler, D. Fischer, S. Vogt, J. T. Wright, C. G. Tinney, and H. R. A. Jones. Observed Properties of Exoplanets: Masses, Orbits, and Metallicities. *Progress of Theoretical Physics Supplement*, 158:24–42, 2005.

T. Matsuo, H. Shibai, T. Ootsubo, and M. Tamura. Planetary Formation Scenarios Revistied: Core-Accretion Versus Disk Instability. *ArXiv Astrophysics e-prints*, March 2007.

D. Mawet. *Subwavelength gratings for extrasolar planetary system imaging and characterization.* PhD thesis, Liège University, Liège, Belgium, 2006.

M. Mayor and D. Queloz. A Jupiter-Mass Companion to a Solar-Type Star. *Nature*, 378:355–+, November 1995.

B. Mennesson and J. M. Mariotti. Array Configurations for a Space Infrared Nulling Interferometer Dedicated to the Search for Earthlike Extrasolar Planets. *Icarus*, 128:202–212, July 1997.

B. Mennesson, A. Léger, and M. Ollivier. Direct detection and characterization of extrasolar planets: The Mariotti space interferometer. *Icarus*, 178:570–588, November 2005.

A. A. Michelson and F. G. Pease. Measurement of the diameter of alpha Orionis with the interferometer. *ApJ*, 53:249–259, May 1921.

T. Owen. The Search for Early Forms of Life in Other Planetary Systems - Future Possibilities Afforded by Spectroscopic Techniques. In M. D. Papagiannis, editor, *Strategies for the Search for Life in the Universe*, volume 83 of *Astrophysics and Space Science Library*, pages 177–+, 1980.

M. A. C. Perryman. Extra-solar planets. *Reports of Progress in Physics*, 63:1209–1272, 2000.

J. B. Pollack, O. Hubickyj, P. Bodenheimer, J. J. Lissauer, M. Podolak, and Y. Greenzweig. Formation of the Giant Planets by Concurrent Accretion of Solids and Gas. *Icarus*, 124:62–85, November 1996.

J. B. Pollack. Origin and History of the Outer Planets: Theoretical Models and Observations L Contraints. *ARA&A*, 22:389–424, 1984.

S. N. Raymond, A. M. Mandell, and S. Sigurdsson. Exotic Earths: Forming Habitable Worlds with Giant Planet Migration. *Science*, 313:1413–1416, September 2006.

S. Reffert, D. Ségransan, R. Launhardt, T. Henning, D. Queloz, A. Quirrenbach, F. Pepe, J. Setiawan, and P. Weise. The PRIMA astrometric planet search: goals and prospects. In *Advances in Stellar Interferometry. Edited by Monnier, John D.; Schöller, Markus; Danchi, William C.. Proceedings of the SPIE, Volume 6268, pp. 626846 (2006).*, volume 6268 of *Presented at the Society of Photo-Optical Instrumentation Engineers (SPIE) Conference*, July 2006.

G. H. Rieke, K. Y. L. Su, J. A. Stansberry, D. Trilling, G. Bryden, J. Muzerolle, B. White, N. Gorlova, E. T. Young, C. A. Beichman, K. R. Stapelfeldt, and D. C. Hines. Decay of Planetary Debris Disks. *ApJ*, 620:1010–1026, February 2005.

D. D. Sasselov and M. Lecar. On the Snow Line in Dusty Protoplanetary Disks. *ApJ*, 528:995–998, January 2000.

J. Schneider, P. Riaud, G. Tinetti, H. M. Schmid, D. Stam, S. Udry, P. Baudoz, A. Boccaletti, O. Grasset, D. Mawet, J. Surdej, and The See-Coast Team. SEE-COAST: The Super-Earth Explorer. In D. Barret, F. Casoli, G. Lagache, A. Lecavelier, and L. Pagani, editors, *SF2A-2006: Semaine de l'Astrophysique Francaise*, pages 429–+, June 2006.

J. Schneider. The extrasolar planet encyclopedia, http://exoplanet.eu/catalog.php, 2007.

S. Seager and D. D. Sasselov. Theoretical Transmission Spectra during Extrasolar Giant Planet Transits. *ApJ*, 537:916–921, July 2000.

A. Segura, K. Krelove, J. F. Kasting, D. Sommerlatt, V. Meadows, D. Crisp, M. Cohen, and E. Mlawer. Ozone Concentrations and Ultraviolet Fluxes on Earth-Like Planets Around Other Stars. *Astrobiology*, 3:689–708, December 2003.

F. Selsis, D. Despois, and J.-P. Parisot. Signature of life on exoplanets: Can Darwin produce false positive detections? *A&A*, 388:985–1003, June 2002.

F. Selsis, B. Chazelas, P. Borde, M. Ollivier, F. Brachet, M. Decaudin, F. Bouchy, D. Ehrenreich, J. . Griessmeier, H. Lammer, C. Sotin, O. Grasset, C. Moutou, P. Barge, M. Deleuil, D. Mawet, D. Despois, J. F. Kasting, and A. Leger. Could we identify hot Ocean-Planets with CoRoT, Kepler and Doppler velocimetry? *ArXiv Astrophysics e-prints*, January 2007.

E. Serabyn, A. Booth, M. M. Colavita, S. Crawford, J. Garcia, J. Gathright, M. Hrynevych, C. Koresko, R. Ligon, B. Mennesson, T. Panteleeva, S. Ragland, K. Summers, W. Traub, K. Tsubota, E. Wetherell, P. Wizinowich, and J. Woillez. Science observations with the Keck Interferometer Nuller. In *Advances in Stellar Interferometry. Edited by Monnier, John D.; Schöller, Markus; Danchi, William C.. Proceedings of the SPIE, Volume 6268, pp. 626815 (2006).*, volume 6268, July 2006.

E. Serabyn. Nanometer-Level Path-Length Control Scheme for Nulling Interferometry. *Appl. Opt.*, 38:4213–4216, July 1999.

M. Shao. Search for terrestrial planets with SIM Planet Quest. In *Advances in Stellar Interferometry. Edited by Monnier, John D.; Schöller, Markus; Danchi, William C.. Proceedings of the SPIE, Volume 6268, pp. 62681Z (2006).*, volume 6268 of *Presented at the Society of Photo-Optical Instrumentation Engineers (SPIE) Conference*, July 2006.

N. Siegler, J. Muzerolle, E. T. Young, G. H. Rieke, E. E. Mamajek, D. E. Trilling, N. Gorlova, and K. Y. L. Su. Spitzer 24 μm Observations of Open Cluster IC 2391 and Debris Disk Evolution of FGK Stars. *ApJ*, 654:580–594, January 2007.

A. Sozzetti, S. Casertano, M. G. Lattanzi, and A. Spagna. The GAIA astrometric survey of the solar neighborhood and its contribution to the target database for DARWIN/TPF. In M. Fridlund, T. Henning, and H. Lacoste, editors, *Earths: DARWIN/TPF and the Search for Extrasolar Terrestrial Planets*, volume 539 of *ESA Special Publication*, pages 605–610, October 2003.

A. Stankov. All sky target stars catalogue - no limit in ecliptic latitude, 2005.

V.J. Sterken, A. Kamp, S. Kampen, and T.C. van den Dool. Impact of the space environment on Darwin and a low earth orbit (LEO) demonstration mission. In *Proceedings of the IAC (2005).*, IAC-05- C.2.5, 2005.

V.J. Sterken. Impact of the space and satellite environment on the optical path differences of Darwin. Master's thesis, Delft University of Technology, 2005.

D. Sudarsky, A. Burrows, and I. Hubeny. Theoretical Spectra and Atmospheres of Extrasolar Giant Planets. *ApJ*, 588:1121–1148, May 2003.

T. Takeuchi and P. Artymowicz. Dust Migration and Morphology in Optically Thin Circumstellar Gas Disks. *ApJ*, 557:990–1006, August 2001.

G. Tinetti, A. Vidal-Madjar, M.-C. Liang, J.-P. Beaulieu, Y. Yung, S. Carey, R. J. Barber, J. Tennyson, I. Ribas, N. Allard, G. E. Ballester, D. K. Sing, and F. Selsis. Water vapour in the atmosphere of a transiting extrasolar planet. *Nature*, 448:169–171, July 2007.

W. A. Traub, M. Levine, S. Shaklan, J. Kasting, J. R. Angel, M. E. Brown, R. A. Brown, C. Burrows, M. Clampin, A. Dressler, H. C. Ferguson, H. B. Hammel, S. R. Heap, S. D. Horner, G. D. Illingworth, N. J. Kasdin, M. J. Kuchner, D. Lin, M. S. Marley, V. Meadows, C. Noecker, B. R. Oppenheimer, S. Seager, M. Shao, K. R. Stapelfeldt, and J. T. Trauger. TPF-C: status and recent progress. In *Advances in Stellar Interferometry. Edited by Monnier, John D.; Schöller, Markus; Danchi, William C.. Proceedings of the SPIE, Volume 6268, pp. 62680T (2006).*, volume 6268 of *Presented at the Society of Photo-Optical Instrumentation Engineers (SPIE) Conference*, July 2006.

S. Udry, X. Bonfils, X. Delfosse, T. Forveille, M. Mayor, C. Perrier, F. Bouchy, C. Lovis, F. Pepe, D. Queloz, and J.-L. Bertaux. The HARPS search for southern extra-solar planets. XI. Super-Earths (5 and 8 M{$\oplus$}) in a 3-planet system. *A&A*, 469:L43–L47, July 2007.

A. Vidal-Madjar, A. Lecavelier des Etangs, J.-M. Désert, G. E. Ballester, R. Ferlet, G. Hébrard, and M. Mayor. An extended upper atmosphere around the extrasolar planet HD209458b. *Nature*, 422:143–146, March 2003.

A. Villien, J. Morand, M. Delpech, and P.Y. Guidotti. GNC for the Pegase Mission. 17th IFAC Symposium on Automatic Control in Aerospace, 2007.

W. R. Ward. On Type III Protoplanet Migration. *AGU Fall Meeting Abstracts*, pages A6+, December 2004.

A. Wolszczan and D. A. Frail. A planetary system around the millisecond pulsar PSR1257 + 12. *Nature*, 355:145–147, January 1992.

M. C. Wyatt and W. R. F. Dent. Collisional processes in extrasolar planetesimal discs - dust clumps in Fomalhaut's debris disc. *MNRAS*, 334:589–607, August 2002.

M. C. Wyatt, R. Smith, J. S. Greaves, C. A. Beichman, G. Bryden, and C. M. Lisse. Transience of Hot Dust around Sun-like Stars. *ApJ*, 658:569–583, March 2007.